Anno Accademico 2007-2008

UNIVERSITÀ DEGLI STUDI DI TRIESTE

FACOLTÀ DI SCIENZE MATEMATICHE, FISICHE E NATURALI

CORSO DI LAUREA SPECIALISTICA IN FISICA

Curriculum: Fisica della Materia

Time dependent dielectric function of photo-excited CuGeO$_3$

Relatore:
Ch.mo Prof. Fulvio Parmigiani

Correlatore:
Dott. Goran Zgrablic

Laureando:
Alberto Crepaldi

Anno Accademico 2007-2008

UNIVERSITÀ DEGLI STUDI DI TRIESTE

FACOLTÀ DI SCIENZE MATEMATICHE, FISICHE E NATURALI

CORSO DI LAUREA SPECIALISTICA IN FISICA

Curriculum: Fisica della Materia

Dipendenza temporale della funzione dielettrica del $CuGeO_3$ fotoeccitato

Relatore:
Ch.mo Prof. Fulvio Parmigiani

Laureando:
Alberto Crepaldi

Correlatore:
Dott. Goran Zgrablic

Abstract

$CuGeO_3$ is a charge tranfer insulator with an energy gap close to the photon energy of the second harmonic of the Ti:Sa laser emission. For this reason $CuGeO_3$ is an ideal candidate to study the dynamic of photo-excited CT processes in strongly electron-correlated compounds.

This thesis deals with an optical pump-probe experiment on $CuGeO_3$ single crystals photo-excited across the charge transfer energy gap (Δ_{pd} ~3.5 eV). From the variation of the optical density, measured in the spectral range 400-720 nm, the time-dependent dielectric function has been obtained.

In this experiment the probe is an ultra-short super-continuum coherent laser pulse, while the pump is either the fundamental emission of the Ti:Sa (~ 800 nm) or its second harmonic (~ 400 nm).

The experimental set-up allows measuring the shot-to-shot change of the optical density (ΔOD) at controlled pump-probe delay times.

The change in the optical properties displays two main spectral features, at ~ 2.2 eV (~ 420 nm) and at ~ 2.9 eV (~ 530 nm). The origin of these features is interpreted in the frame of the Lorentz model, from which the time-dependent dielectric function is obtained, while the evolution of the dielectric function on the sub-ps time-scale indicates that the impulsive injection of holes into the O-2*p* orbitals perturb, both, the local crystal field, experimented by Cu ions, and the O-2*p* – O-2*p* overlap integral. Instead, the time evolution of the dielectric function in the picosecond time-scale is interpreted as the fingerprint of the structural changes of the $CuGeO_3$ lattice.

Finally, these results help to elucidate the dynamic of the electronic structure of this strongly electron-correlated material under a photonic perturbation.

2. Theoretical background

3. Photo-induced phase transitions

4. Properties of $CuGeO_3$

5. Experimental set-up

6. Experimental results

7. Data analysis

8. Discussions

1. Introduction

The possibility of controlling the structural properties of solids represents one of the most interesting problems in physics, challenging our capability of describing elementary excitations and many-body interactions in functional and structural materials.

As well known, the correlation between charge and neutral particles controls the behaviour of the condensed matter giving rise to new and exotic properties such as the super-conductivity [1], the spin and charge density wave [2], the magnetic ordering and the spin-Peierls transitions [3].

In the literature there is an impressive amount of works where the elementary excitations in solids are controlled by doping the system with atomic species, with impurities and/or by replacing the ions with elements having different ionic radii [4] or by the substitution of the ions with other having a different valence, in order to change the density of charge carriers [5]. However, besides these composition changes, other physical effects can be used to modify the material properties [6-9]. In general, a change in the material structure is expected when the charge density is modified.

In the recent years laser systems, capable to produce pulses in the femto-second time scale, became a powerful tool to transiently modify the charge carrier density, by optical excitations. In addition, the sub-picosecond time resolution gives the possibility to probe the system while it is recovering from the excitation process.

For example, time–resolved spectroscopy and the pump-probe techniques opened the gate to study the photo-induced insulator-to-metal transitions in doped manganites [10] and VO_2 [11], phase transition in organic crystals [12] and photo-induced non-thermal electronic phase transition in high temperature superconductor (HTSC) [40].

In the frame of transient effects induced by intense ultra-fast laser pulses, one of the most important results has been obtained on GaAs by Callan, Mazur *et al.* [13]. In this case the band gap collapse and the rising of a metallic behaviour have been reported and investigated [14,15].

In time-resolved optical experiments two models are considered to account for the variation of optical properties (reflectivity and transmittivity) [16, 17]. For example, the susceptibility of metals, and semiconductors, perturbed by low fluence ultra-short laser pulses are described by the Drude formalism, whereas semiconductors under strong fluence laser light are described by the Lorentz formalism.

In these last few years a great deal of efforts has been made to understand the out-of-equilibrium behaviour of systems with more complex electronic structure rather than semiconductors or simple metals; experiments have been performed to investigate strongly correlated systems, such as Mott-Hubbard and charge transfer insulators [18].

This thesis is aimed to investigate the dynamical photo-induced properties of a $CuGeO_3$ single crystal, through a pump-probe experiment.

$CuGeO_3$ is a charge transfer insulator belonging to the well known family of the cuprates. It has an absorption spectra characterized by a charge transfer absorption edge at ~3.5 eV, and a significant structure in the absorption spectrum, between ~1.4 eV and ~2.1 eV, ascribed to phonon mediated d-d transitions [19].

$CuGeO_3$ is blue in colour and transparent, therefore allowing trasmittivity measurements up to the charge transfer gap energy ~3.5 eV.

The experimental novelty of this work is represented by the use of a super-continuum ultra-short pulse, generated by a non-linear optical process in a CaF_2 [20], properly retarded with respect to the pump.

The time dependent variation of the optical density through the 400 - 720 nm spectral range allows to evaluate the time-dependent dielectric function of $CuGeO_3$ photo-excited at 400 nm and 800 nm. In this later case it is not possible to induce a charge transfer through a linear process, but the electrons are re-arranged within the d-bands of Cu, though the phonon assisted d-d intra-band transitions.

The time dependent variation of the optical density is fitted by three exponential-decay constants, while a differential dielectric function model has been used to fit the spectra. The best fit has been obtained by employing, for all the time delays, two simple Lorentz oscillators at ~ 2.2 eV and ~ 2.9 eV.

The time evolution, on the sub-ps time-scale, of the dielectric function, along with the parameters of the oscillators, suggest that the impulsive injection of holes into the O-2*p* oxygen orbitals suddenly delocalize perturbing both the local crystal field experimented by Cu ions and the O-2*p* overlap integral.

In addition, the time evolution of the dielectric function in the picosecond time scale is interpreted as the fingerprint of the structural changes of the $CuGeO_3$ lattice.

In section 2 a brief introduction to many-body effects in strongly correlated materials is reported. In section 3 the conventional phase transitions and transient laser-induced effects are discussed.

Section 4 reports the main properties of $CuGeO_3$.

In section 5 the experimental set-up, along with the laser system, the pump-probe arrangement, the super-continuum generation and the data acquisition through two synchronized arrays of photodiode, are described.

Then the transmittivity data are presented in section 6, while section 7 reports the data analysis and the procedure, to obtain the time-dependent dielectric functions.

The interpretation and discussion of the data are given in section 8. The conclusions remarks are reported in section 9.

2. Theoretical background

2.1 Strongly correlated materials

The first successful theoretical description of simple metals was based on non-interacting or weakly-interacting electron models. In these models the formation of the band structure is due completely to the periodicity of the crystal lattice being the free electrons described as a travelling plane waves [16].

The distinction between metals and insulators is based on the filling of the bands (at zero temperature). For insulators the highest filled band is completely filled, instead for metals it is partially filled.

Following this simple model a system with an odd number of electrons per unitary cell, is a metal. However this picture fails to describe systems with a more complex electron structure. In 1937 de Boer and Verwey reported that many transition-metals oxide, such as NiO, with partially filled *d*-electron band were poor conductors, or insulators with a large band gap [21]. It was soon evident that the origin of this insulating behaviour is due to many-body interactions which the simple band model neglects.

The first experiments on the transition-metal compounds were the beginning of a still-open challenging problem.

In fact, in condensed matter there is an impressive amount of physical phenomena, such as superconductivity, spin/charge density wave, colossal magneto-resistance, metal-to-insulator transition (MTI), that require a the many-body approach.

In the following the Mott approach and the Hubbard formalism for the description of the MTI are briefly introduced.

2.2 The Mott model

In MTI systems it is possible to find a physical variable (like the charge carrier density, or the repulsive coulomb potential between charge carriers) that acts as an order parameter.

The first theoretical approach capable to overtake the one-electron band structure picture is due to N.Mott [22].

The simpler description of this model is based on a periodic lattice of hydrogen atoms where, at the beginning, the many-body interactions are neglected. In this case the resulting band structure consists in a half-filled band, originating from the *s*-like singly occupied orbitals.

The interactions could then be adiabatically “switched on”, such that the electrons will feel the repulsive coulomb interaction. As a consequence the half-filled band is split in two sub-bands. The lower in energy is occupied by the electrons from initially single occupied lattice sites. Instead the upper sub-band accommodates the electrons belonging to a doubly occupied lattice site.

Therefore a chain of hydrogen atoms, with an electron per unit cell, is not anymore a metal, being the lower sub-bands filled, and the upper sub-band empty.

2.3 The Mott-Hubbard insulator

In a one-dimensional chain of hydrogen atoms the band formation could be described through a three terms tight-binding model [23]. The first one, linked to the electron kinetic energy, describes the electrons capability to "jump" from an atom to the nearest neighbour. This "hopping term" is at the origin of the charge transport and thermal conductivity properties. The second term, that represents the analytical formalization of the Mott argument, is a repulsive coulomb potential between two electrons occupying the same lattice site. This last term is a characteristic of the second quantization formalism, in which the number of particles of the system is not determined but is given by a statistical description of the quantum-mechanic counterpart of the grand-canonical ensemble.

The resulting Hamiltonian is

$$H_H = H_t + H_U - \mu N \qquad ; \qquad 2.1\,(\,a\,)$$

being

$$H_t = -t \sum_{<i,j>} \left(c_{i\sigma}^{+} c_{j\sigma} + H.c \right) \qquad ; \qquad 2.1\,(\,b\,)$$

$$H_U = U \sum_{i} \left(n_{i\uparrow} - \frac{1}{2} \right) \left(n_{i\downarrow} - \frac{1}{2} \right) \qquad ; \qquad 2.1\,(\,c\,)$$

$$N = \sum_{i\sigma} n_{i\sigma} \qquad . \qquad 2.1\,(\,d\,)$$

The kinetic energy in the hopping process is represented by t, while c and c^{+} are the annihilation and creation operators, $n_{i\sigma}$ is the number operator for the electrons with spin σ in the "lattice i-nth site" [23] .

The variation of the coulomb repulsive potential (U), permits the system to change the transport properties. For $U = 0$ the electrons are non-interactive, and a single occupancy leads to a metallic state. If $U >> t$, the doubly occupancy is energetically un-favourable, therefore inducing a band splitting and, as a consequence, to an insulating state.

This class of insulators is generally known as Mott-Hubbard insulators.

2.4 The charge transfer insulator

In the Hubbard formalism there are some simplifications, such as for example, the use of *s*-electrons only. In fact, most of the MTI are *d*-electrons compounds [24].

For *d*-electrons systems, the orbital degeneracy is a source of complex behaviour, and the Hubbard formalism has to be slightly modified to take into account the possibility of degenerate bands near the Fermi energy along with the mechanism of orbital fluctuations and orbital symmetry breaking effects.

Before analysing the application of the Hubbard model to *d*-electron systems it is important, for example, to consider also the overlap between the *d*-metal bands and the *p*-ligand bands.

For oxide-based compounds the oxygen *2p* level becomes close to the partially filled *3d* band. Hence, the charge gap of the Mott insulator cannot be accounted only by *d*-electrons. In fact, when the simple *d*-band is used in the Hubbard model, the charge gap is formed between a singly occupied band (lower Hubbard sub-band) and a doubly occupied band (with spin-up and spin-down). Nonetheless, if the *2p* level becomes closer, the character of the minimum excitation gap can change from a gap between singly occupied *d*-bands to a fully occupied *p*-band (see Fig. 2.1).

This kind of insulators were described by Zaanen, Sawatzky and Allen in 1985 [25] as a charge-tranfer insulator (CTI).

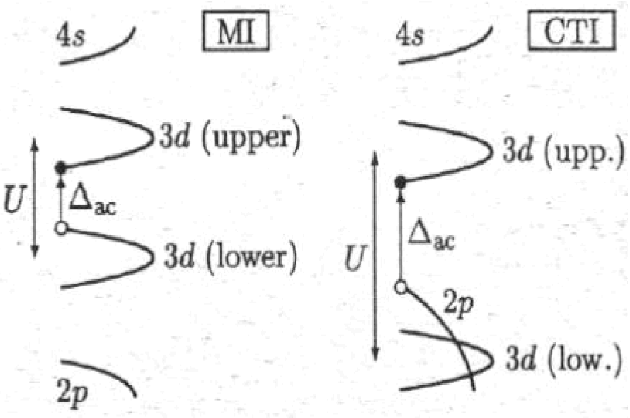

Fig. 2.1- *Schematic description of the density of states for the MI and CTI insulators. The MI insulator has the smallest energy gap between the two Hubbard sub-bands In the CTI the excitation involves a 2-p oxygen electron and the upper sub-band [24].*

2.5 The Hubbard model for d-electrons systems

The Hubbard model described in the previous paragraph neglects multi-band effects, so it is applicable to *d*-electron systems only under restricted hypothesis. The degeneracy has to be lifted by an anisotropic crystal field, in order to describe the low energy excitation by a single band near the Fermi energy.

In this case it is assumed that the *p*-ligand band is far in energy from the *d*-bands, or it is strongly hybridized to form a single band in order to neglect the inter-site coulomb force. Under these simplifications the Hubbard model can reproduce only qualitatively the Mott insulating phase.

To describe the charge ordering effect, the near neighbour interactions should be considered. Therefore the hamiltonian should be written as [24]

$$H = H_H + H_V \quad ; \tag{2.2 (a)}$$

where

$$H_V = V \sum_{<i,j>} n_i n_j \quad ; \tag{2.2 (b)}$$

$$n_i = \sum_{\sigma} n_{i\sigma} \quad . \tag{2.2 (c)}$$

The H_V term describes the nearest neighbour coulomb interaction between charge carrierss occupying the i-th lattice site (with the two possible spin). While H_H is the Hubbard hamiltonian already reported.

When the Fermi energy is across the bands with an E_g symmetry the degeneracy is twofold (in the absence of a Jahn-Teller distortion). Otherwise, for weak Jahn-Teller distortion it is necessary to consider three orbitals (d_{xy}, d_{xz}, d_{yz}) for the bands with a T_{2g} symmetry, and two orbitals ($d_{x^2-y^2}$, $d_{3z^2-r^2}$) for the band with a E_g symmetry. This leads to the degenerate Hubbard model;

$$H_{DH} = H_{Dt} + H_{DU} + H_{DV} + H_{DUJ} \quad ; \tag{2.3 (a)}$$

being

$$H_{Dt} = -\sum_{<i,j>;\sigma,\nu,\nu'} k \left(t_{ij}^{\nu,\nu'} \, c^{*}_{i\sigma\nu} \, c_{j\sigma\nu'} + H.c. \right) \quad ; \tag{2.3 (b)}$$

$$H_{DU} = \sum_{i;\sigma,\sigma',\nu,\nu'} \left(1 - \delta_{\nu\nu'} \, \delta_{\sigma\sigma'} \right) U_{\nu\nu'} \, n_{i\sigma\nu} \, n_{i\sigma'\nu'} \quad ; \tag{2.3 (c)}$$

$$H_{DUJ} = -\sum_{i;\sigma,\sigma',\upsilon,\upsilon'} J_{0\upsilon\upsilon'} \left[\left(1-\delta_{\upsilon\upsilon'}\right) c^{*}_{i\upsilon\sigma} c_{i\upsilon\sigma'}\, c^{*}_{i\upsilon'\sigma'} c_{i\upsilon'\sigma} - \left(1-\delta_{\upsilon\upsilon'}\right)\left(1-\delta_{\sigma\sigma'}\right) c^{*}_{i\upsilon'\sigma'} c^{*}_{i\upsilon'\sigma}\, c_{i\upsilon\sigma} c_{i\upsilon\sigma'} \right] \qquad 2.3\,(\,d\,)$$

Where υ and υ' describe the orbital degree of freedom, and H_{DUJ} is the contribution of the intra-site exchange interaction, with

$$J_{O\upsilon\upsilon'} = \int d\vec{r} d\vec{r}\,'\ \psi_i^{\upsilon}(\vec{r})\,\psi_i^{\upsilon'}(\vec{r})\,\frac{e^2}{|\vec{r}-\vec{r}\,'|}\ \psi_i^{\upsilon}(\vec{r}\,')\,\psi_i^{\upsilon'}(\vec{r}\,')\ . \qquad 2.3\,(\,e\,)$$

Assuming ψ to be real. The inter-site exchange term is neglected.

The term H_{DUJ} generates a strong Hund's rule coupling, since electrons with opposite spin on different atomic orbitals feel a strong repulsive potential.

In this orbital-degenerate model, besides the spin correlation, there are also orbital correlations, which can lead to orbital long-range order. The term H_{DU} represents the intra-orbital coulomb energy $U_{\upsilon,\upsilon}$ as well as the inter-orbital coulomb energy $U_{\upsilon,\upsilon'}$ for the on-site repulsion (typical of the Mott argument), instead the inter-site repulsion is given by H_{DV}.

The orbital exchange coupling is different from the spin exchange since, the first can be highly anisotropic.

Also the transfer term can show anisotropy, being the charge transfer from the $d_{x^2-y^2}$ orbital, in general, larger in the x and y directions, respect to the z direction. Instead, the opposite is observed for the $d_{3z^2-r^2}$ orbital.

These anisotropies introduce complex features in the band structure.

2.6 Hybridized *d* and *p* bands and the d-p model

Transition-metal-oxides based compounds, show strong hybridization effect between *d* and *p* orbitals. This mechanism pushes the oxygen *2-p* orbital nearer to the Fermi energy. For these systems the hamiltonian could be described by considering the d-p hybridized term [24,25]

$$H_{dp} = H_{dpt} + H_{dpU} + H_{dpV} \qquad ; \quad 2.4\,(\,a\,)$$

where

$$H_{dpt} = -\sum_{<i,j>;\sigma} t_{pd} \left(d^{*}_{i\sigma}\, p_{j\sigma} + H.c \right) + \varepsilon_d \sum_i n_{di} + \varepsilon_p \sum_j n_{pj} \;; \quad 2.4\,(\,b\,)$$

$$H_{dpU} = U_{dd} \sum_i n_{di\uparrow} n_{di\downarrow} + U_{pp} \sum_i n_{pi\uparrow} n_{pi\downarrow} \qquad ; \quad 2.4\,(\,c\,)$$

$$H_{dpV} = V_{dp} \sum_{<i,j>} n_{pi} n_{dj} \qquad . \quad 2.4\,(\,d\,)$$

When the *p* orbital energy, ε_p, is lower than ε_d, the oxygen orbitals contribute to the transport properties only through virtual processes described by a second order perturbation theory.

Systems where $(\varepsilon_d - \varepsilon_p)$ is larger than U_{dd} are known as Mott-Hubbard insulators.

Vice versa when $(\varepsilon_d - \varepsilon_p)$ is smaller than U_{dd}, the insulating phase is mainly due to charge tranfer effects, and further added holes occupy an oxygen *p*-band.

The insulator characterization is, in general, given by the lowest excitation able to create a charge carrier. For example, in $CuGeO_3$ the most relevant excitation process tranfers an electron from the *2p* ligand band into the *3d* upper Hubbard sub-band [26]. The excitation process creates a quasi-particle, with a *d*-like symmetry and a *p*-like hole, which is the basic charge carrier mechanism of the system.

There is another picture that can be adopted to recognize the CTI or the Mott-Hubbard character of the insulating phase [19]. This consists in comparing the on-site Coulomb repulsive potential U_{dd} with Δ_{pd}, expressed by

$$\Delta_{pd} = E_0\left(d^{n+1}L \right) - E_0\left(d^n \right) \qquad . \quad 2.5$$

Where "*L*" is the hole in the ligand band. In the $CuGeO_3$ the energy of the d^{n} , d^{n+1} process is lower than U_{dd} (equal to ≈ 8-9 eV) [19] . As it is possible to see in fig 2.1 the activation energy is not simply Δ_{pd}, since the intrinsic width of the quasi-particle and the hole levels (W_d, W_p) must be considered.

In this case the CT energy, Δ_{ac}, is given by

$$\Delta_{ac} = \Delta_{pd} - \frac{W_d + W_p}{2} \quad . \qquad 2.6$$

3. Photo-induced phase transitions

3.1 Phase transitions controlled by bandwidth and band filling

The first controlled phase transition in strongly correlated materials was achieved through the control of *W*, by modifying the chemical composition [4]. This phase transition is known as bandwidth control (BC-MIT), fundamentally different from the phase transition obtained by changing the charge density, *n* (filling control FC-MIT). Many examples of the BC-MIT are reported in the literature, for example in the $NiS_{2-x}Se_x$ crystal [4] which undergoes a charge transfer insulator to metal transition at room temperature by varying x from 0 to 0.6 .

In perovskite compounds, with a general stoichiometric formula ABO_3, the *W* control is made by changing A, i.e. changing the radius of the ions will induce a lattice distortion, which can be quantify by the so-called tolerance factor f [24]

$$f = \frac{(r_A + r_O)}{\sqrt{2}(r_B + r_O)} \quad . \qquad 3.1$$

This distortion will reflect on the bond angle B-O-B, which varies continuously with *f*, modifying the overlap between the bonding orbitals of the ions, therefore inducing a variation of *W* [27].

On this matter a lot of experiments were performed, especially in perovskite compounds, since these systems have the advantages that by changing the “A” *n* remains constant, and controlled phase transitions (BC and FC) can be achieved [28].

The possibility of inducing a metal to insulator phase transition by varying *n* has been widely recognized and studied since the discovery of HTSC’s [1]. The conventional method of filling control is to utilize ternary or multinary compounds in which the ionic sites can be occupied by different valence ions. For example the substitution of divalent Sr on the trivalent La sites allows the filling control in $La_{2-x}Sr_xCuO_4$ [5].

Filling control is obtained also in non-stoichiometry, or altered stoichiometry, as for example in the case of $YBa_2Cu_3O_{6+\delta}$ [29] where the content of oxygen is variable, and it can introduce holes (changing *n*) in the CuO_4 plaquettes planes. This holes doping procedure, mediated by changing the O concentration, is the key-tool to introduce a superconductive state, while the doping level controls the critical temperature, T_c, of the compound [30].

Filling control using off-stoichiometry has also achieved for non cuprate systems, such as for example $V_{2-x}O_3$ and $LaTiO_{3+\delta}$ [31].

Especially vanadium oxides play an important role since they represent the first MIT-systems in which the insulator-to-metal phase transition (IM-PT) has been induced by an ultra-fast laser light pulse [11].

Both the FC- and BC-MIT are stationary phase transition, not associated to transient phenomena like the laser pulse, or the time controlled switching of a magnetic field. In the following section the attention will be moved from stationary to time dependent phenomena.

3.2 Ultrafast laser induced insulator-to-metal phase transitions

Some Mott insulators exhibit an insulator-to-metal transition (IM-PT) upon heating to temperatures beyond the transition point T_M. Most notably, vanadium oxides, such as V_2O_3 (T_M = 150 K) and VO_2 (T_M = 341 K), show an increase in conductivity by a factor of more than 10^2 across T_M, resulting in a significant change in optical properties [32].

These transitions in vanadium dioxide can be approached by direct heating, radiation, or by heat conversion through optically induced radiation-less relaxation.

In the last years the possibility of using ultra-fast laser sources raised the question if the phase transition is achieved by heating the sample above T_M, or by the direct excitation of charge carriers.

The first studies reported that the PT can be achieved through optical excitation followed by radiation-less relaxation, or phonon dispersion. Gervais attributed the laser-induced PT of VO_2 [33] to the lattice instability at the R point in the Brillouin zone. Srivastava and Chase [34] and McWhan *et al.* [35] considered strong electron-phonon interaction as the origin of the PT. This hypothesis was further tested by Raman and x-ray experiments.

By contrast, measuring the reflectivity versus time delay, Cavalleri *et al.* [11] have recently observed that the time scale of the PT depends on the excitation level, which may occur in a time domain between sub-picoseconds and nanoseconds. Therefore, they concluded that the structural transition might not be thermally initiated. However, a clear mechanism to describe the structural dynamics of the PT was not identified.

It is important to note that the well known effect of insulator-to-metal transition induced by carriers (due to additional electrons or holes liberated from defects, or by thermal excitation or by laser induced carrier injection) could be explained as a result of a decrease of the free energy expansion coefficient for charge transfer harmonic fluctuations. Such a behaviour is related to the increase of carrier induced screening of the charge separation, accompanied by a pronounced softening of the charge tranfer conditions. The latter circumstance could switch-on the charge tranfer mechanism of insulator-to-metal phase transition.

It is interesting now to analyse the charge tranfer mechanism induced by ultra-short laser pulses, in order to better understand the role of the electronic excitations in the phase transition.

3.3 Laser induced charge transfer

Photo-induced phase transitions can be achieved either in strongly correlated electron systems (discussed in the previous paragraphs), by an interplay of charge, spin and orbital degree of freedom [36] or in low dimensional organic solid, by strong electron-phonon coupling [12]. Of special importance is the coherent mechanism to trigger the phase transition, where the energy supplied by the optical excitation is selectively deposited into few coherent phonon modes, providing high speed and high efficiency of the switching process.

Recently a large number of experiments reported phase transitions from an insulating to a metallic state in organic charge transfer salts.

This process has been modelled by studying the excited electronic and vibrational dynamics of isolated charge transfer salt dimers (D), with pronounced CT transition effects($D^+ + D^+ \rightarrow D^{2+} + D^0$) [37].

It is interesting to report the results obtained by Lüer *et al.* [37] in order to understand how the laser induced CT can modify the transmission coefficient by measuring the dynamic variation of the optical transmissivity $\Delta T(\omega)$ respect to the static transmissivity $T(\omega)$, $\Delta T(\omega)/T(\omega)$. This quantity is defined also as differential transmission.

Fig. 3.1 (a) shows the absorption spectrum of the organic salt dimer, where CT is the inter-molecular transition, and D_1 and D_2 are two bands at higher energies, assigned to intra-molecular transitions.

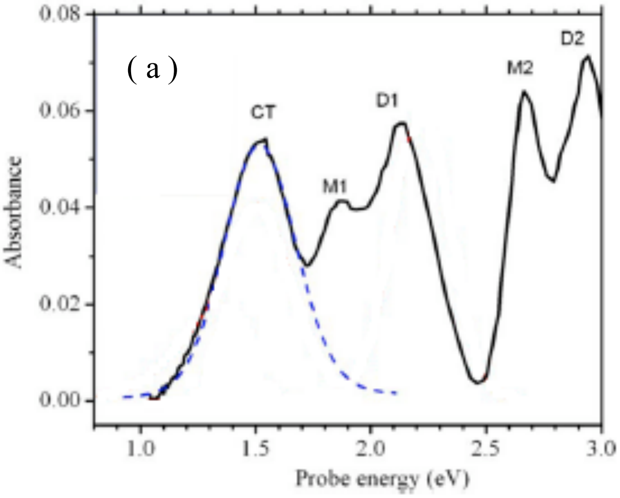

Fig. 3.1 (a)- *Absorption spectrum of* $(TMTTF^+)_2$ *The intra-molecular contributions are labelled with* D_1 *and* D_2.. *CT is the inter-molecular transition.* M_1 *and* M_2 *are the intra-molecular contributions due to the presence of monomers [37].*

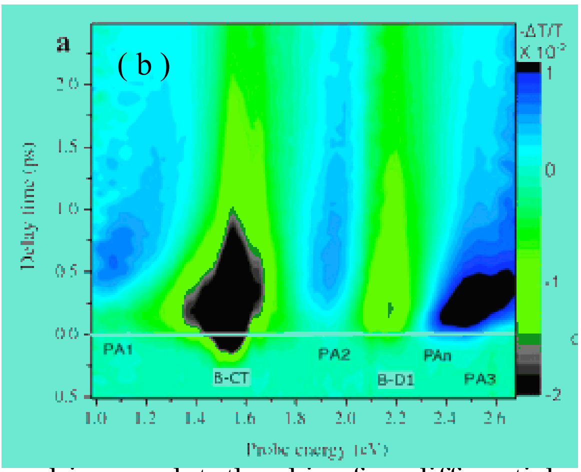

Fig. 3.1 (b)- *Chirp-free two-dimensional time dependent $\Delta T/T$ spectrum. The grey line gives the time zero. B-CT is the transient bleaching of the CT band B-D_1 is associated totheD$_1$ band. PA$_1$, PA$_2$ and PA$_3$ are assigned to hot ground state absorptions from the CT, D_1 and D_2 states [37].*

Fig. 3.1 (b) shows, in a typical bi-dimensional image plot, the chirp free differential transmission ($\Delta T/T$) spectra after the photo-excitation at 1.55 eV. The abscissa reports the energy, while the time delay between pump and probe is reported on the ordinate. It is possible to notice the bleaching of the CT band (B-CT) at 1.5 eV and of D1 (B-D1) at 2.2 eV, which decay within the first picosecond (ps).

For pump-probe delay > 200 fs, three new PA bands grow, red-shifted against the bleaching bands, suggesting a close relationship with the fundamental absorption bands.

The authors interpret the data as shown in Fig. 3.2. The PA1 originates from the same electronic state as B-CT, but with different vibrational population. Thus the delayed bands PA1, PA2, and PA3 can be assigned to hot ground state absorptions to the CT, D1 and D2 states. The scenario is that, after the photo-excitation, there is the quick ground state recovery, with a ~240 fs relaxation time constant (the typical time scale of electronic relaxation), followed by a vibrational cooling of the hot ground state, with a 1.8 ps time constant.

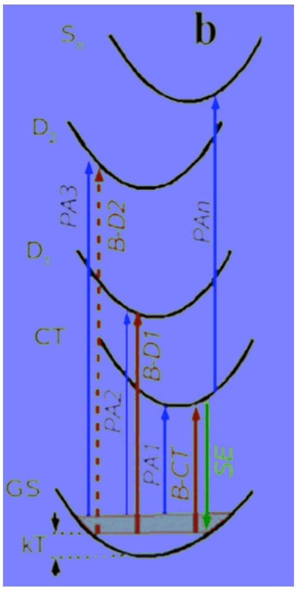

Fig. 3.2- *Schematic assignment of the transient features in fig 3.1 (b) to transitions between the respective dimmer electronic states. In the ground state (GS) potential, room-temperature occupation is indicated by the blue range. The red range indicates the hot ground states [37].*

The laser impulsively excites coherent phonon modes (assigned to the vibration of the dimer out-of-plane) coupled to the CT state. The coherent oscillations damping is partially due to the de-activation back to the ground state, which destroys the coherence and leaves the dimmer in an out-of-equilibrium state, stretched along the intra-molecular configuration. The phonons induced distortion bends the structure of the dimer, and the optical response is found to recall the experimental data obtained in many organic compounds (as (EDO-TTF)$_2$PF$_6$) [38] where this effect is interpreted as a transition from the insulating to the metallic phase.

This model also suggests that vibrations are strongly coupled to the CT transition, leading the electronic transitions to the selective deposition of energy in coherent phonons, whose distortions drastically modify the tranfer integral and the conduction property of the system.

The authors pointed out that since the coupling of the electronic transitions to intra-molecular vibrations is a characteristic common to many CT-compounds, the interpretation of the laser induced phase transition triggered by the changing in the transfer integral is expected to be a general phenomenon in many laser induced phase transitions.

This phenomenology resembles the BC MIT model, in which the change in the transfer integral (and so in the bandwidth), due to lattice distortion, triggers the phase transition.

3.4 Laser induced gap collapse in semiconductor

Recently IM PT haven been classified in two main groups [39]:

a) global phase change via optically excited states;

b) new material phase creation in optically excited states; (even if hybridized situations between them are possible).

Type a) is used to describe the photo-induced structural transitions, mainly observed in some organic materials such as π-conjugated polymers and the organic charge-transfer complexes already described in the previous paragraph [12, 37, 38]. In this case the phase transition is promoted by the laser induced switching between stable and meta-stable structures.

The type b) is typical of inorganic compounds, such as semiconductors (for example GaAs, CuCl, Si) [13]. The phase transition is mainly attributed to electronic transitions and to the "photo-creation and photo-control" of new electronic orders.

The first change in reflectivity data, induced by ultra short laser pulses on semiconductors, were always interpreted as changes in the dielectric constant dominated by the free-carrier contribution to the optical suscettibility. In this assumption the changes in differential reflectivity, $\Delta R/R$, have been always modelled by the Drude formalism. The work of Glezer *et al.* [14] suggests that the Drude model can be used, in order to interpret optical variation in semiconductors, only in low fluence regime.

The authors advance the hypothesis that the laser pulses excite, in higher fluence regime, inter-band transitions, perturbing the equilibrium band structure of the system.

They calculate the inter-band contribution to the suscettibility ($\chi_{inter\text{-}band}$), that arises from the coupling of states in different bands through the electric field of the laser, modelling the dielectric function by a harmonic oscillator, with a resonant frequency corresponding to the average bonding-antibonding splitting energy.

Such a complex dielectric function has a zero crossing of the real component *Re(ε)* coinciding with a peak of the imaginary component *Im(ε)* (as shown in Fig. 3.3).

In this respect the inter-band contribution is very different from the Drude contribution, where the real part is monotonically increasing, while the imaginary part is monotonically decreasing.

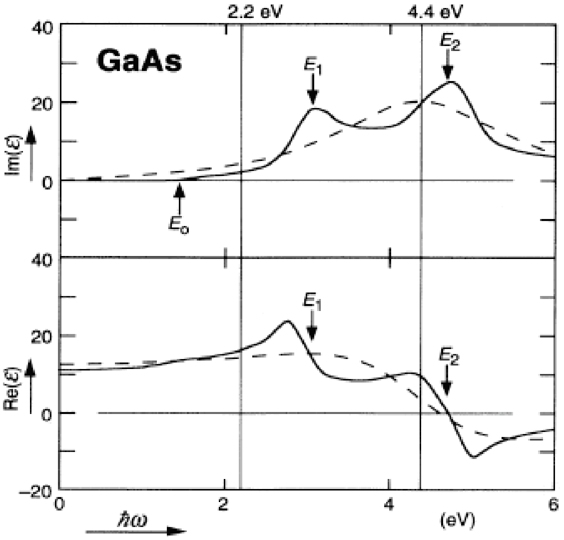

Fig. 3.3- *The solid curves show the dielectric function of GaAs. E_0 labels the fundamental absorption edge, while E_1 and E_2 label the two main absorption peaks. The dashed curves show a fit of the single oscillator dielectric function to the solid curves [14].*

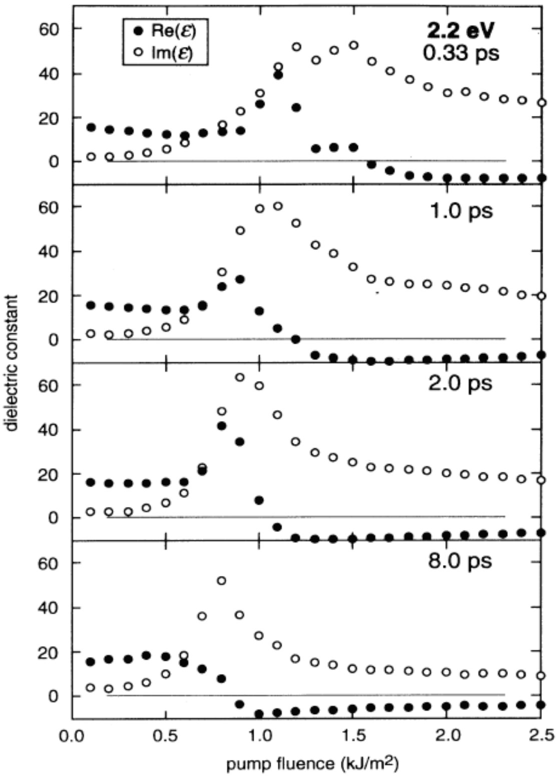

Fig. 3.4- *Dielectric constant (real and imaginary parts) at 2.2 eV vs. pump fluence for four different pump-probe time-delays [14].*

Fig. 3.4 reports the time evolutions of the imaginary (*Im(ε)*) and the real (*Re(ε)*) parts of the dielectric function, obtained by the data acquired with pump energy of 1.9 eV, at different fluences, probed at 2.2 eV. The results are interpreted as an inter-band absorption, since the zero crossing of the real part (*Re(ε)*) is accompanied by the peak in the imaginary (*Im(ε)*) part.

For small time $Re(\varepsilon)$ is positive, so the resonant frequency of the peak starts out higher than the probed frequency. For increasing τ it sweeps down through the probe frequency as $Re(\varepsilon)$ drops to zero, with a rate depending on the pump fluence.

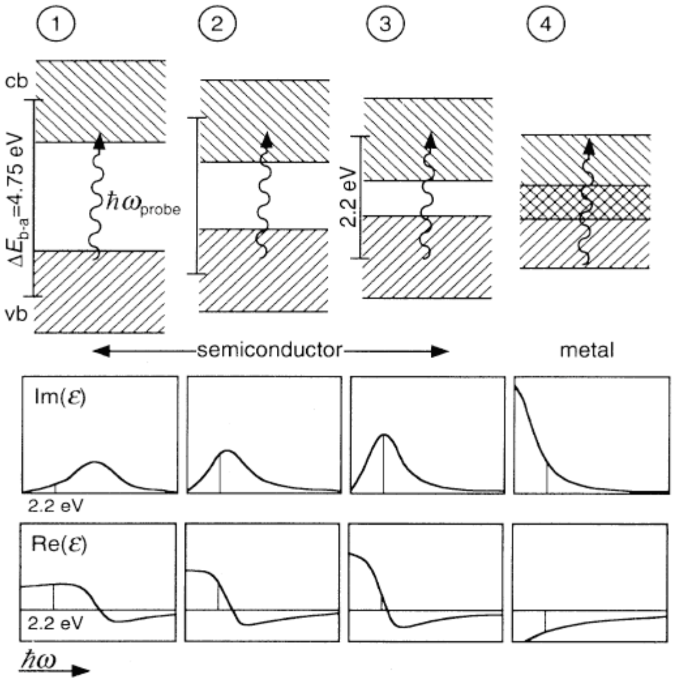

Fig. 3.5- *Schematic representation of the band-gap collapse. The pump pulse leads to a drop in the average bonding–antibonding splitting from its initial value of 2.2 eV. If the minimum in the conduction band drops below the maximum of the valence band the material takes metallic properties. The drop appears as a shift in the main absorption peak in the dielectric function.* ***cb****: conduction band;* ***vb****: valence band****; ΔE*** *average banding-antibonding splitting;* ***ħω*** *is the probe photon energy [14].*

This effect is interpreted as the signature of laser photo-induced band gap collapse, schematically shown in Fig. 3.5.

At the beginning the average bonding-antibonding energy splitting ΔE_{b-a} starts out far above 2.2 eV. As a result of the photo-excitation ΔE_{b-a} starts decreasing, so the resonant frequency of the oscillator gets closer to the frequency of the probe pulse.

As ΔE_{b-a} goes under 2.2 eV the $Im(\varepsilon)$ goes through a maximum. If ΔE_{b-a} drops far enough, the minimum, in the conduction band, will drop under the maximum of the valence band, inducing a non-equilibrium transition from a semi-conductive state to a metallic-like state.

To explain this effect two main mechanisms should be considered. The first arises from the electronic screening, made possible by the generation of electron-hole pairs. The increased population of mobile charged carriers can partially screen the ionic potential, reducing the bonding-antibonding splitting. The electronic screening is a fast process, whose relaxation dynamics is related to the Auger-like recombination of the free carriers.

To second effect is that the reduced strength of the covalent bond, due to the screening processes, allows the ions to move towards new meta-stable positions. With a sudden deformation of the lattice that can persist up to the pico-second time domain.

The band gap collapse is mainly due to the charge transfer and the consequent modification of the band structure. Therefore, the electronic properties seem to play, in this case, a dominant role, respect to the coherent vibrational modes responsible of the IM-PT in organic compounds.

3.5 Laser induced transient effects

For a system perturbed by a coherent laser pulse it is important to distinguish two possible behaviours. The appearance of a phase transition is, in fact, possible only for systems which manifest two (or more) phases. In general phase transitions can be achieved by increasing the internal energy of the system or, more specifically, by the changing of the order parameter of the system.

The same change can be produced also through a laser pulse, via the macroscopic heating of the sample, or via the creation of a new meta-stable crystal structure.

4. Properties of $CuGeO_3$

4.1 Crystalline Structure

Copper oxide based compounds can show different physical properties ranging from the Mott insulators [24] to superconductor [1, 24, 30] to spin-Peierls transition [3]. Despite this variety of properties, it is possible to find common elements in their crystalline structure such as a copper ion coordinated with six oxygen ions, forming a regular or irregular octahedron. The base of the octahedron is formed by a Cu ion coordinated with four oxygen ions (O(2) in Fig. 4.1). These five ions can be viewed as a plaquettes which can share one corner or one edge with the CuO_4 neighbouring unit [19, 30, 24]. The tri-dimensional structures, resulting from these two different crystallographic arrangements, are known as edge-sharing or corner sharing.

In high temperature superconductors (HTSC's) the CuO_4 units share the corners [30, 41], instead in $CuGeO_3$ they share the edges [19, 43, 47]. Figure 4.2 (a) shows corner sharing plaquettes in $La_{2-x}Sr_xCuO_4$, whereas $CuGeO_3$ is shown in Fig. 4.2 (b) Important is to note that in $CuGeO_3$ the sequence of plaquettes do not form plane but chains (see Fig. 4.2 (b)).

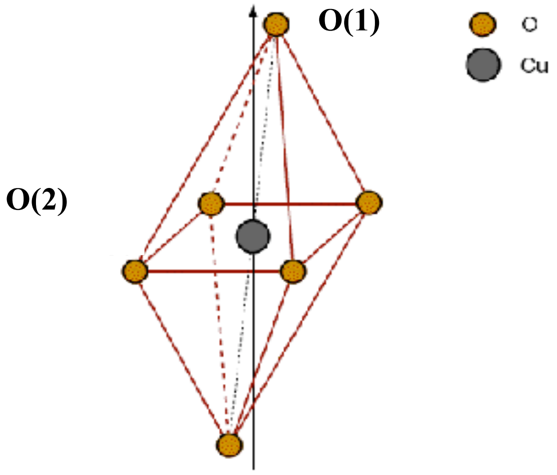

Fig. 4.1- *details of the distorted-elongated octahedron.O(1) is the apical oxygen atom, O(2) belongs to the square plaquette [45].*

For this reason edge sharing systems such as $CuGeO_3$, Li_2CuO_2, $La_6Ca_8Cu_{24}O_{41}$, Ca_2CuO_3, Sr_2CuO_3) exhibit strong one-dimensional behaviour [24].

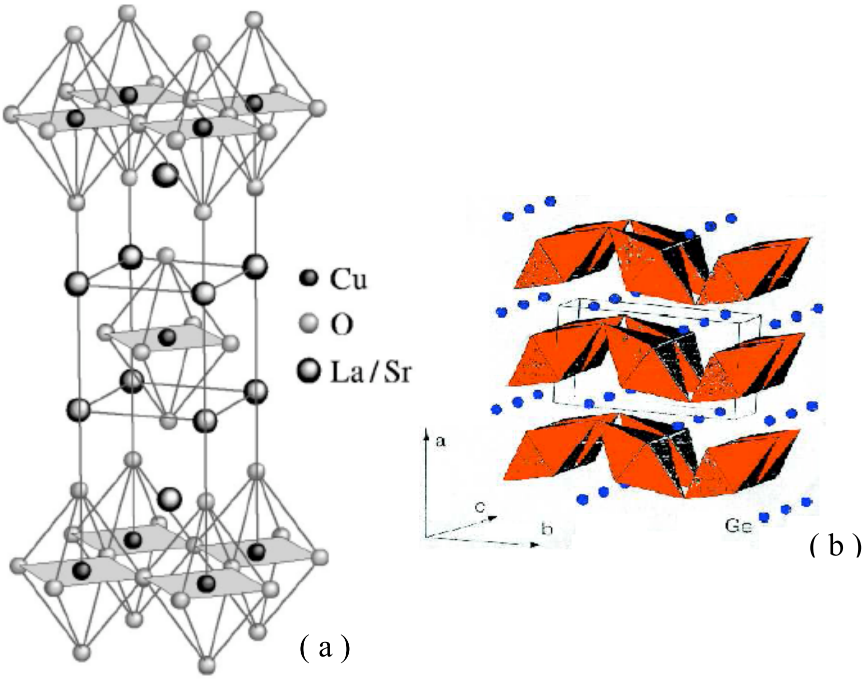

Fig. 4.2 (a, b)- *On the left (a) crystalline structure of the* $La_{2-x}Sr_xCuO_4$*, superconductive cuprate formed b corner sharing plaquettes [30, 41]. On the right (b) the crystalline structure of* $CuGeO_3$*; along the c axe edge sharing octahedrons stack [19].*

The $CuGeO_3$ has an orthorhombic unit cell belonging to the space groups Pbmm (x//*a*, y//*b*, z//*c*) [43] (see Fig. 4.3). At room temperature the lattice parameters are $a = 4.81$ Å, $b = 8.47$ Å and $c = 2.94$ Å

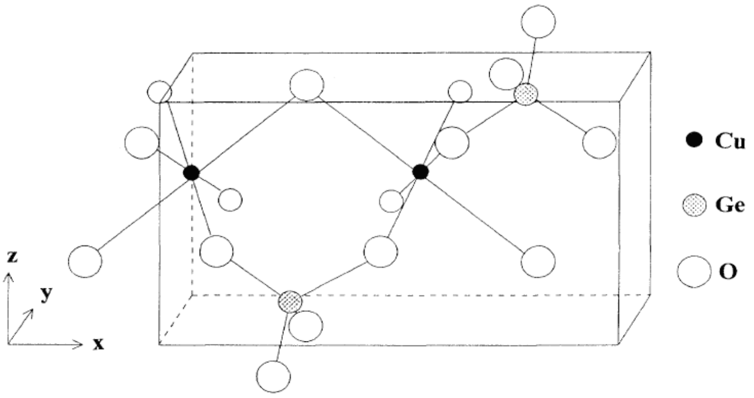

Fig 4.3- *Schematic representation of the* $CuGeO_3$ *crystal structure [44].*

The copper ion at the centre of a plaquette is coordinated with two other oxygen ions along the "*z* direction" (apical oxygen O(1) in Fig. 4.1) forming a distorted-elongated octahedron (Fig. 4.1 and Fig. 4.3).

The Cu-O(1) bond length is 2.76 Å whereas the Cu-O(2) bond length is 1.94 Å [19]. The presence of two different Cu-O bonds plays an important role for the crystal field effects.

The second building block of the $CuGeO_3$ is the tetrahedron formed by Ge and four O. The Ge-O(1) bonds are all equivalent and the O-Ge-O angle is close to 108.9° (Fig. 4.2 (b)).

4.2 Electronic and magnetic properties

The magnetic properties of the copper oxide compounds are strongly influenced by the values of Cu-O-Cu angle (θ angle). In cuprate superconductors, for example, the corner sharing chain allows two copper ions to sit along the same direction($\theta = 180°$), instead θ is ~98° in $CuGeO_3$.

Different spatial orientations of the copper and oxygen ions make possible different hybridization of the bonds. In the edge sharing geometry the O *2p* orbitals hybridize with the Cu *3d* orbitals, and $\theta \sim 90°$. In the corner sharing chain the O *2p* orbital hybridizes with the two neighbouring copper *3d* orbitals. Therefore, the effective overlapping between neighbouring Cu $d_{x^2-y^2}$ orbitals through O ions is rather small if θ is close to 90°. The vanishing of the effective hopping integral (t) is characteristic of the edge-sharing chains.

The model Hamiltonian used to describe the electronic structure of edge-sharing Cu-O chain is the known as three bands Hubbard hamiltonian [46].

$CuGeO_3$ is classified as CT insulator, with $\Delta < U_d$. In Fig. 4.4 the schematic density of state is shown.

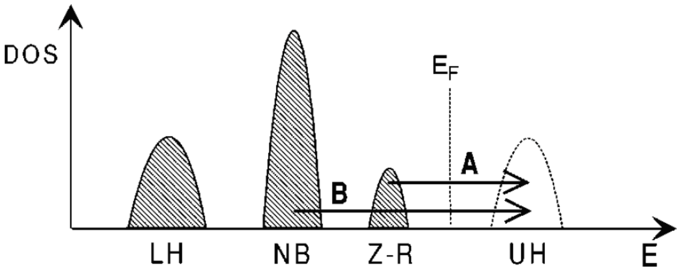

Fig. 4.4- *Schematic density of states for the CT insulator. LH is the lower Hubbard band, while UH is the upper Hubbard band, NB is the non-bonding 2p band, ZR is the Zhang-Rice local singlet band.* E_F *is the Fermi energy. The labels* ***A*** *and* ***B*** *denote the process of optical inter-band excitations [46].*

The energy gap is determined by the interband excitation from the Zhang-Rice singlet (Z-R) band to the upper Hubbard (UH) band as shown in Fig. 4.4. In general, the Z-R singlet is formed by an antiferromagnetic coupling between a 3*d* hole of Cu and another hole, delocalized between the O 2*p* orbitals of the four oxygen ions belonging to the same CuO_4 plaquette, as shown in Fig. 4.5.

The oxygen hole can be introduced by a photo-induced charge-transfer process. In this case, an electron transfer from an O 2*p* orbital to the Cu ion creates a hole on the O ion, and this hole is coupled to the Cu 3*d* hole of the neighbouring plaquette to form a spin singlet.

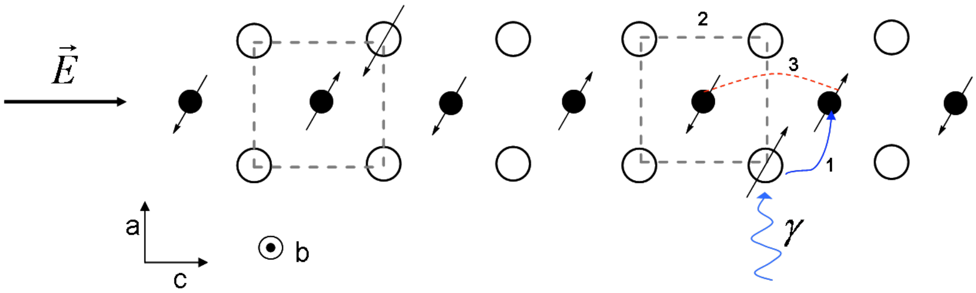

Fig. 4.5- *Zhang-Rice (Z-R) singlet formation:* ***1-*** *the transfer of an electron from an O 2p to a Cu 3d orbital with an absorption of a photon;* ***2-*** *the hole on the O ion can couple to the hole on the neighbour Cu ion to form the Z-R singlet.*

This bound state can be induced only when the laser light polarization is parallel to the *c* crystal axis, whereas a light polarized parallel to the *b* crystal axis excites only the CT along the apical direction of the CuO_6 distorted octahedron [19, 43].

In the framework of the three bands Hubbard hamiltonian, the value of the charge transfer energy (Δ) can be expressed as

$$\Delta = \frac{\Delta V_m}{\varepsilon_\infty} + \Delta_0 \quad . \qquad 4.1$$

ΔV_m is the difference in the Madelung site potential for a hole between Cu and O sites, ε_∞ is the dielectric constant and Δ_0 is linked to the second ionization energy of the Cu^{2+} ion, and to the second affinity of the O^{2-} ion.

For chain systems such as Li_2CuO_2, the CT energy gap is ~2.2 eV. In $CuGeO_3$ the energy gap is ~3.5 eV. The origin of this larger gap resides in the larger value of ΔV_m. This higher value could be due to the fact that O(1)-Cu-O(1)-Cu-O(1) bonds are alternatively tilted of about 60°. As a result the Ge^{4+} ions are very close to the O(1) ions.

In term the magnetic properties $CuGeO_3$ is an anomalous system. In fact the Goodenough-Kanamori-Anderson rule states that, for θ close to 90°, the spin exchange interaction between two nearest neighbour copper ions should be ferromagnetic. Whereas for θ close to 180° the next nearest neighbour interaction is anti-ferromagnetic [47, 48, 49]. The $CuGeO_3$ compound doesn't follow this rule, showing an anti-ferromagnetic order, despite of having $\theta \sim 98°$.

In order to understand the origin of this peculiar magnetic property it is necessary to take into account the exchange interactions between nearest neighbouring (J_1) and the next nearest neighbouring (J_2). For an edge sharing system, as $CuGeO_3$, J_1 can be AFM (anti-ferromagnetic) or FM (ferromagnetic) depending on θ. The FM contribution is caused by the direct exchange mechanism between Cu *3d* and O *2p* orbitals (K_{pd}) and the Hund coupling of two O *2p* orbitals (K_p). The AFM contribution is due to the Anderson's super-exchange mechanism and it is made possible by the strong hybridization of the Cu *3d* and O *2p* orbitals.

If $\theta \sim 90°$, the absence of common O *2p* orbitals linking two different Cu ions makes the super-exchange term vanishing. For increasing θ the AFM contribution will also increase [46].

There is a "special angle" at which the FM and the AFM contributions compensate. In this case it is necessary to introduce the J_2 contribution, which is always AFM.

Theoretical calculations [50] give evidence that $\theta \sim 98°$ is not sufficient to enter in the range of the "special angle" at which the AFM and FM contributions to J_1 compensate themselves. Damascelli *et al.* [51] explain the AFM behaviour as a "side group" effect, in which the presence of the Ge^{4+} ion plays a fundamental role. The Ge-O hybridization introduce a difference in the oxygen p_x and p_y orbitals, that are not equivalent any more, and the cancellation of the AFM contribution, due to the K_{pd} FM term, is no longer complete.

Both the "anomalous" magnetic property and the large CT gap seem to be strongly linked to the particular-critical Cu-O-Cu angle, and to the presence of the Ge^{4+} ion near the in-chain oxygen atoms.

4.3 Crystal field effects

The *d*-like orbitals of copper in $CuGeO_3$ are not energetically degenerate, because of the presence of the interaction of the Cu ions with the neighbouring oxygen ions. This effect is well described by the crystal field model.

In this model the ions are seen as point-like sources of charge. All the charge-sharing due to bonds between atoms is neglected.

For an octahedral system the field of the neighbouring oxygen ions has a cubic symmetry which divides the fivefold degenerate *3d* orbitals into two distinct representations with T_{2g} and E_g symmetry. The twofold degenerate E_g states contain orbitals which point towards the centre of the cube faces. Consequently the E_g states interact more strongly with the ligand ions. Instead the three T_{2g} orbitals point towards the corner of the cube and the interaction with the octahedral ligand ions is smaller.

Representation	Orbital name	Atomic states	Cartesian notation
E_g	d_{z^2}	$\vert 20\rangle$	$\frac{1}{2}(3z^2 - r^2)$
	$d_{x^2-y^2}$	$\frac{1}{\sqrt{2}}\vert 2\bar{2}\rangle + \frac{1}{\sqrt{2}}\vert 22\rangle$	$\frac{\sqrt{3}}{2}(x^2 - y^2)$
T_{2g}	d_{xy}	$\frac{1}{\sqrt{2}}\vert 2\bar{2}\rangle - \frac{1}{\sqrt{2}}\vert 22\rangle$	$\sqrt{3}(xy)$
	d_{yz}	$\frac{1}{\sqrt{2}}\vert 2\bar{1}\rangle + \frac{1}{\sqrt{2}}\vert 21\rangle$	$\sqrt{3}(yz)$
	d_{zx}	$\frac{1}{\sqrt{2}}\vert 2\bar{1}\rangle - \frac{1}{\sqrt{2}}\vert 21\rangle$	$\sqrt{3}(zx)$

Table 4.1- *Schematic effect of a cubic ligand field on 3d electrons. The five ligand states are described in term of their atomic constituting functions. In the last column the atomic symmetries are projected to cubic symmetry [52].*

Table 4.1 shows the five d-orbital and the effect of the ligand field [52].

The energy splitting of the single *d* electron level is set equal to $10D_q$, where D_q is the cubic field strength parameter. If the ligands are considered as point-like charges the value of D_q is estimated using the following approximation [19]

$$D_q = \frac{1}{6}\frac{q}{R^5}\bar{r}^4 \quad ; \qquad 4.2$$

where *R* is the Cu-O distance.

The distortion of the octahedral symmetry is treated as a perturbation of the d-orbital.

Within this perturbation the tetragonal (D_{4h}) field of the $CuGeO_3$ does not distort the orbitals, but it changes their relative energy. Therefore the E_g and T_{2g} orbitals are further split in four states with symmetries: A_{1g} B_{1g} B_{2g} and E_{2g}, as shown in Fig. 4.6.

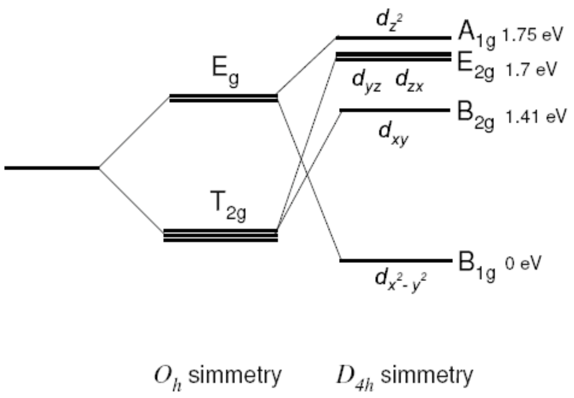

***Fig. 4.6-** Crystal field splitting of a d orbital in the O_h and in the lowest D_{4h} symmetry [45].*

The new orbital energies depend on the splitting parameters D_s and D_t defined through the radial integrals [19]

$$D_s = \frac{2}{7}\left(\frac{1}{R_0^3}-\frac{1}{R_l^3}\right)\int_0^\infty R_{0,l}^2(r)\,r^2 r^2\,dr \quad ; \qquad 4.3\,(a)$$

$$D_t = \frac{2}{21}\left(\frac{1}{R_0^5}-\frac{1}{R_l^5}\right)\int_0^\infty R_{0,l}(r)\,r^4 r^2\,dr \quad ; \qquad 4.3\,(b)$$

where R_l and R_0 are the Cu-$O_{\text{In plane}}$ and Cu-O_{apical} distance.

In Fig. 4.7 the *d* orbitals are presented (in the non-distorted spherical symmetric potential).

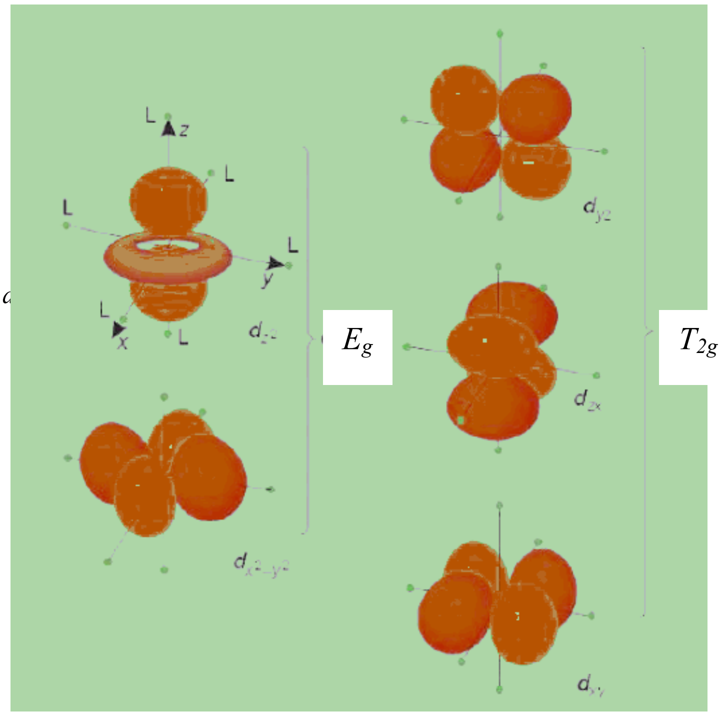

***Fig. 4.7-** E_g double degenerate*

atomic potential [19].

The *d-d* energy split has been deeply studied in a series of different copper oxides by *ab-initio* methods using cluster model calculation by Broer and Coen de Graf [53]. These authors interpreted the absorption peak observed in the 1.40eV - 2.10eV spectral range (see Fig. 4.8 [19]) as d-d phonon assisted transitions [42].
Evidence of the fact that these transitions are associated to the presence in the sample of phonons is the temperature dependence of the absorption spectra [19].
Fig. 4.8 shows the temperature dependence of the optical absorption peaks assigned to the *d-d* transitions in $CuGeO_3$, in the temperature range between 15 K and room temperature.

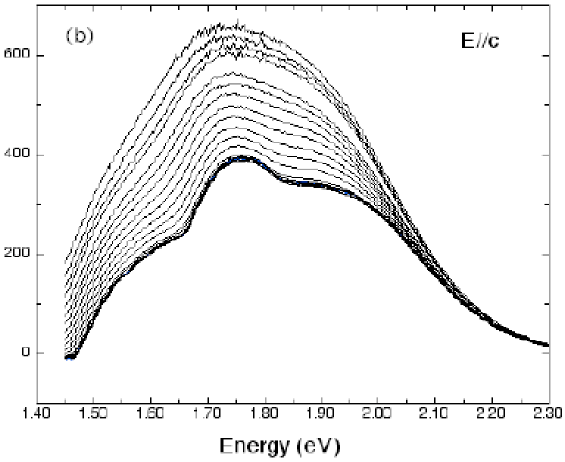

Fig. 4.8- *Temperature dependence of d-d transitions in $CuGeO_3$, from T = 15 K (bottom curve) to room temperature (top curve) with light polarized parallel to the c-axis.*

At low temperature the absorption spectrum consists of three gaussian-like components [19, 43]. On the basis of the crystal field method, it is argued that the three gaussians correspond to transitions from the lower energy laying state $3\,d_{x^2-y^2}$ to the first (d_{xy}), the second (d_{yz}, d_{zx}) and the third (d_{z^2}) higher energy states.

Since the cluster calculations are performed on different copper oxides, Broer and Coen de Graf and [53] investigated the change in the energy position of the *d-d* transitions for different geometries and different copper coordination. They concluded that the transition in which the hole is transferred from the $3d_x{}^2\text{-}{}_y{}^2$ to the $3d_z{}^2$ can varies from 1 eV to 2 eV, relating with the copper coordination and with the different ratio between the lengths of the Cu-O(1) and Cu-O(2) bonds.
The dependence of the *d-d* transition energy on the positions of the ions will be further discussed in the following, as a key property in order to interpret the time-dependent photo-excited optical spectra measured and studied in this work.

5. Experimental set-up

5.1.1 The laser oscillator

The light source is an amplified Ti:Sapphire laser system (see Fig. 5.1).

A $Ti:Al_2O_3$ (titanium sapphire - Ti:Sa) oscillator produces laser pulses with a wavelength tuneable in the 760 nm and 850 nm range, a bandwidth of ~ 47 nm, a pulse duration of ~ 20 fs, at a repetition rate of 76 MHz and an average power of ~350 mW [54] .

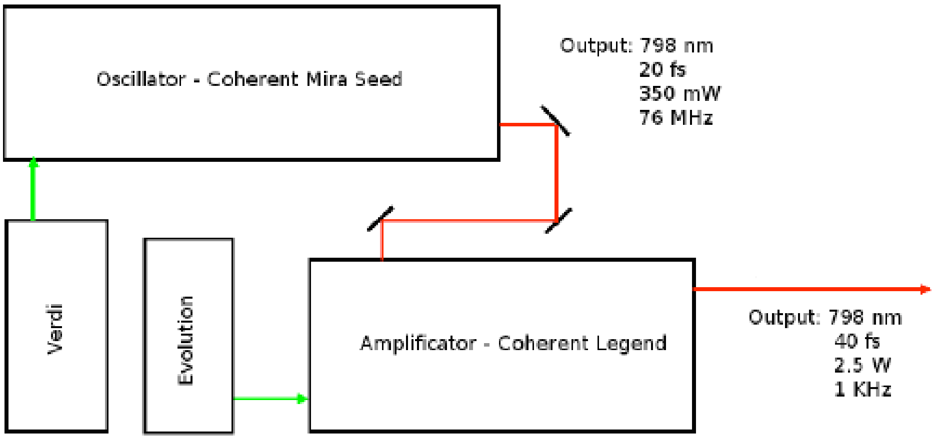

Fig. 5.1- *Scheme of the laser system. The Ti:Sa crystal in the oscillator cavity (76MHz repletion rate, 350 mW average power) is pumped by the continuous Neodymium Vanadate* ($Nd:YVO_4$) *laser. The mode-locked laser light enters the amplifier, whose Ti:Sa crystal is pumped by a 1KHz impulsive Neodymium Vanadate* ($Nd:YVO_4$) *laser. The amplified laser light has average power equal to 2.4 W and 1 KHz repetition rate [56].*

The lasing medium is pumped by a continuous laser with an average power of 5 W at a wavelength of 532 nm.

The electromagnetic modes allowed by the cavity have a wavelength λ related to the cavity length, L, by the relation

$$\lambda = \frac{2L}{n} \quad ; \qquad 5.1$$

hence several modes are allowed, however the generation of ultra-short impulses requires a mode-locking condition, i.e. a constant phase difference between the (n)-th mode and the ($n+1$)-th mode [56].

In general, Ti:Sa lasers use a passive mode-locking, based on the Kerr Lens Mode-locking mechanism.

The Kerr lens effect consists in a variation of the refractive index (η) of a material, proportional to the intensity (I) of the light travelling trough the active medium [55]. The dependence of the refractive index on the beam intensity, $\eta(I)$, is expressed by

$$\eta(I) = \eta_0 + \eta_2 I \quad . \qquad 5.2$$

Where η_0 is the constant part of the refractive index and η_2 is the non-linear term.

Assuming a laser pulse time structure gaussian, with σ proportional to the gaussian FWHM, the time dependent intensity, $I(t)$, is

$$I(t) = I_0 e^{-\frac{t^2}{\sigma^2}} \quad . \qquad 5.3$$

As a consequence the refractive index variation is expressed by

$$\frac{d\eta(I)}{dt} = -I_0 \frac{2\eta_2 t}{\sigma^2} e^{-\frac{t^2}{\sigma^2}} \quad . \qquad 5.4$$

The change in the refractive index induces an effect of self phase modulation (SPM). From eq. 5.4, knowing L, λ_0 and ω_0 (the frequency and the wavelength of the mode, respectively) it is possible to calculate the time-dependent phase variation ϕ_0

$$\phi_0(t) = \omega_0 t - \frac{2\pi}{\lambda_0}\eta(I)L \quad . \qquad 5.5$$

Since the electric field, $\overline{E}(t)$, in the cavity is given by the sum over all the cavity allowed modes

$$\overline{E}(t) = \overline{E}_0 \left(\sum_{i=-m}^{m} \exp(i\ k\ (\Delta\omega + \phi_i(t))) \right) \cdot \exp(i\ \omega_0\ t) \qquad ; \qquad 5.6$$

where $\Delta\omega$ is the frequency difference between the (N)-th mode and the (N+1)-mode, the laser intensity results

$$I \cong \frac{\sin^2\left[(2N+1)\cdot\frac{\Delta\omega+\phi}{2}\right]}{\sin^2\left[\frac{\Delta\omega+\phi}{2}\right]} E_0^2 \qquad ; \qquad 5.7$$

where N is the number of mode-locked modes, and ϕ is the constant phase difference between the N-th mode and the (N+1)-th mode. Therefore the maximum laser intensity is proportional to the square of the number of mode-locked modes

$$I_{\max} \cong (2N+1)^2 E_0^2 \qquad . \qquad 5.8$$

The change in the refractive index (eq 5.4) plays the role of a lens, which focuses the pulsed part of the laser light, whereas the continuous mode (CW) is blocked by a suitable pin-hole (see Fig. 5.2).

.

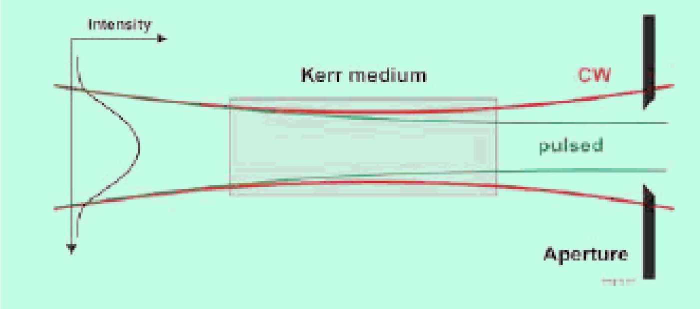

Fig. 5.2- *Kerr-lens effect: inside the Ti:Sa crystal the mode-locked laser light is focus, a small aperture is used to block the continuous laser light (CW) [56].*

Besides the SPM effect another optical non linear effect in the active medium must be considered. In fact, the group (v_g) and the phase velocity (v_f) of the travelling wave, are defined as

$$v_f = \left(\frac{c}{\eta(\omega)} \right) \quad , \qquad 5.9\,(\,a\,)$$

$$v_g = \left(\frac{dk}{d\omega} \right)^{-1} = v_f \left(1 + \frac{\omega}{c} \frac{d\eta}{d\omega} \right)^{-1} \quad , \qquad 5.9\,(\,b\,)$$

are modulated since the crystal refractive index (η) depends on the wavelength of the light. This effect is known as group velocity dispersion (GVD). In a dispersive medium of length equal to l this phase variation results

$$\phi(\omega) = n(\omega)k\ l = k(\omega_0)\ l + \left.\frac{dk(\omega)}{d\omega}\right|_{\omega_0} (\omega - \omega_0)\ l + \frac{1}{2} \left.\frac{d^2k(\omega)}{d\omega^2}\right|_{\omega_0} (\omega - \omega_0)^2 l + \ldots \qquad 5.10$$

the third term representing the phase dependence arising from the GVD effect [55]. In the oscillator the GVD effect is compensated by a pair of prisms. The first prism spatially separates the different wavelengths. The second is used to compensate the different optical paths introduced by the first prism [54].

The SPM effect is of the third order, while the GVD is a second order effect. These two effects have been discussed in details since they play a crucial role for the generation of the super-continuum by the CaF_2 glass, as it will be discussed in details in 5.2.

5.1.2 The laser amplifier

The second stage of the light generation is the amplifier. The laser beam, delivered by the oscillator, travels through a stretcher diffractive grating entering in the regenerative amplifier cavity. In the cavity a Ti:Sa crystal, pumped by a pulsed Nd:YLF_4 laser, at an average power of ~30 W, wavelength of ~527 nm and a repetition rate of 1 kHz, amplifies the laser pulses [57]. The amplification is achieved during several roundtrips inside the active medium. The number of roundtrips, ~20, is controlled by a Pockels cells system. After being amplified the light goes through an optical compressor.

In optimal conditions the amplified pulses have a central wavelength of ~798 nm, an average power of ~2.4 W and time duration of ~50-60 fs. The latter parameter is crucial for the pump-probe experiments, since it determines the time resolution.

5.2 Pump-probe set-up

The pump-probe technique is a time-resolved spectroscopy, based on a stroboscopic effect, allowing observing the time evolution of a system excited by a pump-pulse and probed by a light pulse travelling with a controlled time-delay with respect to the pump.

Fig. 5.3 shows the conceptual scheme of the experimental set-up used for the present experiment. The beam coming from the laser is reflected by two mirrors (M1 and M2) on a pin-hole, used as a reference in the alignment of the system.

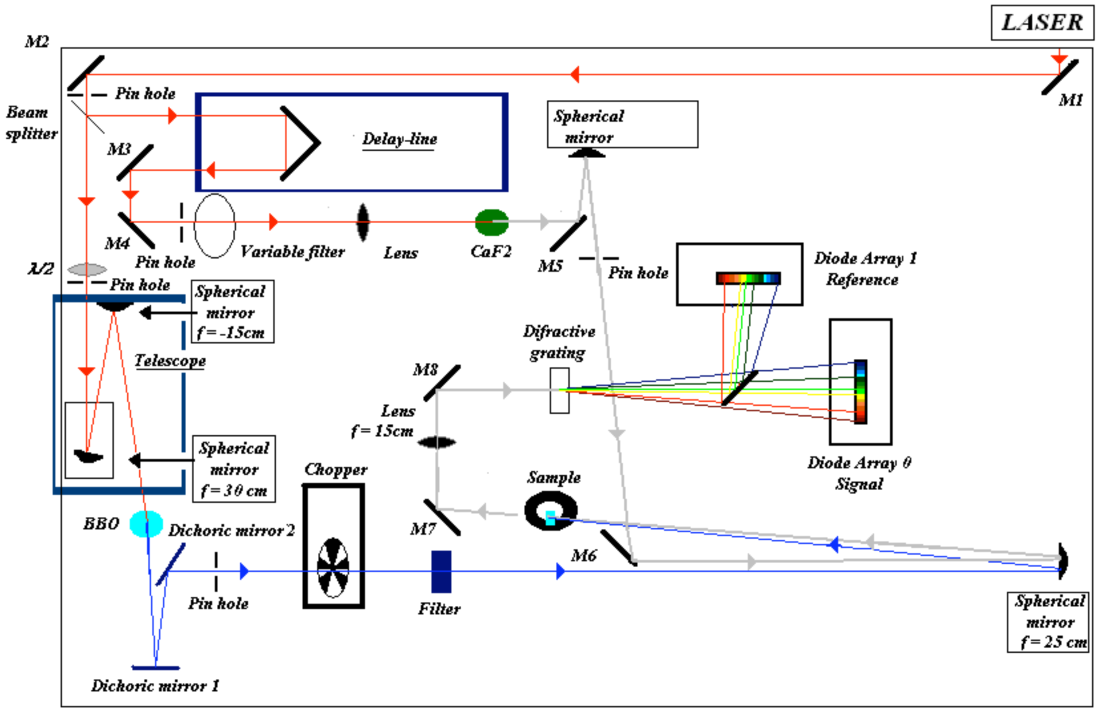

Fig. 5.3- *Scheme of the experimental set-up.*

After the pin-hole a 10%-90% beam splitter divides the beam in two parts. The more intense beam (pump) passes through a telescope, formed by two spherical mirrors with focal length f = 50 cm and f = 25 cm, respectively, then entering in a BBO (Beta Barium Borate) non-linear crystal that generates the second harmonic at ~3.12 eV.

This process has a ~10% efficiency, so the blue pump-beam arrives on two dichroic mirrors with a high reflective coefficient for the 400 nm light, but transparent at the residual "infrared" beam that is filtered out. A $\lambda/2$-plate before the BBO crystal, controls the pump power.

After the second dichroic mirror a 500 Hz chopper synchronized to the laser blocks one pump pulse out of two. The pump beam is then focused on the sample by a spherical mirror with focal length of 25 cm.

The second beam (probe) is reflected by a retro-reflector device, mounted on a remote controlled linear stage. By moving the stage it is possible to control the optical path of the probe, i.e. the time delay between the pump and the probe.

After the delay line two mirrors (M3 and M4) reflect the beam onto a pin-hole and a variable neutral density filter, to control the dimension and the power of the probe pulse. The laser light is then focused by onto the CaF_2 glass. In this material the spectral width of the laser light is broadened by a non linear process known as super-continuum (SC) generation [20]. This non-linear process is originated by the third order (χ^3) non-linear susceptibility term of the material.

For a positive non-linear coefficient ($\eta_2 > 0$) the SPM reduces the frequency of the incoming wave-front light, whereas the tail of the pulse increases the frequency components [20].

The SPM induced frequency spread obtained in the present experiment, as shown in Fig 5.4 (b), spans from ~ 720 nm to ~ 400 nm.

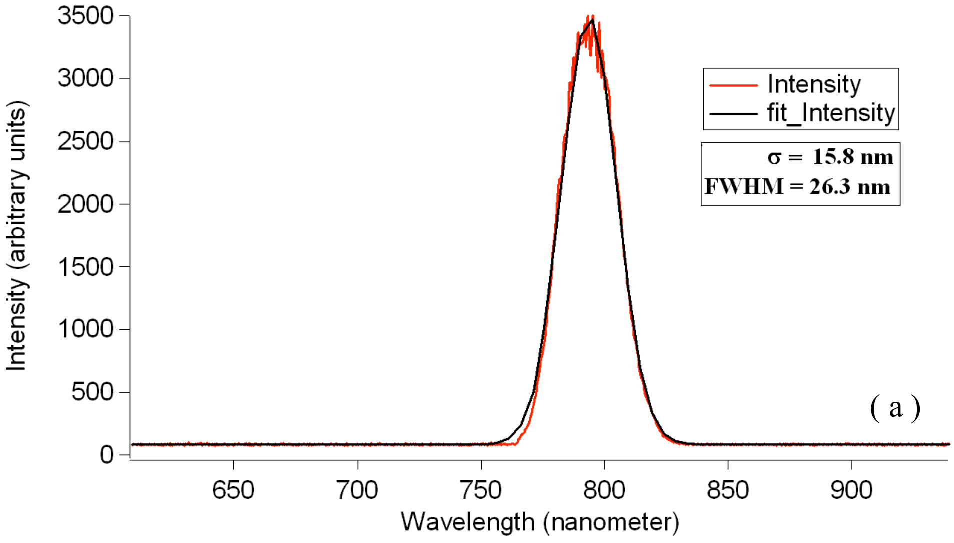

Fig. 5.4 (a)- *Laser light spectrum after the amplifier. The gaussian distribution is centred at 798 nm with a FWHM equal to ~26 nm.*

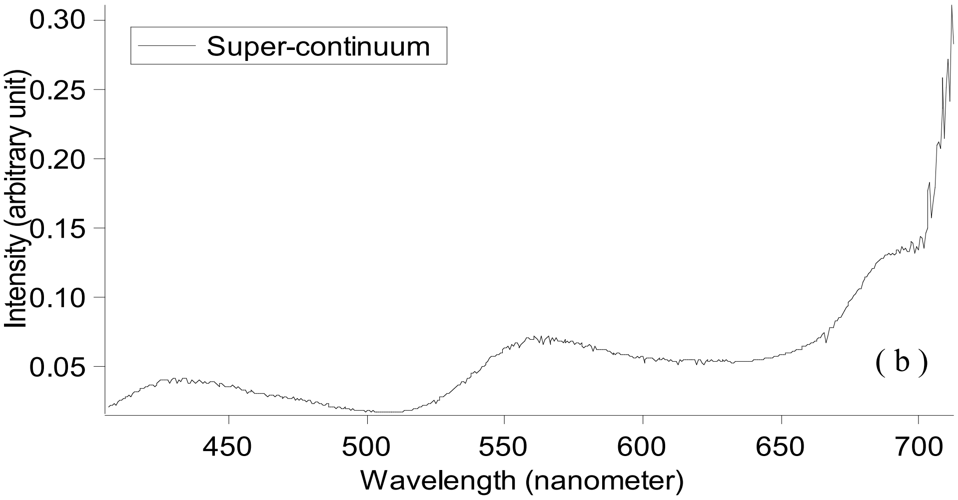

Fig. 5.4 (b)- *Super-continuum laser light spectrum, spreading from ~400 nm to ~720 nm.*

Unfortunately, besides the SC generation in the CaF_2 glass there is also a dispersion of the group velocity (see eqs 5.9 and 5.10). The pulse components having different frequencies propagate with different velocities And it is very important to consider this effect during the data analysis, since different wavelengths of the SC enter the sample at different times.

Since the main goal of the pump-probe technique is to study the time-resolved evolution of the system for different wavelengths, it is necessary to correct the GVD in order to estimate the correct real-time evolution of the system at the different energies [58].

The SC light is then reflected by the mirrors M5, a spherical mirror to re-collimated the light and M6, onto a final spherical mirror, to focus the probe on the sample.

The pump and probe pulses have to be parallel and co-planar as much as possible, to preserve the time-resolution of the experiment.

The SC light transmitted trough the sample is analyzed by a spectrometer. This device is based on two mirrors (M7 and M8) a lens, with focal length equal of 15 cm, and a diffractive grating. Finally, the optimize SC light is detected by a photodiode array (PDA).

5.3 Time superposition and spatial beam profiles

To find the time zero the spatial and temporal overlap of the pump and probe pulses is needed.This overlap is found by replacing the sample with a BBO crystal. The SC pulse is suppressed (by reducing the probe power impinging on the CaF_2), and the sum-frequency between the fundamental (probe) and the second harmonic (pump) beams is detected. When the two beams are properly superposed in time and space, the intensity of the resulting sum-frequency light has a maximum.

It is also important to set both the pump and probe foci on the sample surface. This is achieved by measuring the dimensions of the two spots are measured by a charged-couple-device camera (ccd).

In Fig. 5.5 (a) and 5.5 (b) the spot images of the two beams are shown. For the SC light the dimensions are estimated to be $\Delta x \approx 60$ μm and $\Delta y \approx 60$ μm, for the pump-blue light they are $\Delta x \approx 140$ μm and $\Delta y \approx 140$ μm.

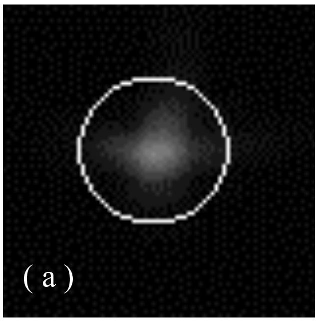

Fig. 5.5 (a)- *Super-continuum probe beam profile.*
($\Delta x \approx 60$ μm and $\Delta y \approx 60$ μm).

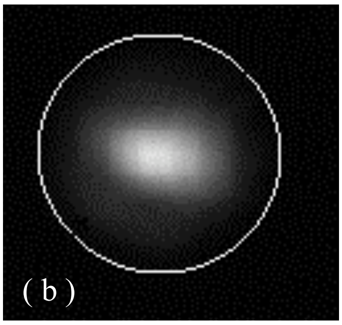

Fig 5.5 (b)- *Pump beam profile.*
($\Delta x \approx 140$ μm and $\Delta y \approx 140$ μm).

Another important parameter is the temporal structure of the laser pulses.

This is measured at the exit of the laser amplifier by detecting the temporal convolution of two laser pulses using an optical auto-correlator. The time duration of the pulse is ~ 56 fs, as shown in Fig. 5.6.

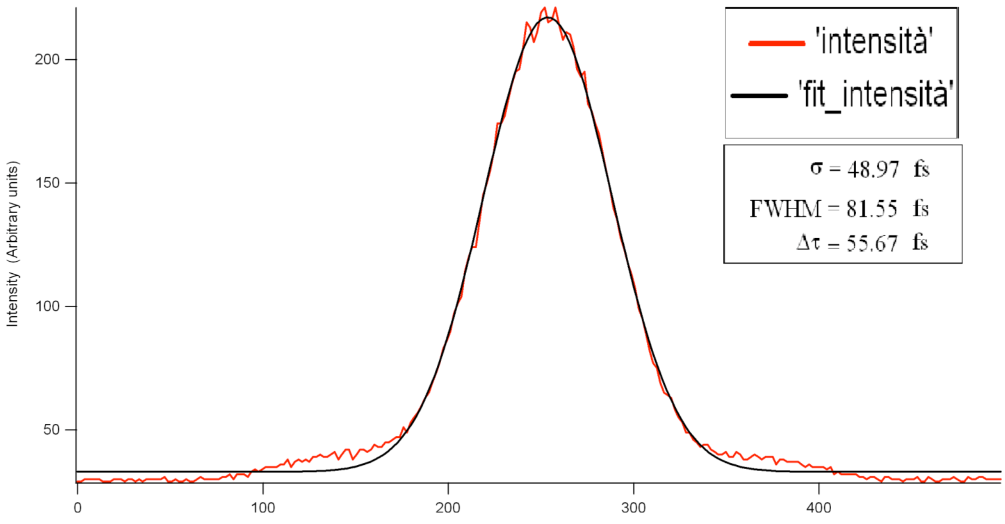

Fig. 5.6- *Temporal beam profile. Along the x axis is reported the time (fs), along the y axis is reported the beam intensity. The gaussian FWM is equal to 81.55 fs. The pulse temporal length is obtained by dividing the FWHM by* $2^{1/2}$*, and it results equal to 55.67 fs.*

5.4 Data acquisition

The measured transmission coefficient is defined as

$$T = \frac{I^{*}}{I} \qquad ; \qquad 5.11$$

where I is the intensity of the incoming SC light, and I^{*} is the intensity of the SC light transmitted through the sample. In order to obtain the information about the perturbation induced by the pump pulse it is important to know T when the system is pumped (subscript p) and un-pumped (subscript u).

The variation of the relative transmission, $\Delta T / T$, is than defined as

$$\frac{\Delta T}{T} = \frac{\left(\frac{I^{*}{}_{p}}{I_{p}} - \frac{I^{*}{}_{u}}{I_{u}} \right)}{\frac{I^{*}{}_{u}}{I_{u}}} \quad . \qquad 5.12$$

Unfortunately, it is not possible to measure simultaneously both the white spectral intensity before and after the sample. To solve this problem two different strategies could be considered.

The first is to collect a reference spectrum, which is then used in all the acquisitions as I_u and I_p. The limit of this method concerns mainly long time-scale instabilities of the laser emission.

The second method uses a second PDA. The SC is split by a 50%-50% “pellicol” beam splitter. One of the two SC spots is the signal (here-after reported with the subscript 0) the second is the reference (subscript 1). The first pulse passes through the sample in temporal and spatial superposition with the pump pulse. The second, that does not go through the sample, is used to measure the shot-to shot spectral intensities I_u and I_p. By defining the signal and the reference measured by the two detectors DDA_0 and DDA_1 respectively, the relative variation of transmission results

$$\frac{\Delta T}{T} = \frac{\left(\frac{I^{*}{}_{0,p}}{I_{0,p}} - \frac{I^{*}{}_{0,u}}{I_{0,u}} \right)}{\frac{I^{*}{}_{0,u}}{I_{0,u}}} = \frac{\frac{I^{*}{}_{0,p}}{I_{0,p}}}{\frac{I^{*}{}_{0,u}}{I_{0,u}}} - 1 = \frac{\frac{I^{*}{}_{0,p}}{C \cdot I_{1,p}}}{\frac{I^{*}{}_{0,u}}{C \cdot I_{1,u}}} - 1 = \frac{\frac{DDA_{0,p} - B_{0,p}}{C \cdot DDA_{1,p} - B_{1,p}}}{\frac{DDA_{0,u} - B_{0,u}}{C \cdot DDA_{1,p} - B_{1,p}}} - 1 \quad . \qquad 5.13$$

In this equation $B_{0,\,u\,(p)}$ and $B_{1,\,u\,(p)}$ are the background signals for the two arrays, with and without the pump pulse, while C is a constant to normalize the reference and the signal SC.

5.5 Synchronization of two photodiode arrays

For every time delay the reference and signal spectra are acquired by the two PDAs and the *ΔT/T* coefficient is measured in real time.

The sorting of the pumped and un-pumped spectra is made using a photodiode (PD) that detects the pump beam after the chopper. The PD signal is also used to measure the pump intensity and to correct possible pump power fluctuations.

To lower the statistical noise, 10^3 shots usually are averaged out.

In the following the system used to synchronize the chopper, the two arrays of photodiode and the photodiode (PD) with the 1 kHz frequency amplifier are briefly described (Fig. 5.7).

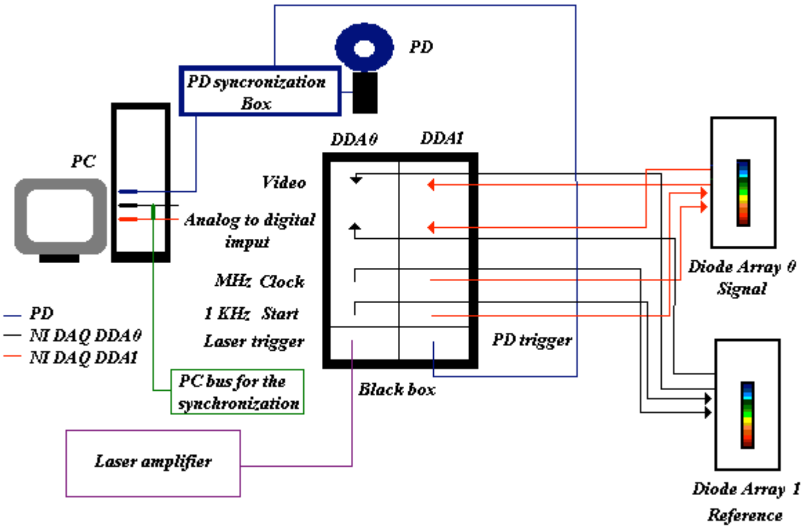

Fig. 5.7- *Scheme of the data acquisition "circuit".*

The laser trigger signal, at 1 kHz, enters the "black box", containing the electronic unit. The trigger is duplicated and synchronized to a 2.5 MHz clock. The former is used as the acquisition start signal, whereas the latter is used as a clock for the PDA electronics.

The two arrays are formed by 512 pixels and they collect the light until the start signal arrives. Then the PDAs start discharging the pixels, one by one, and an analog signal (called video) is emitted and returns back to the black box.

The video is a continuous analog voltage signal, which needs to be digitalized.

The PDAs emit a second signal, which is brought to the black box (analog to digital input) and it informs when the video signal has to be measured by the NI DAQ (National Instruments card M5 series) [59].

The introduction of the second PDA increases the signal-noise ratio up to 10^4. This result has been possible by a link (RTSI Bus signal) between the two NI-DAQs. In this way the two internal clocks of the NI DAQs can be synchronized, providing common MHz outputs synchronized to the laser trigger at 1 kHz.

6. Experimental results

6.1 Unperturbed optical data

Fig. 6.1 reports the absorption spectrum in arbitrary units of the $CuGeO_3$ [19, 43]. Two main absorption regions are clearly detected. The first, between 1.4 eV and 2.1 eV, associated to the d-d transitions, the second, which edge starts at ~3.1 eV, associated to electronic transitions through the band-gap.

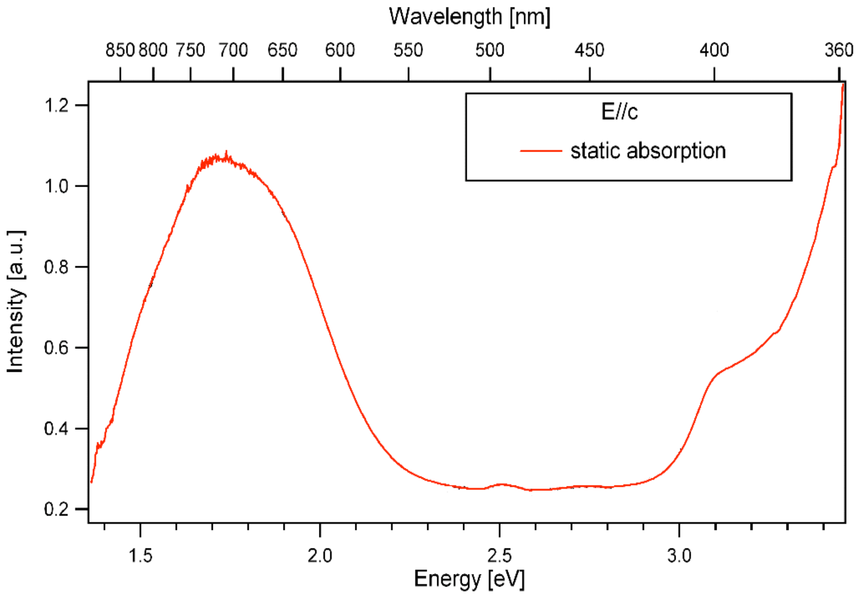

Fig. 6.1- *$CuGeO_3$ absorption coefficient for laser light polarized along the c axe [19].*

The first harmonic of the Ti:Sa laser system, at ~800 nm, can thus be used to photo-induce the *d-d* transitions, instead its second harmonic, at ~400 nm, can be used to photo-induce CT processes from the O *2p* orbitals to the Cu *3d* empty orbitals.

The data reported in the following have been all obtained with both pump and probe light polarized parallel to the *c* crystal axis.

Fig. 6.2 compares the measured trasmittivity of $CuGeO_3$ with the data present in literature [19].

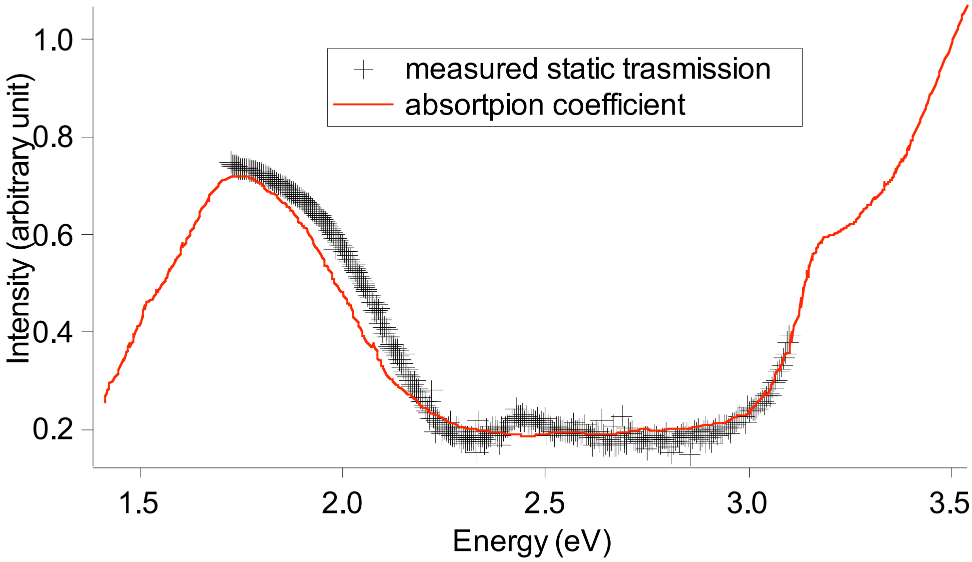

Fig. 6.2- *Comparison between the static spectrum taken with our experimental set-up and the data present in literature [19].*

]

6.2 Time dependent change in trasmittivity

The time-dependent variation of trasmittivity of $CuGeO_3$ is stored in two dimensional data matrice as a function of the probe wavelength and as a function of the time-delay between pump and probe pulses. The variation of trasmittivity, ΔT, has been reported as the variation of the optical density of the medium ΔOD, which is related to ΔT by the following relation [58]

$$\Delta OD = \frac{(\ -1)}{\ln 10} \cdot \frac{\Delta T}{T} \quad . \qquad 6.1$$

Some examples of the data acquired are reported in Fig. 6.3 and Fig.6.4 using a three dimensional surface representation.

In Fig. 6.3 (a) and 6.4 (a) are shown the data set taken with the pump at ~400 nm (with two distinct orientations of the surface in order to see both the fast initial dynamics and the slower relaxation), with a pump power of ~ 4 mW. In Figs. 6.3 (b) 6.4 (b) it is reported the ΔOD induced by the pump at ~800 nm, with a power of ~6.8 mW, in both cases the pump and probe laser light is polarized along the crystallographic *c* axis.

The time delay between pump and probe is in a range between about -200 fs and ~ 2 ps in Figs.6.3 (a) and 6.4 (a), and between about -270 fs and ~ 1.37 ps in Figs.6.3(b) and 6.4(b). The wavelength is in the range between ~ 400 nm and ~720 nm.

For both the pump power energies it is possible to notice a very fast increase in the value of the optical density, as a consequence of the fast increase of the absorption. This process has a characteristic time in the order, or smaller, then the time resolution of our set-up (~ 80 fs).

This very fast dynamic reaches its maximum at the zero-delay time, where the ΔOD value is wavelength dependent, since the fast dynamic has structures in the wavelength domain.

Most noticeable are the two bands with a lorentzian shape, appearing at ~ 420 nm (first band) and at ~ 520 nm (second band).

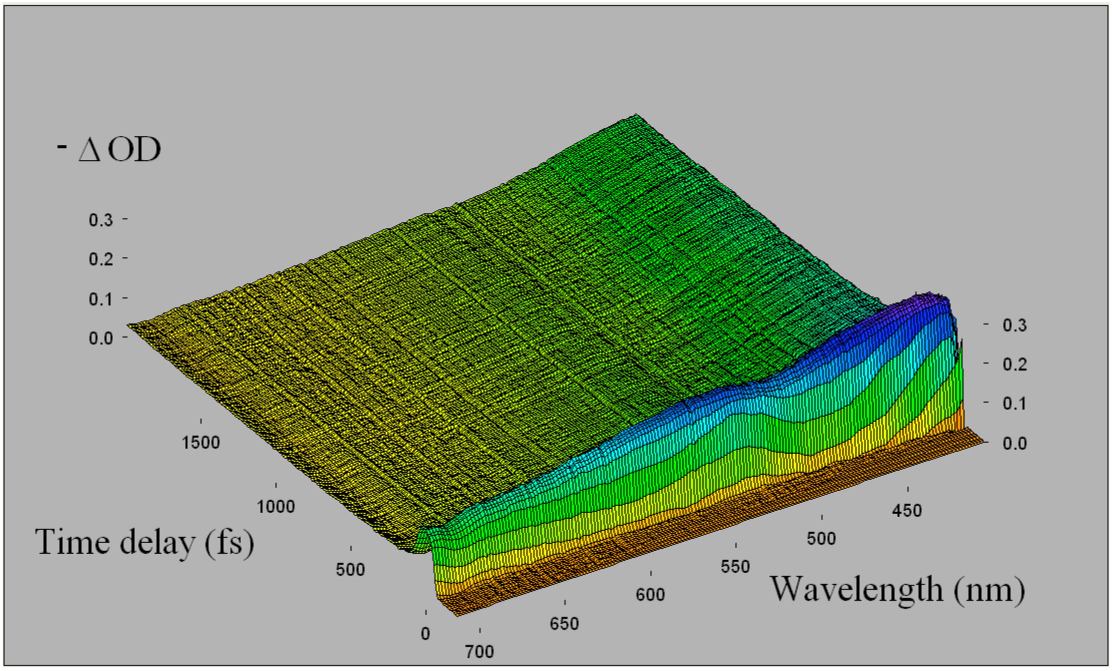

Fig. 6.3 (a)- Three-dimensional surface plot displaying the optical density change induced by the pump light at ~400 nm with pump power equal to ~4 mW. It is visible the fast dynamics.

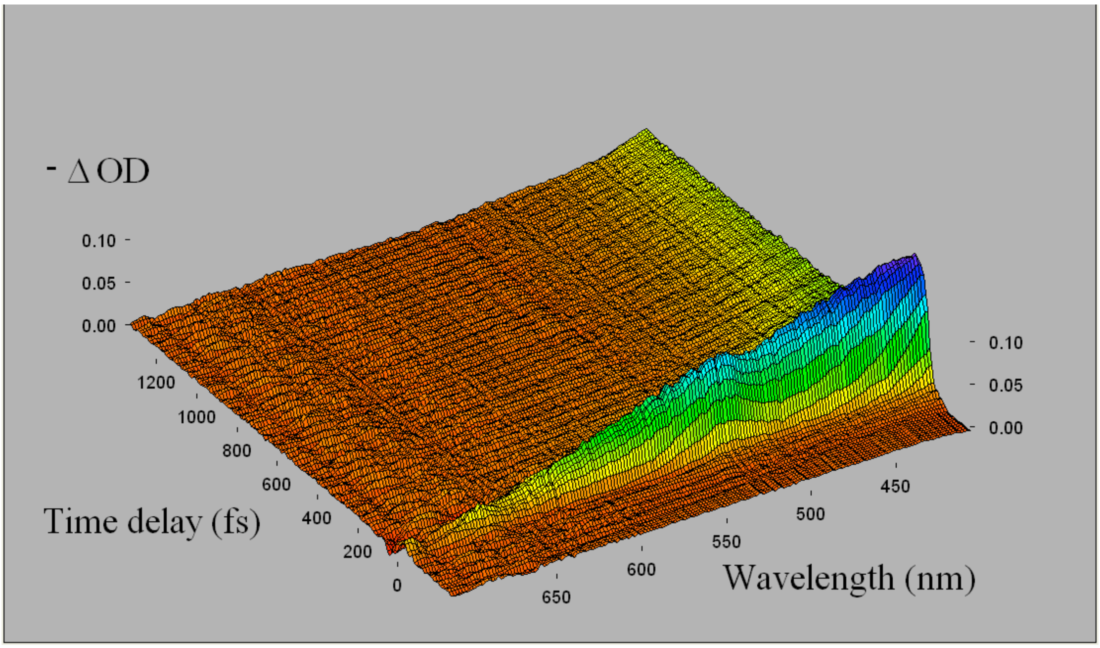

Fig. 6.3 (b)- Three-dimensional surface plot displaying the optical density change induced by the pump light at ~800 nm with pump power equal to ~6.8 mW. It is visible the fast dynamics.

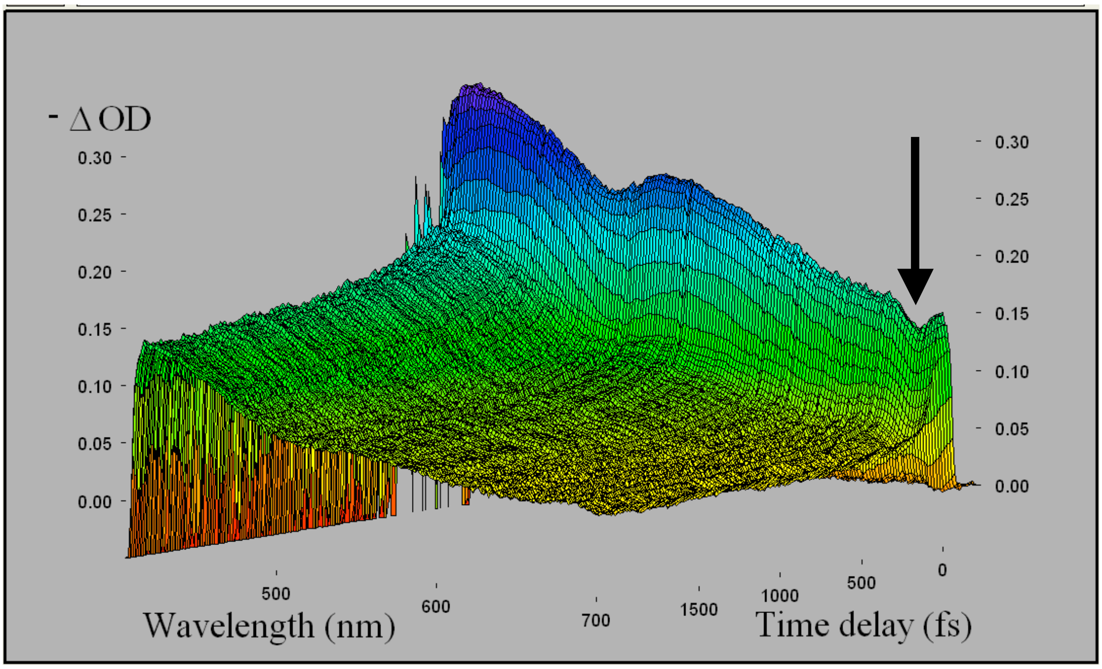

Fig. 6.4 (a)- *Three-dimensional surface plot displaying the optical density change induced by the pump light at ~400 nm with pump power equal to ~4 mW. It is visible the slow relaxation dynamics after the zero time. The black arrow indicates the ~700 nm region.*

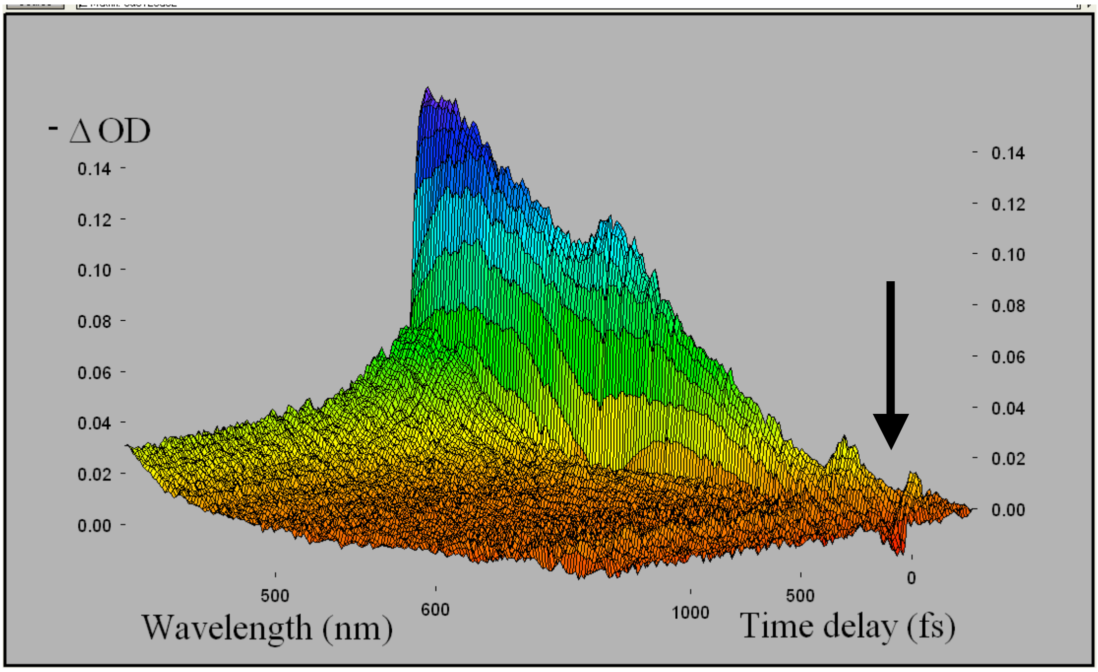

Fig. 6.4 (b)- *Three-dimensional surface plot displaying the optical density change induced by the pump light at ~800 nm with pump power equal to ~6.8 mW. It is visible the slow relaxation dynamics after the zero time. The black arrow indicates the ~700 nm region.*

After the fast increase in the absorption the ~520 nm and ~420 nm bands seem to disappear, and the spectra acquire a structure-less shape. The relaxation slows down and the spectral shape does not show any evolution up to the ps range.

This temporal dynamic is studied through the de-convolution of the kinetic traces, by fitting the data with a proper function.

The presence of two bands at ~420 nm and ~520 nm will be investigated by fitting the transmission variation data with a Lorentz model, to obtain the time dependent dielectric function of $CuGeO_3$.

Another very interesting feature of the fast dynamics is the difference in the optical response in the "red" part of the spectrum (from 600 nm to 720 nm), when the sample is excited at two different photon energies. While for the pump at 800 nm the ΔOD signal is very weak or absent, with the pump at 400 nm the absorption at the red edge ~680-720 nm is much stronger (this effect is indicated by a black arrow in figure 6.4 (a) and 6.4 (b)).

6.3 Pump power dependence of the time dependent trasmittivity change

Measurements of the laser induced change in trasmittivity have been carried out with different pump powers, for the excitation at 400 nm. In order to make a more quantitative analysis, and to make comparable the excitation measurements at 400 nm with those at 800 nm, it is necessary to evaluate the absorbed energy density.

The density of the absorbed energy can be expressed as

$$EnergyDensityAbsorbed\left[\frac{mJ}{cm^3\cdot pulse}\right]=\frac{\langle P\rangle[mW]}{rep.rate[s^{-1}]}\cdot\frac{1}{Area[cm^2]}\cdot(1-R)\cdot\alpha(\lambda)\left[cm^{-1}\right]\quad , \qquad 6.2$$

where P is the pump power, *rep.rate* is the repetition rate of the pump. *Area* is the dimension on the sample and the $\alpha\ (\lambda)$ term is the penetration depth of the laser light. From data reported in literature α, at 400 nm, is ~ 500 cm^{-1}, while at 800 nm is ~525 cm^{-1} [19]. The factor *(1-R)* is introduced in order to consider only the energy going through the sample. The value for the reflection coefficient, for both the pump energies, is equal to 0.1 [51].

The density of absorbed photons can be expressed as

$$n_{photon}=EnergyDensityAdsorbed\left[\frac{J}{cm^3\cdot pulse}\right]\cdot\frac{1}{PhotonEnergy[J]}\quad . \qquad 6.3$$

For example using a 4 mW pump at 400 nm, the absorbed energy density is

$$EnergyDensityAbsorbed\left[\frac{mJ}{cm^3\cdot pulse}\right]=\frac{4mW}{500Hz}\cdot\frac{1}{70^2\cdot\pi\cdot10^{-8}cm^2}\cdot(0.9)\cdot500cm^{-1}\approx23397\left[\frac{mJ}{cm^3\cdot pulse}\right]$$

while the number of absorbed photon is

$$n_{photon}=23.397\left[\frac{J}{cm^3\cdot pulse}\right]\cdot\frac{1}{3.12[eV]\cdot1.6\cdot10^{-19}\left[\frac{J}{eV}\right]}\approx4.687\ 10^{19}\,photons/cm^3\quad ;$$

To evaluate the number of photon absorbed per Cu ion it is necessary to calculate the density of copper ion in $CuGeO_3$. The number of crystal unit cell per cm^{-3} is given by

$$n_{CuGeO_3}=\frac{1[CrystalUnit]}{a\cdot b\cdot c[cm^3]}=8.35\cdot10^{21}\left[\frac{CrystalUnit}{cm^3}\right]\quad , \qquad 6.4$$

since every crystal unit cell contains two different copper ions, the density of copper ions per cm^{-3} is

$$n_{cuION} = 2 \cdot 8.35 \cdot 10^{21} \left[\frac{CrystalUnit}{cm^3} \right] = 16.710^{21} \left[\frac{Copper\ \ ion}{cm^3} \right] \quad . \qquad 6.5$$

Therefore,

$$n_{photon} \Big/ n_{CopperION} = 4.687\ \ 10^{19}\, photons\,/\,cm^3 \Big/ 16.7\ \ 10^{21}\, CopperION\,/\,cm^3 = 0.2807\,\% \quad .$$

Table 6.1 reports the data discussed above for the different pump powers.

Power	4 mW	2 mW	0.5 mW	0.2 mW	800 nm 6.8 mW
Absorbed Enery density (mJ / cm^3 pulse)	23397	11698.5	2924.625	1169.85	42000
Density of photons (fotoni / cm^3)	4.687 10^{19}	2.3435 10^{19}	0.5857510^{19}	0.23435 10^{19}	16.7 10^{19}
Density of photons / Density of copper ions (%)	0.2807	0.14035	0.03508	0.014035	1

Table 6.1- *Absorbed energy density, photon density and photon density vs. copper ion density calculated for the different pump power for the excitation at ~400 nm and at ~800 nm.*

The behaviour of the time dependent *ΔOD* is shown in the Fig. 6.5 (a) – (e).

The horizontal axis reports the time delay between the pump and the probe, instead the vertical axis reports the wavelength. The colour scale represents the change in the optical density. The five images reports the data acquired with excitation wavelength equal to ~ 400 nm, for pump power equal to 4 mW (a), 2 mW (b), 0.5 mW (c), 0.2 mW (d), and the data set for the excitation at ~800 nm with pump power equal to 6.8 mW (e).

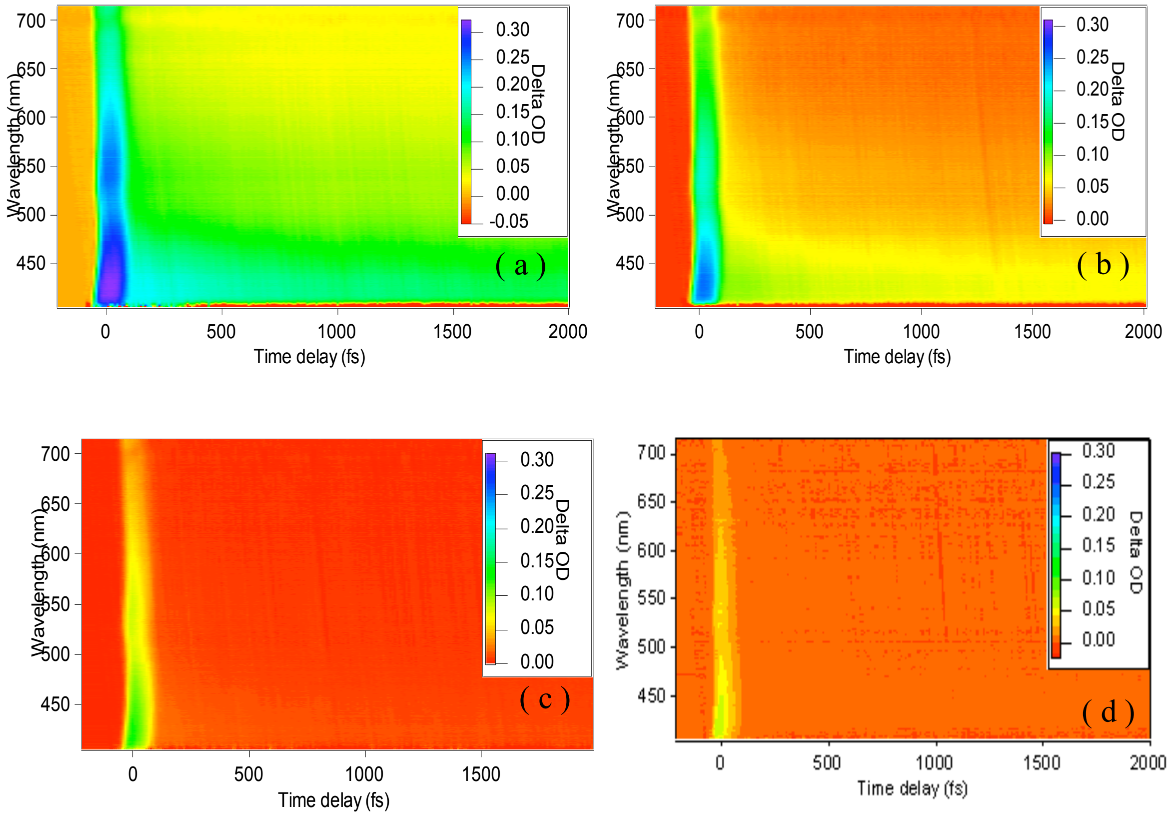

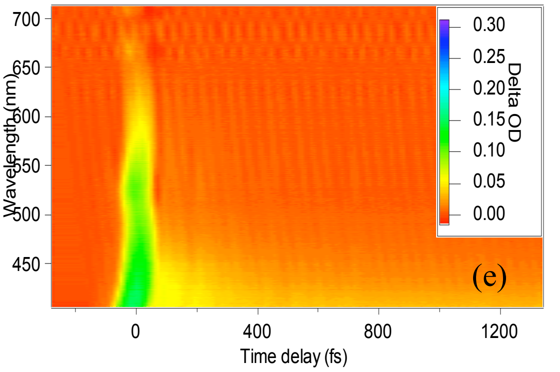

Fig. 6.5 (a - e) *- Image plot of the time-dependent change in the optical density, in the spectral range between ~ 400 nm and ~720 nm, for the excitation at ~ 400nm with power equal to ~ 4 mW(a), ~ 2 mW(b), ~0.5mW(c) and ~ 0.2 mW (d). In the last figure (e) it is reported the data set acquired with excitation at ~ 800nm with power equal to ~ 6.8mW.*

In all the images it is visible the presence, at the zero delay time, of a rapid increase in the absorption, however this effect is not uniform at all the wavelengths.

The dynamics of these bands is better described in the Fig. 6.6 (a) and 6.6 (b), where the stack of different spectra is reported, for different time-delays, and for the data acquired at 4 mW.

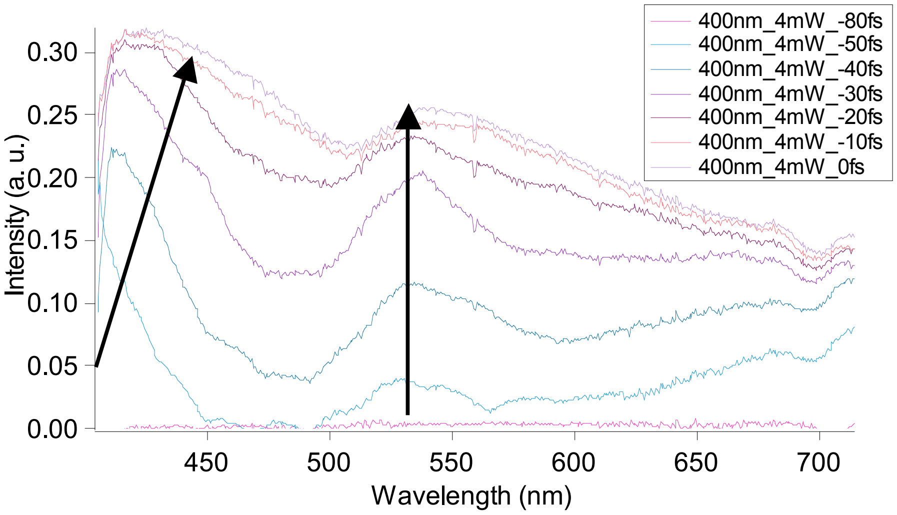

***Fig. 6.6 (a)-** Stack of seven spectra acquired at negative time-delay for the excitation at ~ 400 nm with power equal to ~4 mW. Black arrows indicate the two bands at ~420 nm and ~530 nm. The first band maximum position seems to shift towards higher wavelength values.*

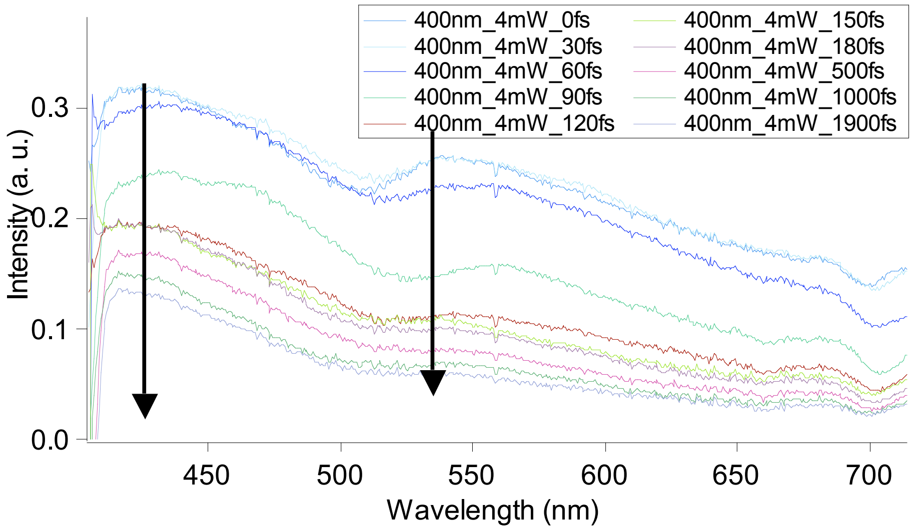

***Fig. 6.6 (b)-** Stack of ten spectra acquired at positive time-delay for the excitation at ~400 nm with power equal to ~4 mW. Black arrows indicate the two bands at ~420 nm and ~530 nm.*

Fig. 6.6 (a) reports the spectra at negative delay time. The fast increasing dynamics is characterized also by the translation of the position of the maximum of the first peak.

Unfortunately, for the spectra taken with negative time delays the maximum of the ~ 410 nm band is out the present experimental range. As the time delay approaches zero the peak moves towards the 450 nm region.

Fig. 6.6 (b) shows the slower relaxation dynamic, while the positions of the two maxima remain the same after the ~ 200 fs. It is worth to observe that the signal intensity remains above zero till the larger delay times achievable with the present experimental set-up (~1.9 ps).

It is important also to point out that the blue edge of the spectra is affected by the pump beam scattered light. In the following the data analysis of these points is not considered.

Besides the spectral behaviour of the signal, discussed so far, it is also interesting to analyze the time dependent optical response.

In Fig.6.7 the time traces, at different wavelengths, are reported.

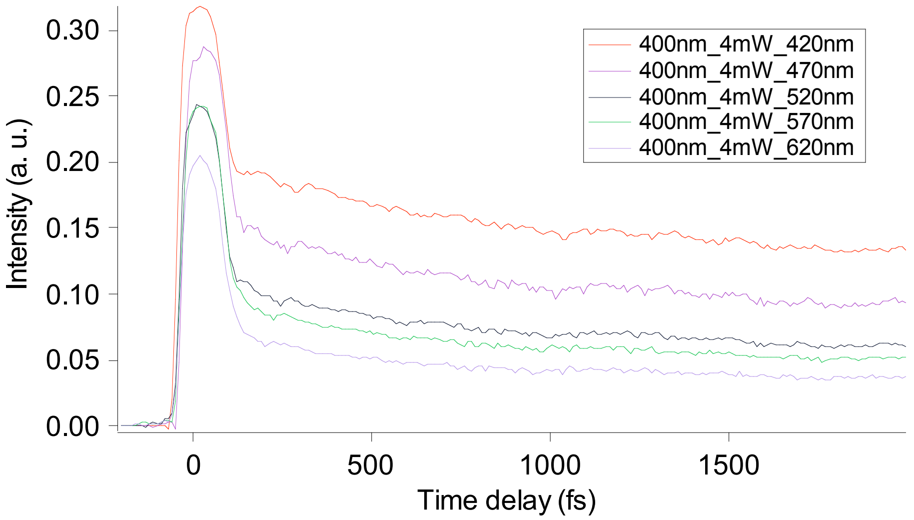

Fig. 6.7- *Stack of five time traces for different wavelength, for the data set acquired with excitation equal to ~400 nm and power equal to ~4 mW.It is visible a fast increase in the absorption, and a slower relaxation dynamics.*

A fast dynamics is visible for all the wavelengths, whereas a slower relaxation follows at the shortest wavelength with a signal quite intense (about half of the maximum) even after 2 ps.

To better understand this short time-scale intensity spectral behaviour and the origin of the long lasting signal, the data are analyzed in terms of the temporal dynamics and spectral behaviour.

7. Data analysis

7.1 Time decay analysis

The temporal dynamics of the optical response relaxation can be obtained by fitting a trace at a certain wavelength with a function that is a convolution between a gaussian, a step function and a suitable number of exponential decays.

The highlights of this fitting procedure are:

1. three relaxation time scales, identified as ultrafast (τ < 100 fs), intermediate (100 fs < τ < 1 ps) and slow (τ > 1 ps), present for all the kinetic traces, wavelengths, pump energies and pump powers.

2. The three decay time constants obtained from the fits are:

◊ $\tau_1 < 30$ fs

◊ 200 fs < τ_2 < 250 fs

◊ $\tau_3 \cong 6$ ps

Fig. 7.1 (a) and 7.1 (b) report some example of the time traces, at different wavelengths, resulting operating the pump at 400 nm using a power of 2 mW and 4 mW, respectively.

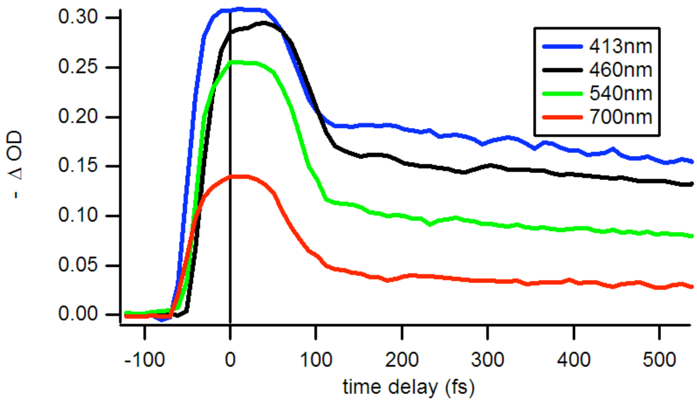

Fig. 7.1 (a)- *four time traces for different wavelengths, for the excitation at ~400 nm with power equal to ~2 mW. After the fast increase in the absorption it is visible a quite constant plateau.*

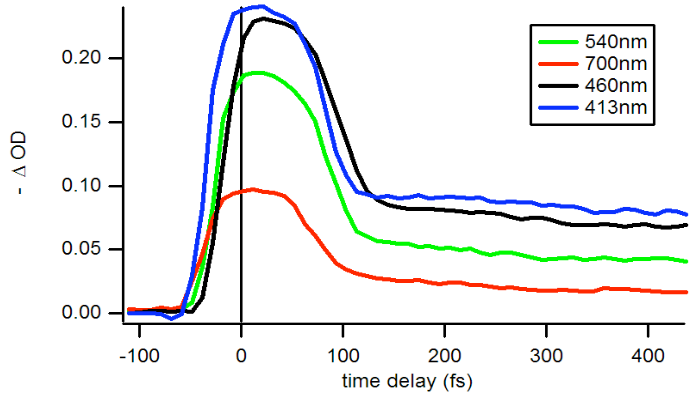

Fig. 7.1 (b)- *four time traces extracted from the data set with pump power equal to ~4 mW.*

Noticeable is the fast increase in the optical density across the zero-time delay. After the zero-time delay, it is possible to observe a quasi-constant plateau, which lasts about 100 fs. Fitting the time-trace with a sum of exponentials gives residuals with a damped oscillatory behaviour (see the upper trace in fig 7.2). The residuals are stored in new matrices as a function of the time-delay and wavelength.

Periodic modulation of the trasmittivity has been already discussed and deeply analyzed by Consani in her master thesis [58]. These residuals have been fitted with a damped cosine function of the form

$$f(t) = y_0 + A\cos\left(\omega\cdot(t-t_0)+\varphi\right)\cdot\exp\left(-\frac{t-t_0}{\tau}\right) \quad , \qquad 7.1$$

being A, ω, τ and φ the fitting parameters, and t_0 is the time when $-\Delta OD$ is maximum.

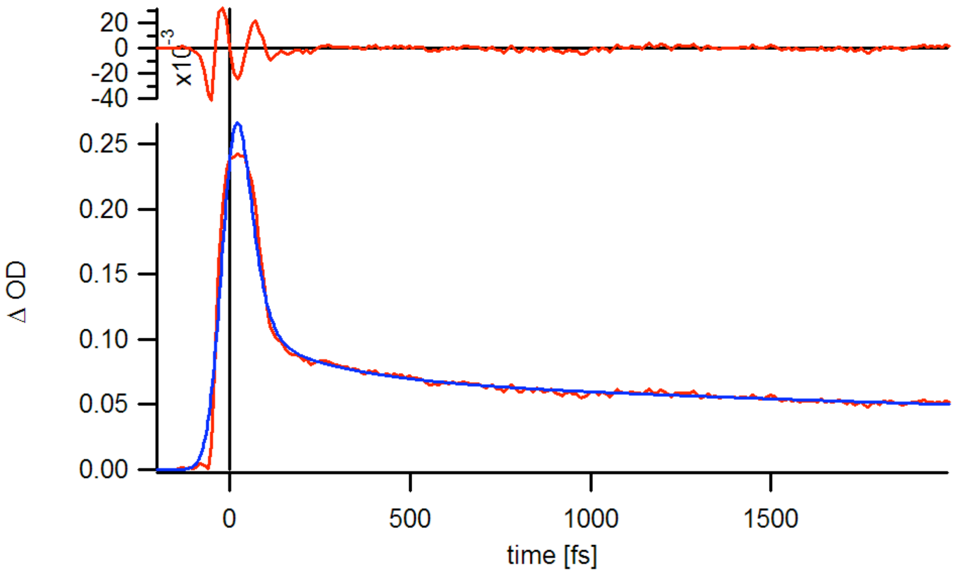

Fig. 7.2- Time trace at 520 nm from the data acquired with pump power equal to ~4 mW It is shown the associated fit and the residual, displaying an oscillating behaviour.

From the value of ω, it is possible to recover the period of the oscillation.

This period is estimated to be of the order of 100 fs, in accordance with the data reported by Consani [58], while the duration of the modulation is between 200-250 fs.

The residual matrices obtained for the pump, at 400 nm and power of 4 mW, is shown in Fig. 7.3

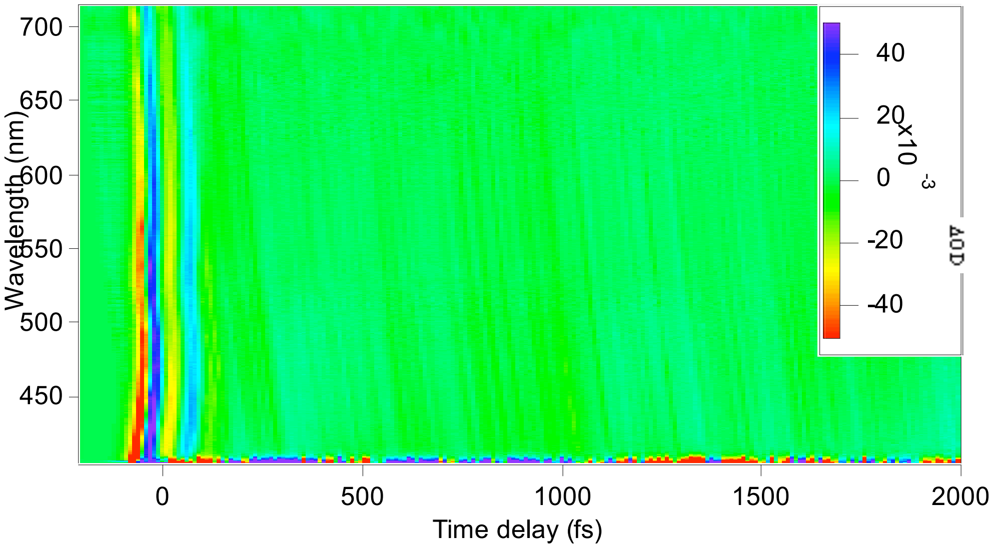

Fig. 7.3- Matrices formed by the fit residuals, reported as a function of the time-delay and wavelength. The data are shown in an image plot, with intensity expressed by the colour scale.

By subtracting the periodic modulation “cleaned” matrices, shown in Fig. 7.4, for the pump at 400 nm and 4 mW of power, are obtained.

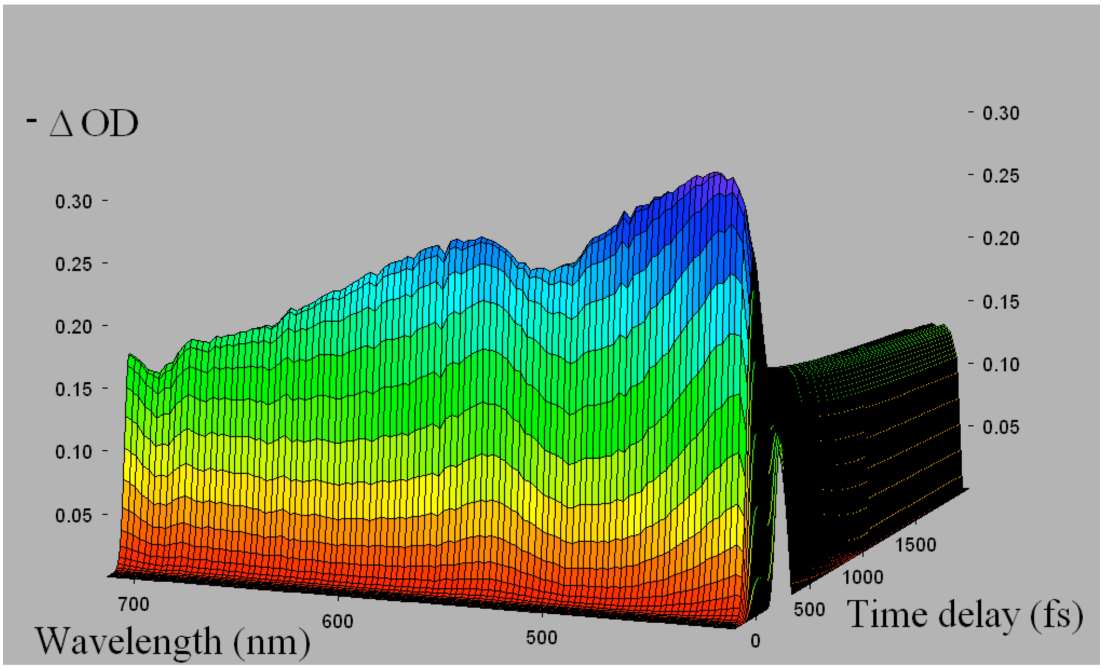

Fig. 7.4- *Three-dimensional surface plot reporting the change in the optical density induced by the excitation at ~400 nm with p ~ 4mW, after the subtraction of the periodic modulation.*

7.2 The Drude and Lorentz models

The classical theory of absorption in dielectrics is due to Lorentz [16] while for metals the Drude model is used [17]. Both models treat the optically “active” electrons as classical oscillators. In the Lorentz model the electron is considered to be bound to the nucleus by a harmonic restoring force. Drude instead considered the electrons free, and thus setting the restoring force zero. Both models include a damping term, representing the radiation losses, and the equation of motion of electrons results.

$$\frac{\partial^2 \vec{x}(t)}{\partial t^2} + \gamma \frac{\partial \vec{x}(t)}{\partial t} + \omega_0^2 \vec{x}(t) = \frac{e}{m} \vec{E}(t) \quad , \qquad 7.2$$

where e and m are the electron charge and mass respectively, $\bar{E}(t)$ is the driving electric field and γ is the viscosity parameter.

The solution of eq.7.2 is used to evaluate the dipole oscillator moment. The oscillations of the electrons in the system is related to the polarization of the medium, hence to the dielectric function, which can be written, in a simplified form, as

$$\varepsilon(\omega) = 1 + \chi(\omega) = 1 - \sum_j \frac{\Omega_j^2}{\omega^2 - \omega_j^2 + i\omega\gamma_j} \quad , \qquad 7.3$$

where χ is the linear susceptibility, and the j index spans over all the ionic species and Ωj is the number of electrons associated to the j-th ionic species

Fig.7.5 shows the real (ε_{1R}) and the imaginary part (ε_{2R}) of the dielectric function.

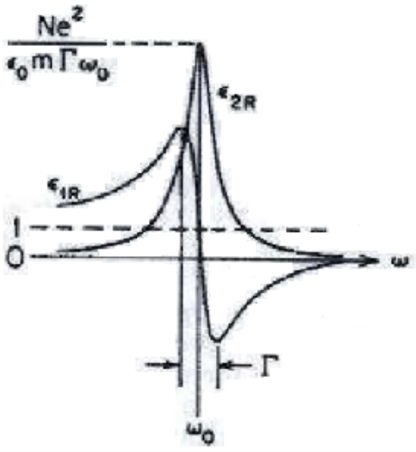

Fig. 7.5- *Frequency dependence of the real (ε_{1R}) and imaginary (ε_{2R}) part of the dielectric function.ω_0 is the transverse frequency, in the following indicated also with W_0. Γ is the line width, also indicated with γ of G. Finally, the maximum $\left(\frac{ne^2}{\Gamma\omega_0 m\varepsilon_0}\right)$ can be expressed as a function of the plasma frequency, the third parameter characterizing a Lorentz oscillator.*

In the figure N is the number of dipoles per unit volume, Γ is the damping constant (which appears in the motion equation as γ) and ε_0 is the free space permittivity.

In the Drude model ω_0 is set equal to zero, and the real and imaginary parts of the dielectric constant are then given by

$$\varepsilon_{!R} = 1 - (Ne^2\varepsilon_0 m)\frac{1}{\omega^2 + \gamma^2} \quad , \qquad 7.4\,(\,a\,)$$

$$\varepsilon_{2R} = (Ne^2\varepsilon_0 m)\frac{\gamma}{\omega(\omega^2 + \gamma^2)} \quad . \qquad 7.4\,(\,b\,)$$

Being γ related to the mean time between electron collisions with lattice vibrations.

According to the Drude model only the plasma frequency, equal to $\omega_p = \sqrt{\left(\frac{ne^2}{m\varepsilon_0}\right)}$, should dictate the macroscopic optical behaviour of a metal. However, it does not explain the colour of noble metals for example, in which the plasma frequency lies at about 9 eV. This value is outside the visible region, whereas, for instance the reflectance spectrum of silver shows a drop at 4 eV, that is below the expected plasma frequency.

This behaviour is due to the d-bands, which lie below the Fermi energy of the conduction band. Thus the transition from *d*-band (energy E_d) to empty states above the Fermi energy (E_f) can occur.

The reflectivity properties of noble metals are influenced by the combined effects of the free electrons (Drude model) and the bound d-electrons (Lorentz model).

If the two models are used in order to describe the measured variation of optical properties, as in a time-resolved experiments, the Drude model takes into account the time-dependent variation of the electron density $n(t)$ injected by the pump pulse in the empty band, instead the Lorentz model well describes the inter-band transitions.

The optical data acquired in pump-probe measurements on metallic systems are usually interpreted in the frame of the Drude model. Instead for semiconductors, as it has been proved by Glazer *et Al.* [13, 14, 15], the optical data can be described both in term of the Drude and Lorentz model, the choice of the model depending on the laser pump fluence.

7.3.1 The spectral analysis

In order to understand the physical origin of the spectral structure observed in the fast dynamic a fitting program [ReFIT], developed by Alexey Kuzmenko, is used [60].

This program allows the fitting a large variety of optical data, such as the absorption and trasmittivity coefficient and the reflectivity at grazing and normal incident angle. The fit is built starting from a Drude-Lorentz model, with a suitable number of oscillators which are completely defined by three parameters, namely the transverse frequency W_0 (or eigen-frequency), the plasma frequency W_p and the linewidth G (or scattering rate coefficient). From the modeling of the oscillators, it is then possible to calculate the associated dielectric function (real and imaginary part).

From the measured ΔOD data it is first necessary to calculate ΔT, inverting equation 6.1 *.

The signal acquired in the experiment is a variation of trasmittivity, and the program allows studying the change of the optical properties using a differential model.

If $S(\omega, P_1)$ and $S(\omega, P_2)$ are two different values of an optical property (in our case the trasmittivity), and $\mathrm{P_i}$ is the physical quantity whose change controls the value S (in our case the time delay between pump and probe). In principle, it is possible to obtain the model dielectric functions $\varepsilon_{mod}(\omega, P_1)$ and $\varepsilon_{mod}(\omega, P_2)$ by the fitting of $S(\omega, P_1)$ and $S(\omega, P_2)$, separately and assume that

$$\Delta\varepsilon(\omega) \approx \Delta\varepsilon_{\mathrm{mod}}(\omega) \equiv \varepsilon_{\mathrm{mod}}(\omega, P_1) - \varepsilon_{\mathrm{mod}}(\omega, P_2) \quad . \qquad 7.5$$

Here we have measured the variation of S (ΔS), and not the absolute value, so we have initially to construct a static model, that is then used to evaluate the derivatives of the measured static value of S with respect to ε_1 and ε_2

---

* *Since the program works in wavenumber (cm^{-1}), and not in wavelength (nm), all our data are converted in the former quantity.*

$$\alpha_1(\omega) \equiv \frac{\partial S(\omega)}{\partial \varepsilon_1(\omega)}, \ \alpha_2(\omega) \equiv \frac{\partial S(\omega)}{\partial \varepsilon_2(\omega)} \quad . \qquad 7.6$$

Using these derivatives, the differential spectra can be calculated in the first order of a Taylor expansion

$$\Delta S(\omega) \approx \alpha_1(\omega)\Delta\varepsilon_1(\omega) + \alpha_2(\omega)\Delta\varepsilon_2(\omega) \quad . \qquad 7.7$$

The second step of the fitting procedure requires then the introduction of an extra (differential) model and adjust its parameters to fit *ΔS*.

7.3.2 Spectral analysis: the static model

The first step is the construction of an opportune model which can describe the optical property of the sample in the unperturbed condition. This is done by fitting the absorption coefficient, measured by Pagliara et *al.* (19, 43) as shown in fig 7.6.

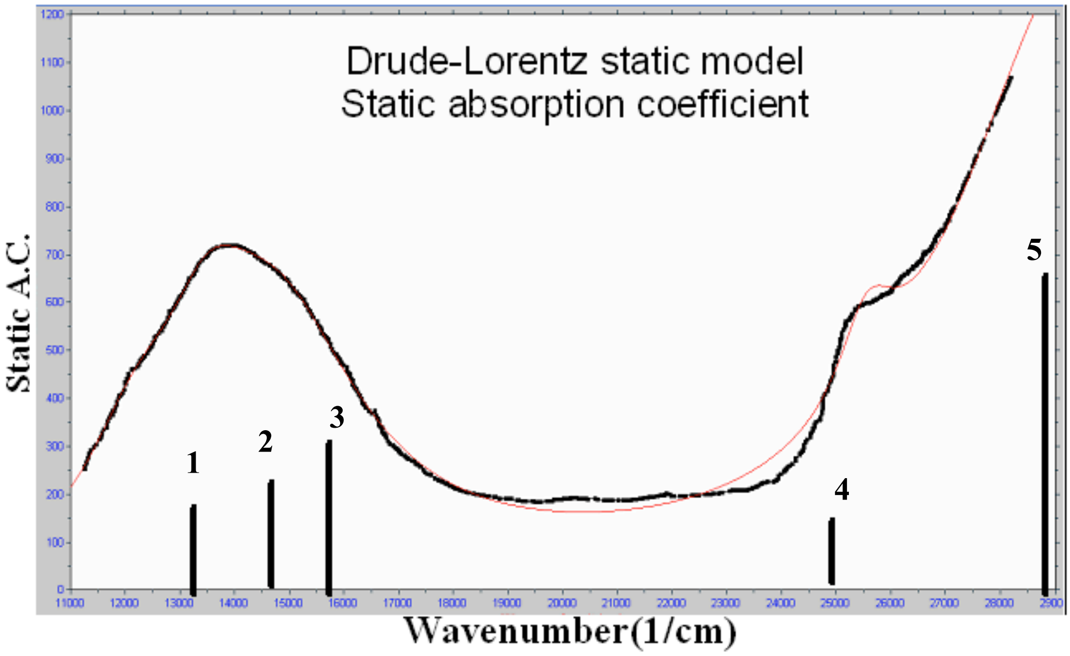

Fig. 7.6- Drude-Lorentz static model obtained by the fit of the absorption coefficient, taken in literature [19].

The best fitting of the data consists of five Lorentz oscillators, whose parameters are reported in the following table.

#	W_0 (cm^{-1})	W_p (cm^{-1})	G (cm^{-1})
1	12206	289.36	2388.3
2	13519	292.36	2024.7
3	14830	539.44	3737
4	25557	197.44	1274.5
5	29599	1092.3	5733

***Table 7.1-** Model parameters obtained for the static model, formed by five oscillators.*

7.3.3 Spectral analysis: the dynamic model

The second step is the fitting of the *ΔT* signal, with the differential model. In Figs.7.7 (a), (b) and (c) three different fits are reported, for the data acquired with the pump at 400 nm and power equal to 2 mW. The data are taken at three different delay times (-50 fs, 0 fs and 60 fs) in order to show the behaviour of the fits across the zero-delay time.

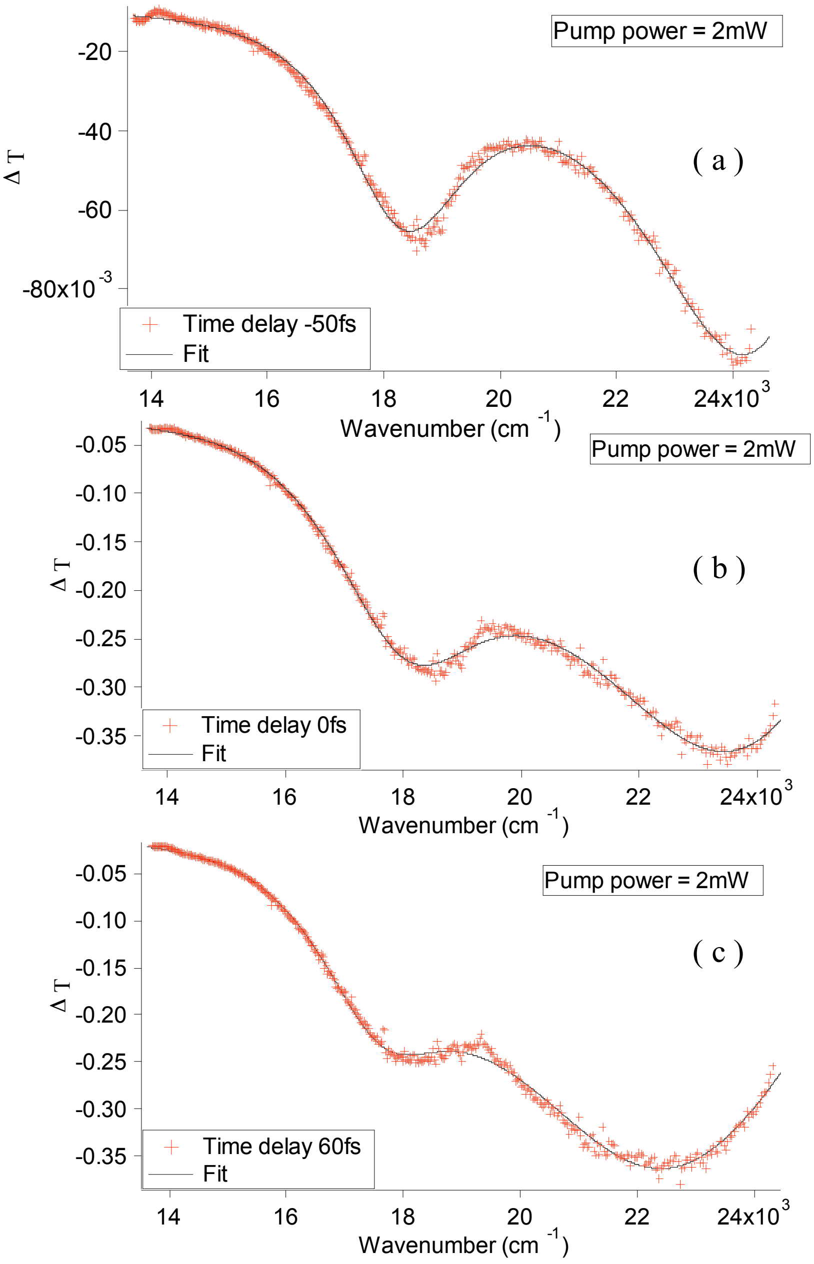

***Fig.** 7.7 **(a - c)-** Change in trasmittivity at-50 fs, 0 fs and 60 fs with associated fits, for the data set acquired with excitation at ~ 400 nm and p ~ 2 mW.*

Figs. 7.8 (a - f) show the comparison between the data and the fits for excitations at 400 nm and pump power of ~ 4 mW.

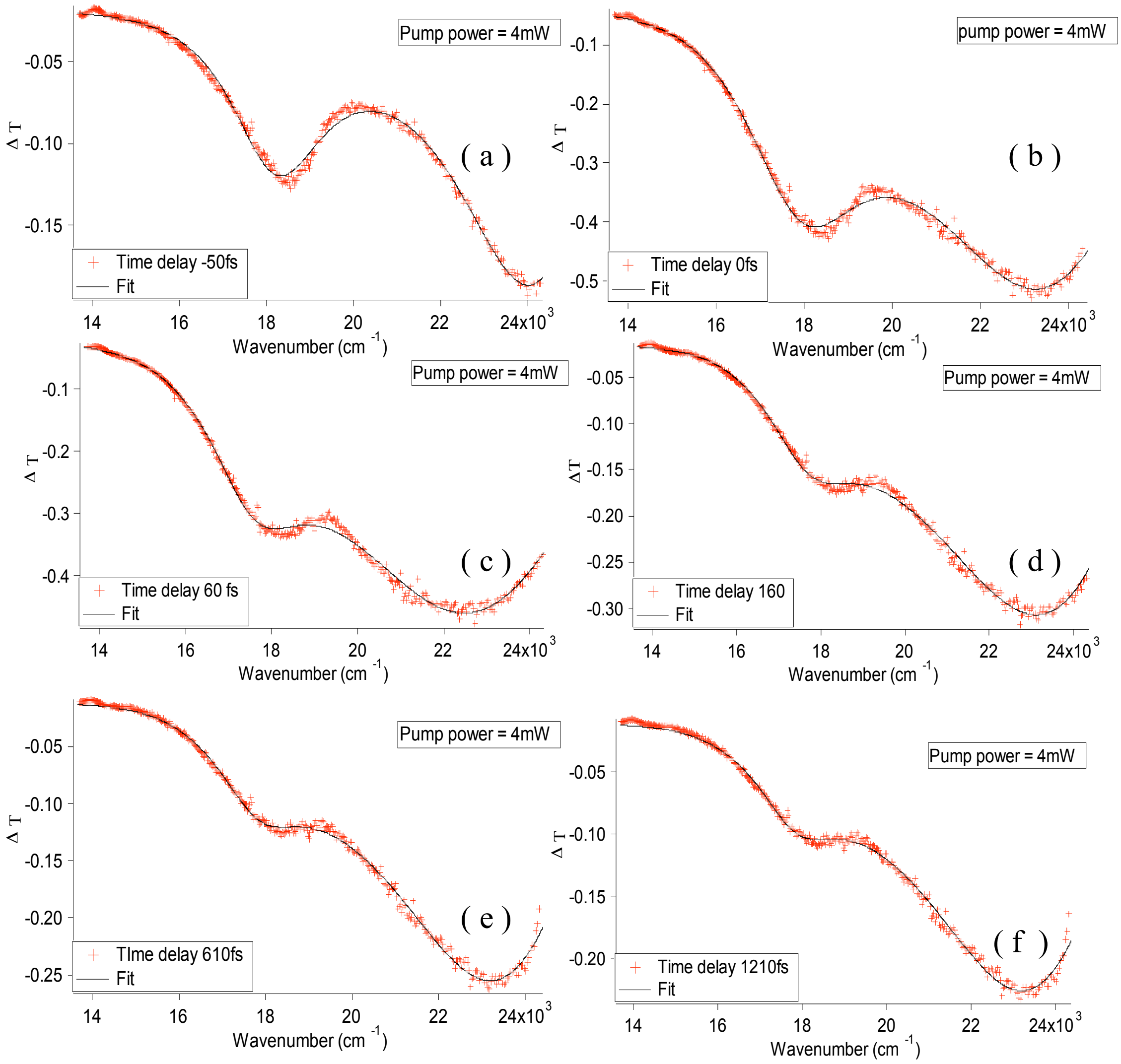

***Fig. 7.8 (a - f)** - Change in trasmittivity at -50 fs (a), 0 fs (b), 60 fs (c), 160 fs (d), 610 fs (e), 1210 fs (f) with associated fits, for the data set acquired with excitation at ~ 400 nm and p ~ 4 mW.*

Fig.7.8 (f) shows that, for the highest pump power, the signal is detectable up to 1 ps. In the data reported by Consani [58] a small signal is still detectable even after several hundreds of picosecond.

The differential model introduced to fit the change in trasmittivity is based on two Lorentz oscillators. As an example the parameters of the model, for a time delay of -50 fs and a pump power of 2 mW, are reported in the table 7.2.

#	W_0 (cm^{-1})	Wp (cm^{-1})	G (cm^{-1})
1	18306	119.2	2612.2
2	24622	229.45	4194

Table 7.2- *Model parameter for the dynamic model for the time delay equal to -50 fs for the excitation* at ~ 400 nm with p ~ 2mW.

The two oscillators correspond to the two bands previously described in Figs. 6.6 (a) and 6.6 (b).

Figs. 7.6 and 7.8 show that the fit has a good accordance with the experimental data in the region from 14000 cm^{-1} up to the minimum of the first band a ~ 18000 cm^{-1}. The model fits well also the data associated to the second band, in the range between ~21000 cm^{-1} up to the end of the acquisition range. Only in the central region, between the two oscillators, the fit gets worse, and the difference is stronger when the ΔT signal becomes larger (at the zero time delay, and with the higher pump power). The same is true also for the other pump power (0.5 mW and 0.2 mW), and for the data acquired using the pump at 800 nm.

The fitting is done for all the time delay between about -100 fs and 500 fs, in order to follow the evolution of the model parameters as a function of the time delay.

7.3.4 Spectral analysis: time dependent dielectric function

The last step of the spectral analysis is the calculation of the differential dielectric function, starting from the differential model. From the latter the contribution of a single oscillator to the dielectric function is calculated. Figs.7.9 (a-b) report the imaginary and real part respectively of the dielectric function for the first oscillator. Figs. 7.10 (a-b) report similar data for the second oscillator. For both the fitting of the data has been obtained with the pump at 400 nm and power at 4 mW.

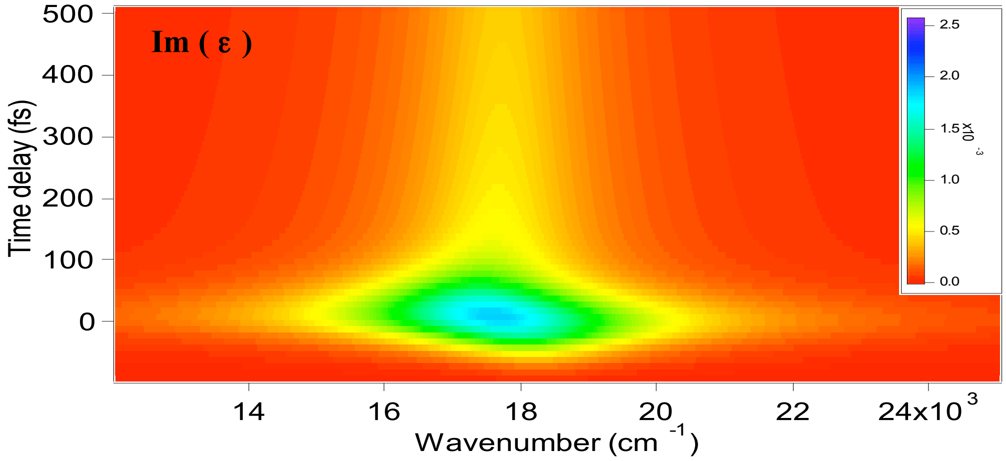

Fig. 7.9 (a)- Imaginary part of the first-oscillator-contribution to the time-dependent dielectric function, calculated for the data acquired with excitation at ~ 400 nm with p ~ 4 mW. The intensity is reported in a colour scale, as a function of the wavenumber and of the time-delay.

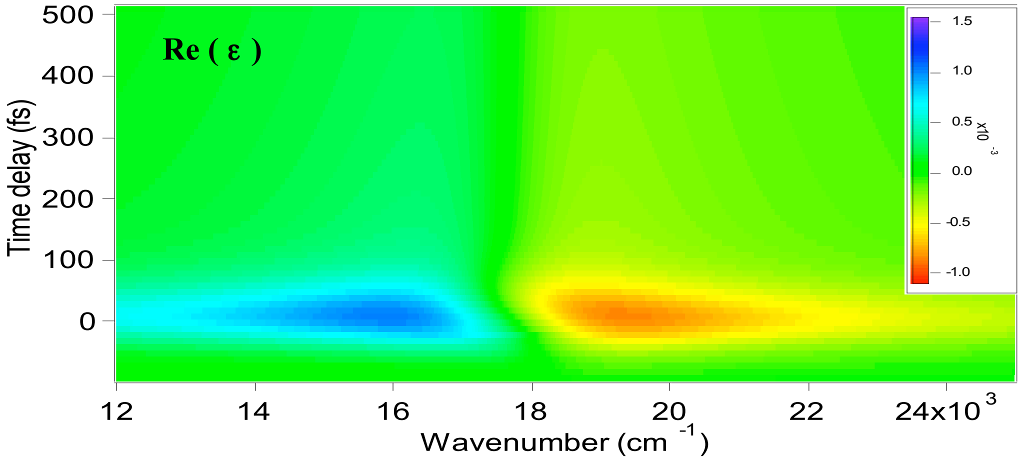

Fig. 7.9 (b)- Real part of the time-dependent dielectric function.

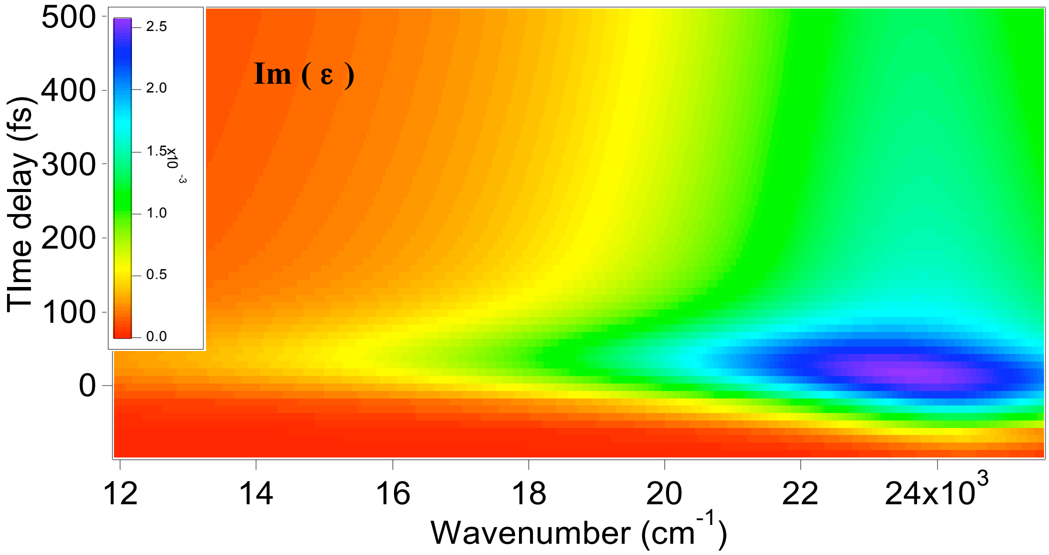

Fig. 7.10 (a)- Imaginary part of the second-oscillator-contribution to the time-dependent dielectric function, calculated for the data acquired with excitation at ~ 400 nm with p ~ 4mW. The intensity is reported in a colour scale, as a function of the wavenumber and of the time-delay.

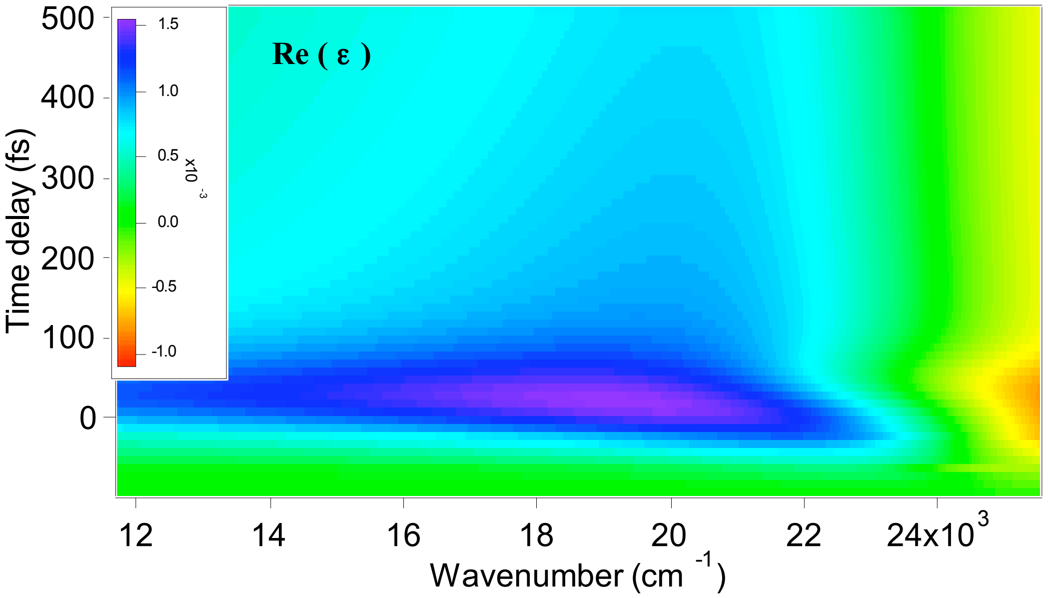

Fig. 7.10 (b)- *Real part of the dielectric function due to the contribution of the second oscillator.*

It is worth to note that for both the oscillators, a very fast change of the dielectric function is detected. The imaginary part rises up in a time smaller than 100 fs with a relaxation process characterized by two different time scale processes. One lasts for ~ 100 fs, the other has a slower decay-time.

It is interesting to notice that in about 200 fs the strong spectral modulation ends, and the following dynamic is less structured, as it is possible to see also in the raw data presented in Fig.6.3 (a).

In the fast dynamic it is present, besides the intensity change of the dielectric function, also a spectral change of the maximum of the *Im(ε)*.

In Fig. 7.11 the data of Fig 7.9 (a), are plot as a sequence of spectra stack along the vertical axis and separated by a constant offset.

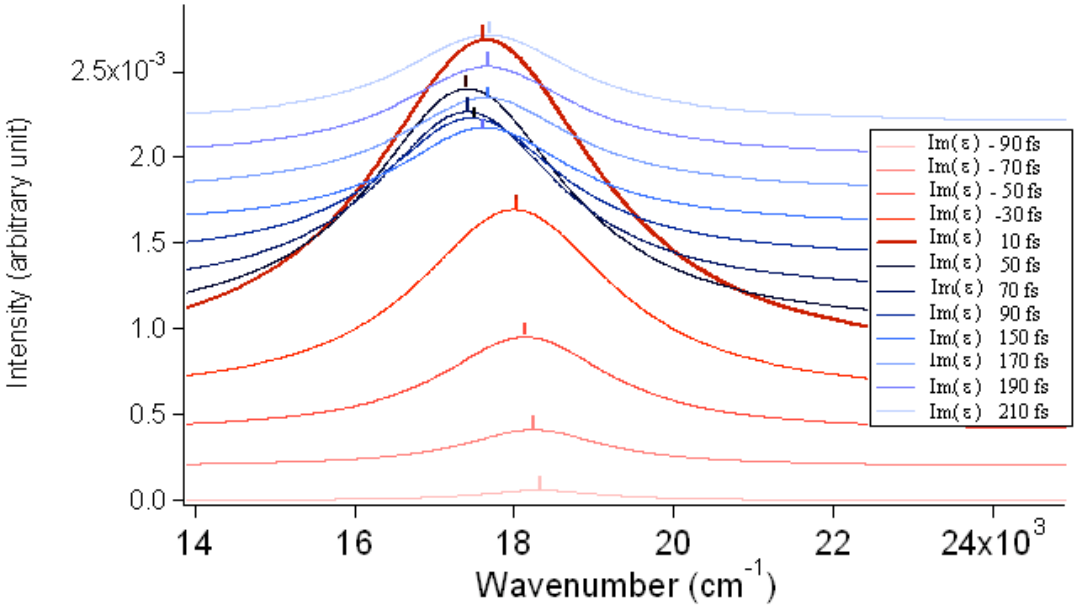

Fig. 7.11- *different spectra reporting the contribution to the imaginary part of the differential dielectric function due to the first oscillator (at ~ 2.2 eV). The spectrum for the different time-delays stacks along the vertical axis and a constant spacing is introduced between them. A mark labels the maximum- position for the different time-delays.*

The color of the graph is pink for the delay time - 90 fs, then it gets darker as the time delay gets closer to 10 fs, where the maximum is found. The following positive delay time is dark blue and it gets lighter as the time-delay increases. The vertical marker indicates the position of the maximum for every time delay.

The same has been done for the imaginary part of the dielectric function associated to the second oscillator, as reported in figure 7.12.

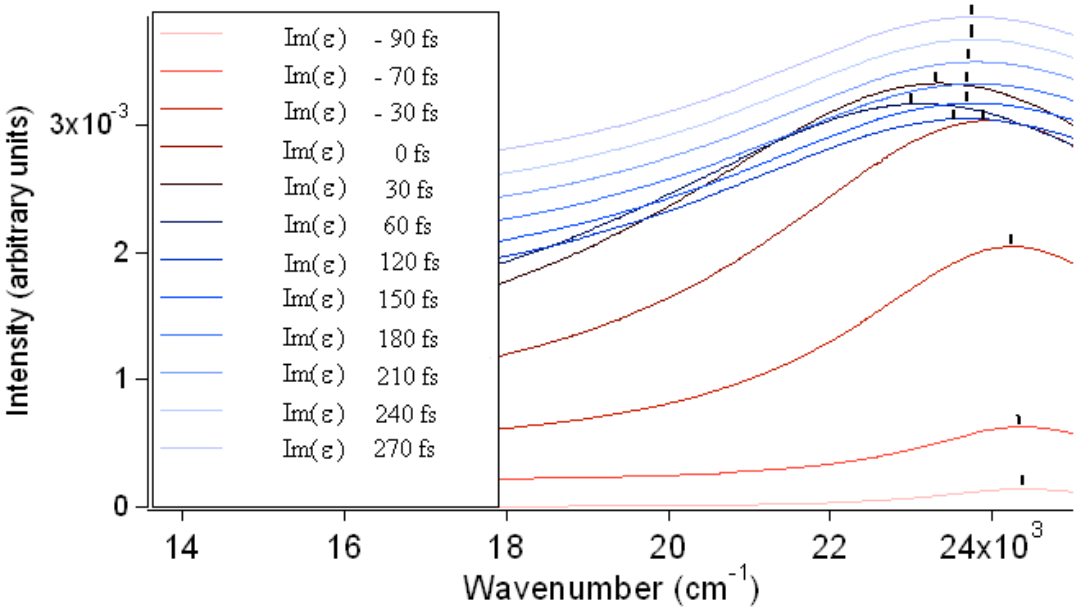

Fig. 7.12- *Imaginary part of the differential dielectric function for different time-delays for the second oscillator (at ~ 2.9 eV). The spectra stack along the vertical axis with a constant spacing between them, and a mark labels the maximum-position.*

Also for this set of data it is possible to observe both a fast increase of the maximum and a translation of the maximum position towards lower wavenumber. After the zero time a slower relaxation of the maximum position towards the initial value can be observed.

7.4 Comparison of the model parameters

Since the maximum of the imaginary part is determined by the value of W_0 it is possible to study its time dependence. Figs.7.13 (a - b) report the maxima position versus the time-delays foth the two oscillators, with the pump at 400 nm, and power of 0.2 mW, 0.5 mW, 2 mW and 4 mW.

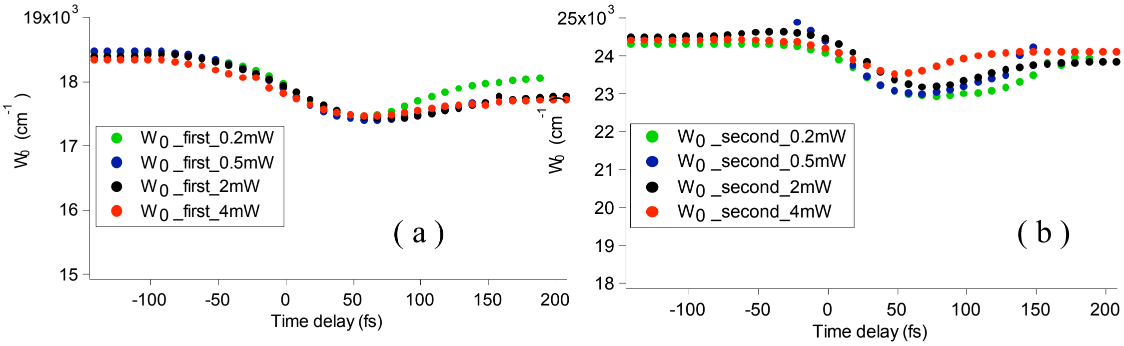

Fig. 7.13 (a, b)- Time-dependent behaviour of the model parameter ω_0 (W_0) for the different pump power, for the first oscillator (on the left) and for the second oscillator (on the right).

The change in the position of the maximum seems to not depend on the power of the pump. In fact, it changes in time for both the two oscillators for all the four pump powers considered.

In Fig. 7.14 (a-d) the other two parameters of the model, *G* and *W_p*, are reported, for the two oscillators.

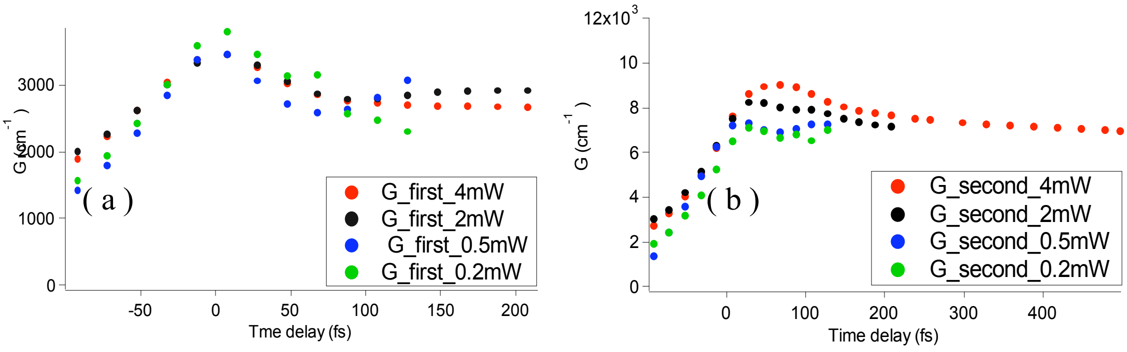

Fig. 7.14 (a, b)- Behaviour of the G model parameter as a function of the time-delay for the four different pump power, for the first oscillator (on the left) and for the second oscillator (on the right).

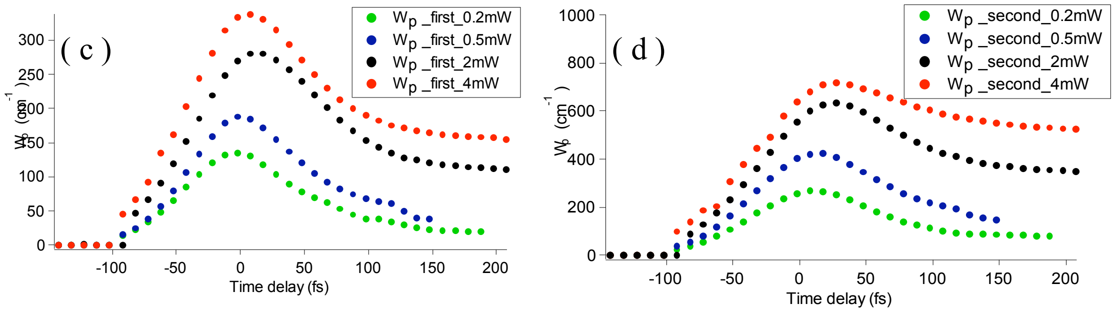

***Fig. 7.14 (c, d)-** Behaviour of the W_p model parameter as a function of the time delay for the four excitation power (excitation at ~ 400 nm) for the first oscillator(on the left) and for the second oscillator (on the right).*

While the eigen-frequency of the two oscillators seems not to depend on the pump power, the plasma frequency shows a strong power dependence.

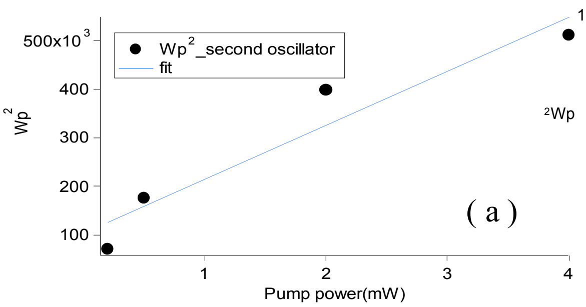

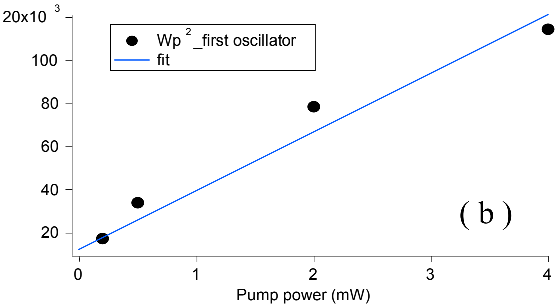

***Fig. 7.15 (a)-** Trend of the Wp^2 parameter of the second oscillator as a function of the pump power.*

***Fig. 7.15 (b)**- Trend of the Wp^2 parameter of the first oscillator as a function of the pump power.*

Fig. 7.15 reports the values of Wp^2 vs. the pump power, for the two oscillators. Having only four distinct points a correct estimation of the behaviour of Wp^2 as a function of the pump power is not possible. From the time dependence of Wp^2 on the pump power, and from relation $W_p = \sqrt{\left(\frac{ne^2}{m\varepsilon_0}\right)}$, it is possible to speculate that, for the present excitation regime, the electron densities varies linearly with the pump power.

7.5 Pump excitation at 800 nm

The same analysis has been performed for the excitation at 800 nm.

In this case it is possible to fit the time traces by convoluting three exponential decays function a Gaussian function and a step function. Fig. 7.16 reports the residual matrices, showing the same modulation already detected for the previous data.

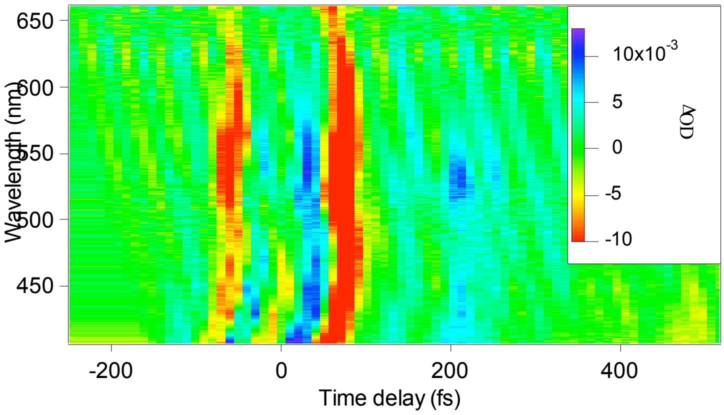

Fig. 7.16- *Matrices formed by the fit residuals, reported as a function of the time-delay and wavelength. The data acquired with excitation equal to ~ 800 nm and p ~ 6.8 mW are shown in an image plot, with intensity expressed by the colour scale.*

The presence of modulation is smaller at 800 nm than for the excitation at 400 nm, both with a power of 4 mW. This is also the case for a 800 nm pump at 6.8 mW, even if in these conditions the density of adsorbed energy is 1.79 times the density of adsorbed energy at 400 nm at 4 mW (see table 6.1).

By the subtraction of this modulation from the raw data the 3D surface reported in Fig 7.17 is obtained.

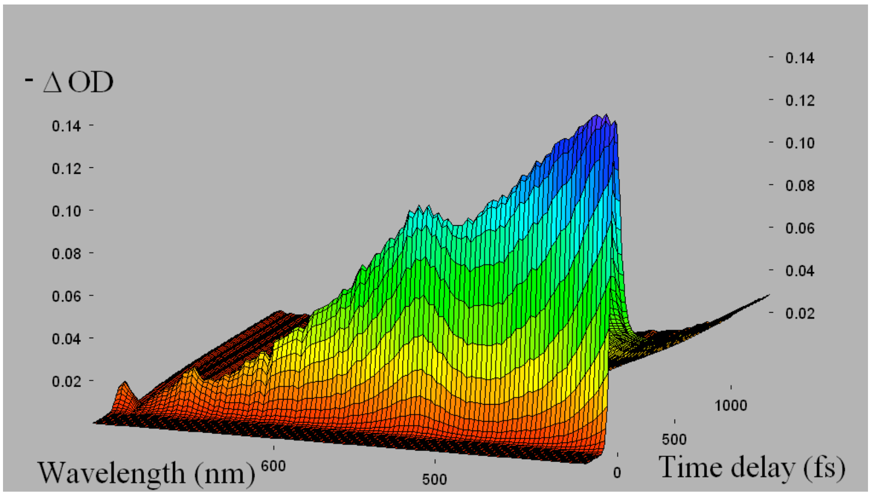

Fig 7.17- *Three-dimensional surface plot reporting the change in the optical density induced by the excitation at ~800 nm with p ~ 6.8mW, after the subtraction of the periodic modulation.*

Also these data are then analyzed by using ReFIT program. Fig 7.18 (a) and Fig. 7.18 (b) report the imaginary part of the two oscillators.

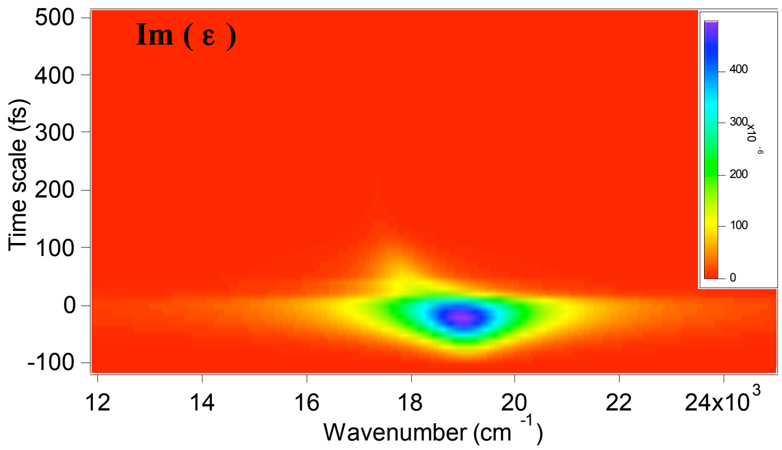

Fig. 7.18 (a)- *Imaginary part of the first-oscillator- contribution to the time-dependent dielectric function, calculated for the data acquired with excitation at ~ 800 nm with p ~ 6.8 mW.*

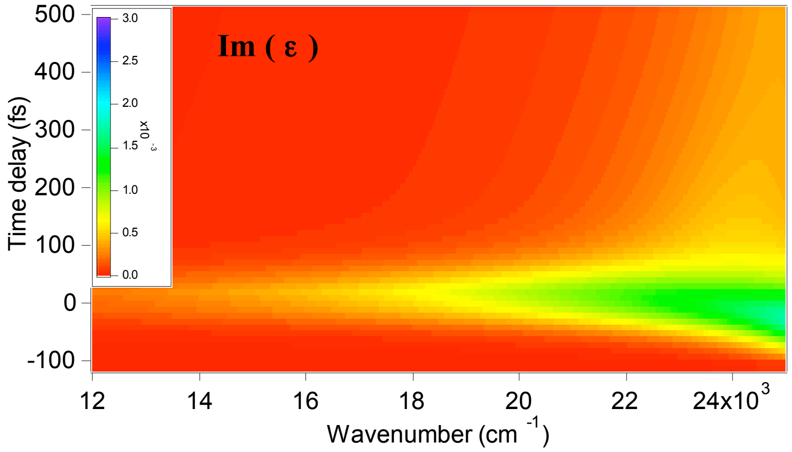

Fig. 7.18 (b)- *Imaginary part of the second-oscillator- contribution to the time-dependent dielectric function, calculated for the data acquired with excitation at ~800 nm with p ~ 6.8 mW.*

By comparing the given components of the dielectric function at 800 nm to those at 400 nm it is possible to notice some similarities and important differences.

There are always two main bands rising in less than 100 fs. The spectral behaviour are fitted using a differential model with two oscillators. The first has an energy (wavenumber) position close to the energy of the first oscillator excitated at 400 nm. This band lasts for a time of the order of 200 fs, whereas the second oscillator seems to be out of the experimental range, as shown in Fig. 6.17 (b).

This different behaviour, especially in the delay time near the zero time, is better described by Fig.7.19 (a).

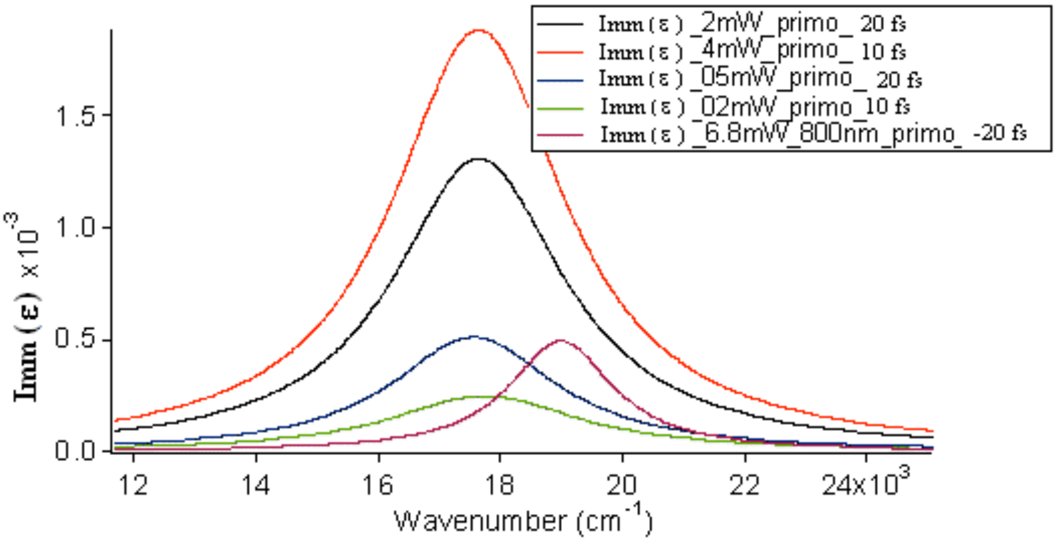

Fig. 7.19 (a)- *Imaginary part of the dielectric function for the first oscillator at the zero time-delay for the different excitations.*

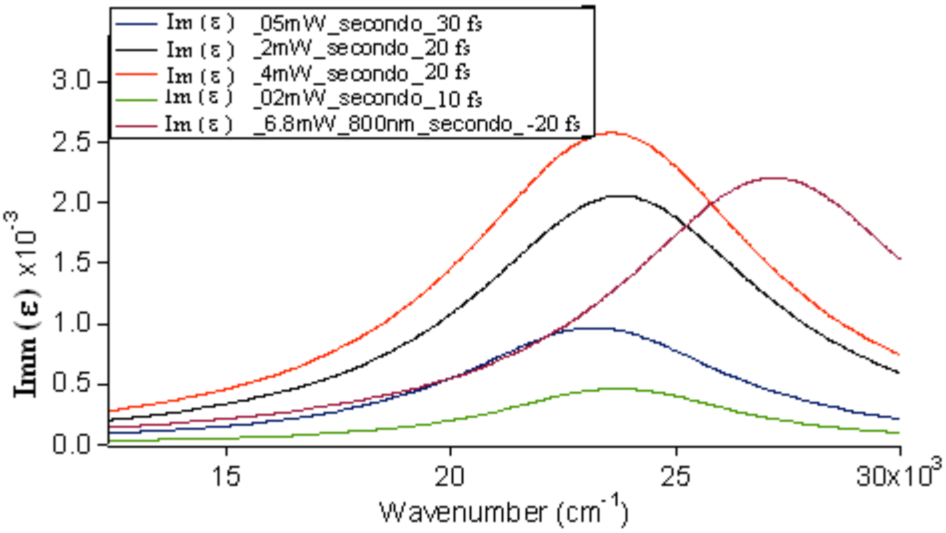

Fig. 7.19 (b)- *Imaginary part of the dielectric function for the second oscillator at the zero time-delay for the different excitations.*

Fig. 7.19 (a) reports the imaginary parts of the dielectric function associated to the first oscillator, for the time delay of maximum intensity. Fig 7.19 (b) reports the same function for the second oscillator.

Fig. 7.19 (a) and Fig. 7.19 (b) show the different character of the two perturbations. The first oscillator has a different W_0 with respect to the oscillator at 400 nm. Also the intensity of the peaks is smaller, in spite of the fact that at 800 nm and 6.8 mW of power, the density of the absorbed energy is 1.79 times higher at 400 nm with 4 mW of power.

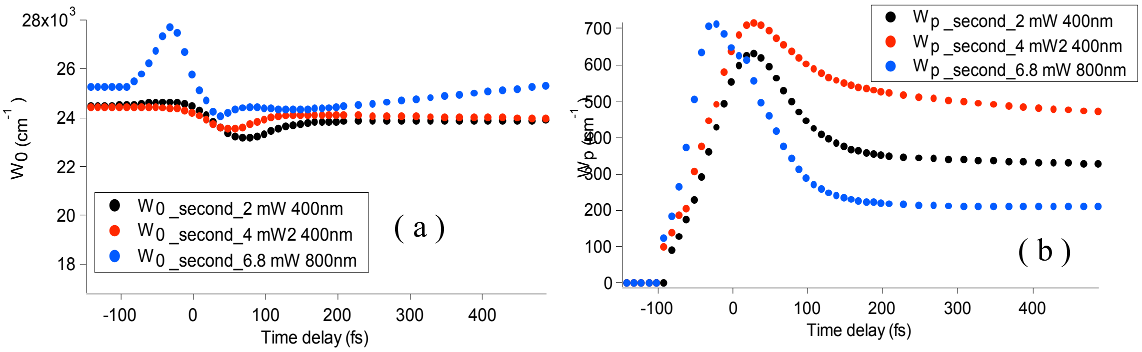

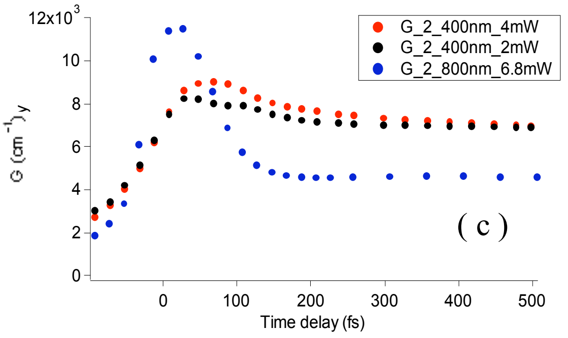

Fig. 7.20 (a - c) - *Model parameter (W_0 in* ***a****, W_p in* ***b*** *and G in* ***c****) comparison for the data obtained at ~ 800 nm with p ~ 6.8mW and at ~400nm with p ~ 4mW and ~ 2mW. The parameters describe the second oscillator for different time delays between ~ -100 fs and ~500 fs.*

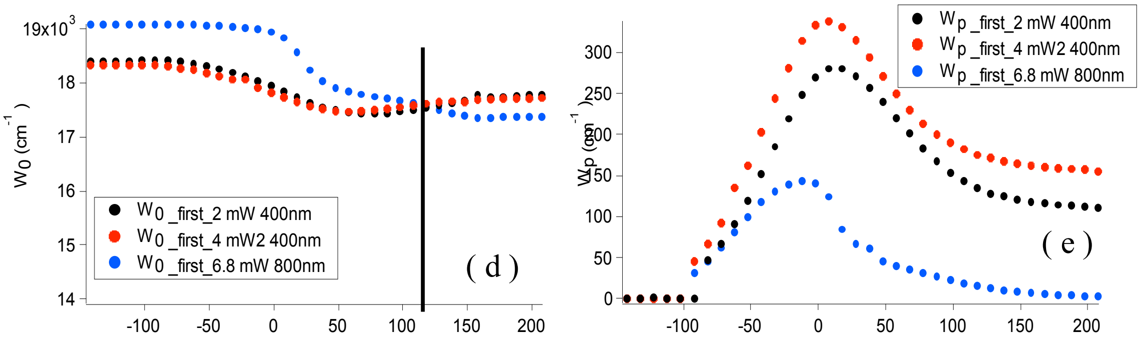

*Fig. 7.20 (d - f) - Model parameter comparison (W_o in **d**, W_p in **e** and G in **f**) for the data obtained at ~800 nm with p~6. 8mW and at ~400 nm with p ~ 4 mW and ~ 2 mW. The parameters describe the first oscillator for different time delays between ~ -100 fs and ~220 fs.*

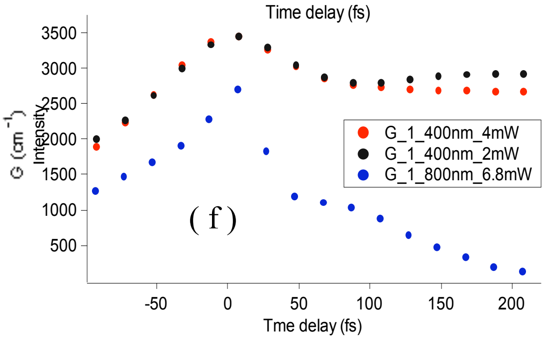

Even if the position of the maximum for the second oscillator is out of the investigated range it is interesting to point out the difference between the excitations at 800 nm and 400 nm.

Fig. 7.19 (a-b) report, as an example, only one delay time, however Fig. 7.20 (a–f) report the model parameters, for time delays between 210 fs and -110 fs for the first oscillator, and between 500 fs and -110 fs for the second oscillator.

From these figures it is quite clear that the effects of the two perturbations are significantly different. For example, the value of W_p for the first oscillator reaches quickly the zero, while for the excitation at 400 nm it remains above zero for a long time, even if the density of the absorbed energy is much higher for the excitation at 800 nm. Besides, at negative time delay, the maximum position is found at higher wavenumber for the excitation at 800 nm. Nonetheless, as W_p approaches zero, W_0 moves towards smaller wavenumber crossing the 400nm W_0 function for a delay time of ~110 fs.

For the second oscillator is evident that the fast dynamics is significantly different for the two excitations. W_0 , W_p and G have a larger and rapid increase at the zero-time delay, with a characteristic time comparable with time structure of the laser pulse. After this strong perturbation W_p decreases to a value smaller than the ones reported for the excitation at 400 nm (with power equal to 2 mW and 4 mW). W_0 after the fast dynamics increases and becomes different from the W_0 at 400 nm.

8. Discussions

8.1 The coherent phonon

The first interesting feature of the data shown previously is the temporal modulation of the *ΔOD* signal. This effect can be associated with the generation of a coherent phonon.

As well known a thermal excitation induces lattice oscillations with random phases, whereas a coherent light pulse, shorter than the inverse of a fundamental phonon frequency, could produce simultaneous excitations of in-phase phonons (coherent processes).

The coherent phonons are associated with a macroscopic change in the dielectric function and, as a consequence, in the optical properties. These modifications last until dephasing processes destroy the coherence of the oscillations.

In our experiment the coherent oscillation has a period of the order of ~ 100 fs.

In table 8.1 the phonon modes, measured by Popovic *et al.* [44], are reported, along with a Raman active mode with a period of ~100 fs. This is an A_g fully symmetric mode, which originates from oxygen ions displacements that tend to rotate the CuO_4 plaquette, as shown in Fig. 8.1.

	Modes	Energy (meV)	Energy (cm^{-1})	Period (fs)
Raman active modes	A$_g$	23.1 41.3 73.8 106	187 332 594 859	178 100 56 39
	B$_{1g}$	48	388	86
	B$_{2g}$	14.4 27.7 53 109	116 224 427 879	287 149 78 38
	B$_{3g}$	13.6 51 88.3	110 411 712	303 81 46.8
Infrared active modes	B$_{1u}$	16.3-16.6 40.5-46.1 59.3-60.6 76.2-79.5 105-109	131-134 328-372 478-489 615-640 843-880	253-249 102-89.6 69.7-68.2 54.2-52 39.5-38
	B$_{2u}$	20.5-20.9 65.6-74.3 89.2-99.6	165-168 530-600 720-803	202-198 63-55.6 46.3-41.5
	B$_{3u}$	59.5-60.8 26.2-28.7 35.3-38.3 46.7-51.3 95.7-106	48-49 211-231 285-308 377-414 772-857	694-680 158-144 117-108 88.4-80.5 43.2-39

Table 8.1- *Table of* $CuGeO_3$ *measured phonons with respective periods [44]. For each IR active phonon two values are given, that refer to the transversal optical (TO) and longitudinal optical (LO) modes respectively.*

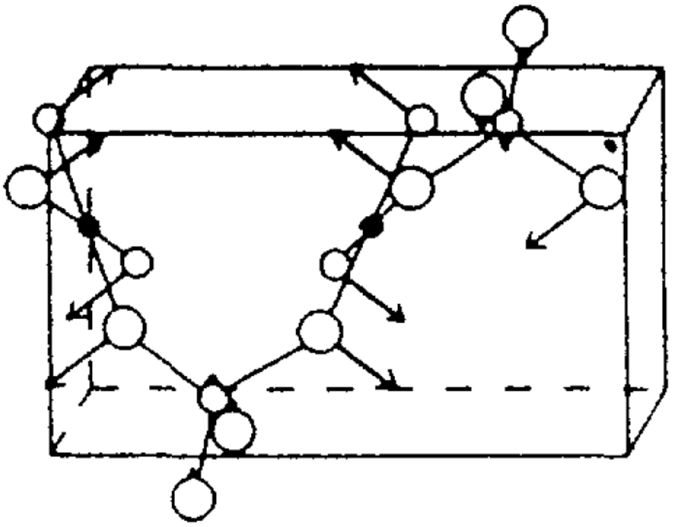

Fig. 8.1- *Normal mode displacement of the* $CuGeO_3$ A_g *phonon with period equal to 100 fs. The displacement consists in the vibration of the* O_2 *oxygen atoms which tend to rotate the* CuO_4 *square plaquette [44].*

Theoretical works in the literature introduced an important distinction between impulsive and resonant types of excitation [62, 63].

The first theoretical description of the coherent phonon generation is the impulsive stimulated Raman scattering (ISRS) [61]. An ultra short laser pulses exert an impulsive driving force on the sample. That gives momentum to the ions, changing their kinetic energy.

However, Zeiger *et al.* introduced a different mechanism known as displacive excitation of coherent phonons (DECP) [62]. In this model, upon an ultra-fast optical excitation a significant fraction of the valence electrons is excited to higher energy electronic states. Such an excitation reduces the attractive part of the inter-atomic potential and allows the ions to move with their intrinsic velocities towards a new equilibrium position.

In contrast to the ISRS excitation mechanism, DECP consists of an instantaneous change in the potential energy of the ions.

In 2002 Merlin *et al.* [63] described the Raman scattering with two separate tensors, having the same real components, associated with the impulsive generation of phonons, but different imaginary parts. If the imaginary term dominates, the mechanism for two processes is displacive. Therefore, the DECP model represents only a particular case of the more general ISRS mechanism.

Following the DECP model, the excitation of the coherent phonon is due to an inter-band excitation from a bonding orbital to an anti-bonding orbital [62]. The presence of this inter-band excitation is extremely important also in order to understand the rising of two bands in the spectral domain observed in the present experiment.

The coherent phonon itself, and the induced ionic displacements, are also interpreted as key effects affecting the appearance of the first band (at 520-530 nm).

8.2 The first oscillator and the phonon assisted d-d transitions

By comparing the energy position of the first band (at ~ 2.2 eV) with the data found in literature for the *d-d* transitions it is not possible to associate this peak in the *ΔOD* signal to any static *d-d* transitions.

A tentative phenomenological model to explain this observation is given in the following.

After the arrival of the pump pulse, the $CuGeO_3$ is strongly perturbed, and the presence of a coherent phonon is the finger print of this perturbation that also involves some inter-band transitions. The lower inter-band excitation consists in the transfer of an electron from an oxygen ion to a copper ion. This charge transfer is possible since the pump energy is near to the CT excitation energy. By transferring a hole into a plaquette oxygen ion (plaquette1 in Fig. 8.2), a change of the local field felt by the copper ion of the near plaquette (for example plaquette 2) should be excpected.

Since the Cu atom has gained the electronic charge, it changes its electronic configuration from d^9 to (d^{10}, $\underline{L}$) and no further *d-d* transitions are possible on this site. However, this simplified picture must be modified considering that the transferred electron charge is delocalized on the neighbouring CuO_4 plaquettes [53, 65]. The change of the charge distribution, even if limited to few neighbouring CuO_4 units modifies the local crystal field, which in turns changes the equilibrium position of the oxygens ions forming the plaquette.

Broer and Coen de Graf analyzed, through *ab-initio* calculation in a cluster model, the change in the d-d transitions energy as a function of the copper ion coordination and as a function of the Cu-ligand distances [53].

Their work can be divided in two parts. First they started studying a model system (CuO), with an ideal rock-salt structure, and simple cubic symmetry. Then they elongated the Cu-O$_{\mathrm{apycal}}$ distance in order to study the dependence of the *d-d* transition energies on the ratio between the Cu-O$_{\mathrm{plaquette}}$ and Cu-O$_{\mathrm{apycal}}$ distances. In the following the in-plane/apex ratio will be indicated with *r*.

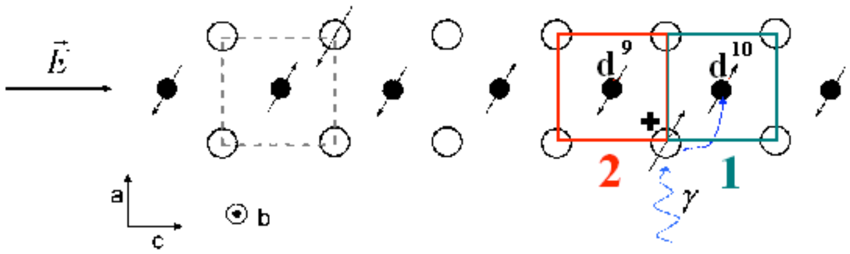

Fig. 8.2- *Cluster of CuO_4 square plaquette, showing the laser induced (γ) CT from an oxygen atom to a Cu ion, whose electronic configuration change from d^9 to (L, d^{10}).*

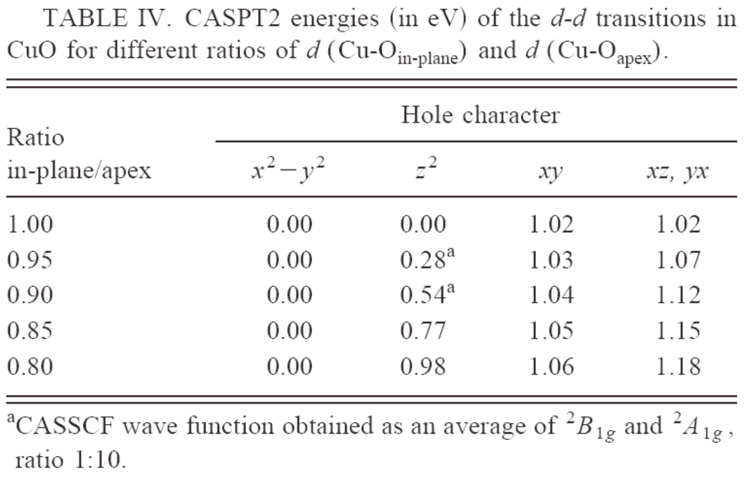

TABLE IV. CASPT2 energies (in eV) of the *d-d* transitions in CuO for different ratios of d (Cu-O$_{\text{in-plane}}$) and d (Cu-O$_{\text{apex}}$).

Ratio in-plane/apex	Hole character			
	x^2-y^2	z^2	xy	$xz,\ yx$
1.00	0.00	0.00	1.02	1.02
0.95	0.00	0.28[a]	1.03	1.07
0.90	0.00	0.54[a]	1.04	1.12
0.85	0.00	0.77	1.05	1.15
0.80	0.00	0.98	1.06	1.18

[a]CASSCF wave function obtained as an average of $^2B_{1g}$ and $^2A_{1g}$, ratio 1:10.

Table 8.2- *CASPT2(complete active space second-order perturbation theory) energy (eV) of the d-d transitions in Cu-O for different ratios of d(Cu-O$_{\text{in-plane}}$) and d(Cu-O$_{\text{apex}}$) [53].*

The results obtained from the cluster calculation are reported in table 8.2. The transition from the lower energy state ($d_{x^2-y^2}$) towards the d_{xy} state is not affected by the change in the Cu-O$_{\mathrm{apycal}}$ distance, while the energy positions of the d_{xz} and d_{yz} states are only slightly changed by the different value of *r*.

At the same time it is sufficient a change of the order of the 20% in the value of *r* to change the energy position of the d_{z^2} state from 0 eV to 1 eV.

After having shown the strong dependence of the energy position for the d_z^2 orbital as a function of r, the authors calculated the d-d energy transitions for different cuprates.

Therefore, the ideal model for a Cu-O cluster is changed into much more realistic models, taking into account the specific crystalline structure of the different cuprates.

The result is that the d-d transitions from $d_{x^2-y^2}$ towards the d_z^2 orbital has a characteristic energy which varies from 1 eV in La_2CuO_4 to 1.7 eV in $CuGeO_3$ to more than 2 eV in Ca_2CuO_3 (2.15 eV) and Sr_2CuO_3 (2.11 eV).

The r values for these compounds are 0.8 for La_2CuO_4, 0.7 for $CuGeO_3$, 0.6 for Ca_2CuO_3 and 0.56 for Sr_2CuO_3.

These simulations suggest the possibility of interpreting the first band, at about 2.2 eV, as a d-d transition from $d_{x^2-y^2}$ towards the d_z^2 [53].

This energy is different from the 1.7 eV static value because of the change in the charge density around the plaquette oxygen ions, which is connected to the change of the in-plane/apex ratio.

This interpretation is reinforced by the fact that the energy position of W_0, reported in Fig. 7.13 (a), does not show any significative variation for the different pump powers. The transfer of the d-d transition energy from 1.7 eV, to 2.2 eV depends only on the change in the electron density and on the local field felt by the copper ions. The change in the pump power affects only the number of plaquettes where the CT is realized, and it controls the number of copper ions that feel a perturbed local field. Only the parameter W_P, the strength of the oscillator, displays pump power dependence, as shown in Fig. 7.15 (a).

In the time evolution of the first band it is clearly visible a very fast optical response, that can be associated to the CT process. The change in the charge distribution modifies the local field and so the energy position of the d-d transitions.

As discussed also in the study of organic compounds, such as ($(EDO\text{-}TTF)_2PF_6$) [38], after the photo-excitation there is a quick ground-state-recovery, followed by a vibrational cooling of this hot ground state, on a pico-second time scale. A lot of energy is transferred in a limited number of coherent phonon modes, whose vibration drastically distorts the crystalline structure, leaving the sample in a meta-stable structural configuration.

We can speculate that a similar effect characterizes also $CuGeO_3$. The change in the charge distribution inside the plaquette lowers the electronic screening of the inter-atomic potential. Following the DECP model a coherent phonon is excited in the system, and it permits the creation of a meta-stable structural configuration.

Therefore, also the in-plane/apex ratio is affected by the coherent phonon, shown in Fig. 8.1, where the vibration involves a rotation of the plaquette plane [44]. The new meta-stable configuration probably enhances the distortion of the octahedron, as shown in Fig. 8.3, contributing to the change in the energy splitting of the *d*-bands.

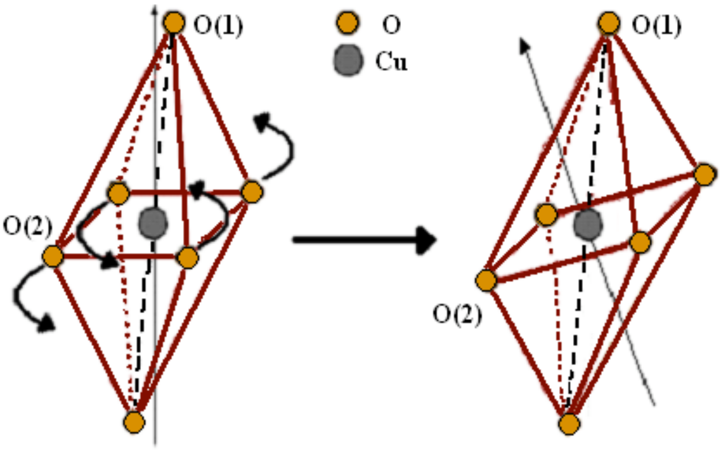

Fig. 8.3- *Elongated octahedron whose distortion is enhanced by the coherent phonon*

It is possible to investigate also the presence of the first band in the data acquired with the pump excitation at 800 nm. With this kind of excitation it is not possible to excite electrons from oxygen atoms to copper ions, but the electrons are re-arranged on the copper ion.

After the pump pulse at 800 nm a hole is transferred from the d_{Z^2} to an orbital lying on the plaquette. As already discussed the variation of the electronic density distribution can be associated with an equivalent change in the Cu-O bond length. This process will also induce a charge re-distribution that can influence the neighbouring plaquettes.

The excitation at 800 nm introduces not only a hole in the plaquette plane orbitals, but it also eliminates the hole present along the z direction, so the change in the local field felt by the copper ion results even stronger for this excitation than for the one at 400 nm.

This can explain why W_0 of the models for the excitation at 800 nm is different from the values obtained for the excitation at 400 nm.

The perturbation induced by the excitation at 400 nm is delocalized in the near plaquettes and different copper ions are affected by the change in the local field. Instead with the excitation at 800 nm only a single copper ion felt the change induced by the re-arrangement of the electronic charge. This speculation offers a possible explanation for the smaller value of W_P of the oscillator, as it is shown in Fig 7.20(e). Also for the excitation at 800 nm the lowering of the electronic screening of the inter-atomic potential gives rise to a coherent phonon response with a change in the structural configuration that lasts on the pico-second time scale.

8.3 The second oscillator, the delocalized photo-excited holes and the probing of the CT to an excited state

The second spectral feature consists in an increase of the *ΔOD* on a time scale comparable with the time-duration of the laser pulse. This increase is followed by a relaxation on a time scale of 150-200 fs. After the first decay, with a characteristic time typical of an electronic process, there is a slower decay in the ps → ns time domain. This effect can be related to the relaxation of the system from a structural deformation. As already noticed for the first oscillator the model parameter W_0 doesn't display pump power dependence, while W_P does. In addition W_0 is characterized by the same temporal behaviour for the two bands, i.e. a fast decrease (~150 fs), from 2.27 eV to 2.16 eV for the first band, and from 3.02 eV to 2.94 eV for the second band. On a longer time-scale W_0 recovers a value of 2.2 eV and 2.97 eV.

All these common features suggest that the two bands are directly related to the same process. By comparing the energy position of W_0 for the second oscillator, with the data found in the literature for the static absorption coefficient, it is not possible to associate this spectral feature to any static property of $CuGeO_3$.

For the excitation at 400 nm, it is possible to interpret our data accordingly to the cluster model developed by Fink *et al.* [65] in order to describe the electronic structure of $CuGeO_3$. These authors have investigated the energy losses spectrum and focus their attention on energy higher than 2 eV. They used the cluster model Cu_5O_{12} reported in Fig. 8.4. They took into account only the Cu $3d_{x^2-y^2}$ orbitals and the O $2p_{x\,(y)}$, so the results do not display the features below 2 eV associated to the *d-d* phonon assisted transitions.

In Fig.8.4 it is possible to see that the cluster model is built over 5 plaquettes, the system is divided into 2 sub-lattices. The first containing three Cu sites, and the O *2p* orbitals with the strongest overlap with the three Cu $3d_{x^2-y^2}$ orbitals (shaded Fig.8.4). The second sub-lattice contains two Cu-sites and the remaining O *2p* orbitals (un-shaded).

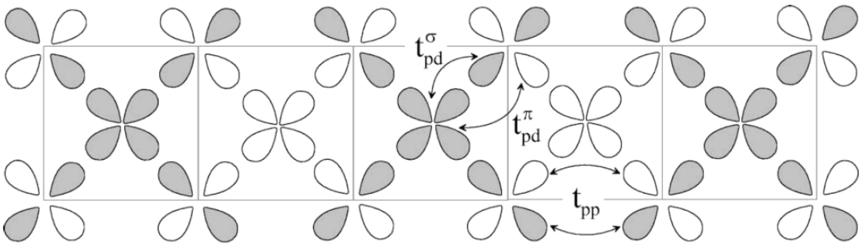

Fig. 8.4- *Cu_5O_{12} cluster model used in the calculation [65]. In the model only the Cu $3d_{x^2-y^2}$ and O $2p_{x(y)}$ orbitals are taken into account. The cluster is divided into two sublattices, marked by shaded or un-shaded orbitals. The three hopping integrals are indicated by double arrows [65].*

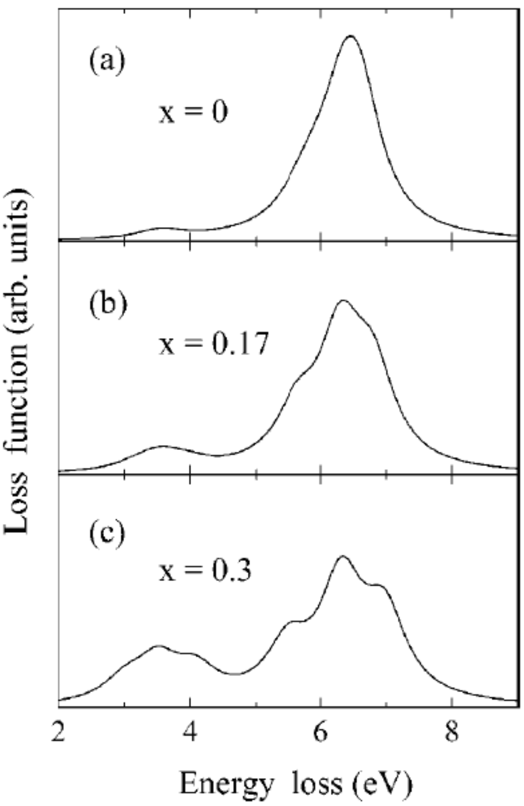

Fig. 8.5-*Different calculated loss functions for the three different couplings (x). An increase in the low energy peak is visible as the coupling increases [65].*

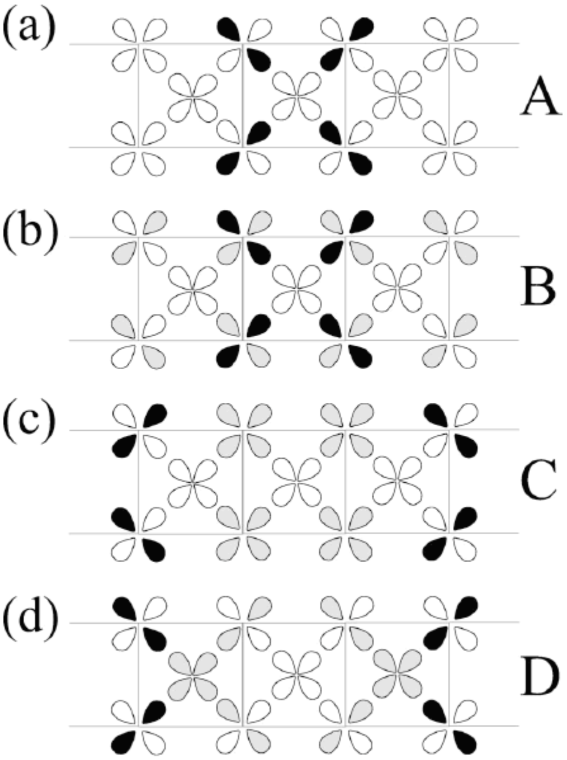

Fig. 8.6- *Qualitative description of four different final states. The black, grey and white colours stand for high, medium and low hole density[65].*

The hopping parameters of the model, displayed in the Fig.8.4, are taken to minimize the number of parameters of the cluster model. There is a single parameter t_{pp} for the hopping between two oxygen ions of the same sub-lattice. No hopping is possible between oxygen ions of different sub-lattices. For the hopping between Cu ions and

O ions there are two distinct terms, t_{pd}^{σ} describes the intra-plaquette hopping, and t_{pd}^{π} describes the hopping between different sub-lattices.

The results of the simulation show the presence of two spectral regions. One, at higher energy, centred at 6.2 eV and the other around 3.2 eV.

In the ground state the hole density is distributed for the 72% on the Cu site, and the remaining 28% are spread over the nearest neighbour O *2p* states.

The different final states, after the optical perturbation, are shown in Fig. 8.6. The three different colours of the orbitals represent the probabilities for the hole to occupy the states. Black colour stands for high hole density after the hopping process, grey for medium and white for low.

The feature at 6.2 eV is associated to the CT transition from the ground state to a localized final state with pure oxygen character (Fig8.6 (a)). Also the process described in Fig.8.6 (b) (centred at 6.8 eV) is localized, but with the presence of an additional hole density in the oxygen orbitals of the neighbouring (NN) plaquette, belonging to the second sub-lattice.

Considering the transition described in Fig.8.6 (c) the authors discuss the possibility to obtain a delocalized hole in the final state That can hop to the oxygen ions of the next nearest neighbouring (NNN) plaquette.

The feature around 3.2 eV is resulting from transitions into delocalized final state, with enhanced occupation of orbitals of the NN and NNN, described in Fig. 8.6 (d).

Interesting is to note that, in order to distinguish the contribution coming from the localized and delocalized transition, Fink et *al.* repeated the simulation by changing the inter-plaquette coupling parameter [65]. From a practical point of view the coupling parameter (indicated with x in figure 8.5) is related to the Cu-O-Cu angle. As x varies from 0 to 1, the bond angle increases from 90° to 180°.

In Fig.8.5 it is shown how the increasing in the bond angle ($x = 0.3$ is equivalent to an angle equal to 105°) induces the shift of spectral weight from the energy range above 6 eV to the one at lower energy.

Following the model developed in ref. [65] it is possible to speculate that the laser pump pulse excites a hole from the Cu 3d states into the O *2p* orbitals in the plane of the plaquette. This hole results strongly delocalized in the neighboring plaquettes (as it is shown in Fig. 8.6 (d)) and it is also partially delocalized over other Cu ions. The delocalization of the hole changes the hopping parameters and the characteristic electronic properties of the system. The change in the hole density is equivalent to the change in the electron density *n*, that is the typical order parameter of the MTI. Even if in $CuGeO_3$ is not evident a phase transition, a transient-laser induced change in the CT energy, due to the change in the band structure affected by the change of *n*, is observed.

The change in *n* lowers the energy split between the two Hubbard sub-bands, and so it lowers the energy required for the CT between the O *2p* non bonding-band and the Cu *3d* empty band. This description in terms of band is equivalent to the description reported by Fink *et al.* [65].

This electronic effect lasts few hundreds of femto-second, and they are consistent with an initial rapid decay process.

The slower dynamics is, instead, associated to the crystalline distortion, which changes the Cu-O-Cu bond angle and introduces a spectral shift from 6.2 eV towards smaller energy values.

As for the first band at 2.2 eV also the band at 2.9 eV can be related to a new meta-stable structural configuration, and it could explain the long time-scale of the relaxation process.

It is well-known that the electronic properties of a many-body system are controlled not only by *n* but also by *U/W*, where *W* is related to the hopping integrals and to the bond-angles in the crystalline structure [24]. The increasing in the bond angle (the cluster model parameter *x*) makes easier the hopping from a Cu ion to an O ion, and it explains the enhancement of the delocalized contribution to the energy loss spectrum. At the same time the increasing in the hopping integral enhances the "conductive" properties of the sample and it reduces the energy required for the CT excitation, explaining the presence, in our data, of a peak in the absorption spectra at energy lower than the one of the un-perturbed CT.

9. Conclusions

In this thesis we perform a time-resolved study of the out-of-equilibrium optical properties of $CuGeO_3$. The laser-induced change in the optical density is probed in a broad band spectral range (~400 nm – ~720 nm) through the use of a super-continuum ultra-fast laser pulse.

The relaxation of the system, after the excitation, is fitted with a convolution of three exponential decays. The fit residuals show a periodic modulation which is interpreted as a coherent phonon signature.

The coherent phonon period is ~100 fs, and it is comparable with a Raman active phonon with A_g symmetry [44]. This normal mode displacement consists in the vibration of the oxygen ions that tends to rotate the CuO_4 plaquettes.

The time-dependent dielectric function is calculated by a three step procedure. In the first step the fit of the static absorption coefficient provides the static model for the dielectric function. In the second step the time-dependent change in the trasmittivity is fit by a differential model. In the third step the time-dependent dielectric function is calculated from the differential model.

This analysis of the data shows the presence of two spectral features that can be fit with two Lorentz oscillators. The energy position of these oscillators (~2.2 eV and ~2.97 eV) can not be directly associated to any static property of $CuGeO_3$.

In addition, the temporal behaviour of the time-dependent dielectric function shows two time scale dynamics. One, of the order of hundreds of femtosecond, is ascribed to electronic de-excitation processes. The second, in the picosecond time scale, is ascribed to the vibrational cooling of the system.

The first band (at 2.2 eV) is interpreted as out-of-equilibrium *d-d* phonon assisted transition from the $d_{x^2-y^2}$ to the d_{z^2} orbitals. In the short time scale, the change in the energy position of this transition is due to the sudden change of the charge density distribution (n), induced by the photo-exciting laser pulse. The new charge distribution changes the local field felt by the copper ion inside the distorted-octahedral environment.

Moreover, the change of the electronic charge distribution lowers the screening of the ionic potential, and the ions start moving with their intrinsic velocities. This process is observe for both the pump pulse at 800 nm and 400 nm.

The picosecond time scale dynamic is due to the structural relaxation of the $CuGeO_3$. In fact the ionic displacement seems to leave the sample in a meta-stable structural configuration, in which the ratio of the $Cu\text{-}O_{apycal}$ and $Cu\text{-}O_{in\text{-}plane}$ is different from the static configuration. This interpretation is consistent with *ab initio* all electrons cluster calculations, where the change in the octahedron distortion controls the energy position of the $d_{x^2-y^2}$ - d_{z^2} transition [53].

The second band, at 2.97 eV, is ascribed to the CT transitions. On the fast time scale the change in the energy position of this feature could be due to the out-of-equilibrium charge re-distribution. In fact, by changing the many body interaction, the split of the Hubbard sub-bands could be lowered and the CT energy could diminish.

The change in the optical density on the picosecond time scale, which can not be ascribed to the variation of electronic density, is interpreted as an effect originating from the deformation of the $CuGeO_3$ lattice. The Cu-O-Cu bond angle modification affects the super-exchange term and therefore the U/W order parameter of the MTI.

As shown by Fink *et al.* [65] a feature due to the injection of a delocalized hole is observed in the absorption of $CuGeO_3$ at ~3.5 eV. The authors pointed out that the intensity and the width of this spectral feature increase as a function of the Cu-O-Cu bond angle.

In conclusion we have applied a new time-and-frequency resolved technique to investigate the photo-excited state of $CuGeO_3$. The experiment allows following the time-evolution of the dielectric function after a photo-excitation process, and it represents an advance in the study of the properties of strongly correlated material.

Bibliography

[1] J. G. Bednorz, K. A. Müller, Z. Phys. B. **64** 189 (1986)

[2] G. Grüner, Reviews Of Modern Physics **60** 4 (1988)

[3] E. Pytte, Phys. Rev. B. **10** 4637 (1974)

[4] J. A. Wilson, "The metallic and non-metallic states of matter", edited by P. P Edwards and C. N. B Rao (1985)

[5] A. Fujimori, Y. Tokura, Phys. Rev. Lett. **69** 1796 (1992)

[6] E. Dagotto, T. Hotta, A. Moreo, Phys. Rev. B. 344 1 (2001)

[7] S. Q. Liu, N. J. Wu, A. Ignatiev, Appl. Phys. Lett **76** 2749 (2000)

[8] J. Sakai, S Imai, J. Appl. Phys. 97 10 H 709 (2005)

[9] V. Kiryukhin, D. Casa, J. P- Hill, B. Kelmer, A. Vigilante, Y.Tomioka, Y. Tokura, Nature (London) 386 813 (1997)

[10] L. Hao, J. Wang, D. Y. Xing, Phys. Rev. B. **74** 014440 (2006)

[11] A. Cavalleri, C. S. Toth, C. W. Siders, J. A. Squier, F. Raksi, P. Forget, J. C. Kieffer, Phys Rev Lett **87** 237401 (2001)

[12] H. Okamaoto, Y. Ishige, S. Tanaka, H. Kishida, S. Iwai, Y. Tokura, Phys. Rev. B. **70** 165202 (2004)

[13] A. M. –T Kim, J. P. Callan, C.A. D.Roeser, E. Marzur, Phys. Rev. B **66** 245203 (2002)

[14] G. N. Glezer, Y. Siegal, L. Huang, E. Marzur, Phys. Rev. B. **51** 111995

[15] J. S. Graves, R. E. Allen, Phys. Rev. B. **58** 20 (1998)

[16] N. W. Ashcroft, N. D. Mermin, "Solid state physics", edited by Saunders College, Philadelphia (1976)

[17] F. Wooten, "Optical properties of solids", edited by Academic Press, New York (1972)

[18] S. Iwai, M. Ono, A. Maeda, H. Matsuzaka, H. Kishida, H. Okamoto, Y. Tokura, Phys. Rev. Lett. **91** 5 (2003)

[19] S. Pagliara, PhD's Thesis, Università degli Studi di Brescia (1999)

[20] R. R. Alfano, S. L. Saphiro, Phys. Rev. Lett. 24592 (1970)

[21] J. H. de Boer, E. J. W. Verway, Proc. Phys. Soc. London, Ser. A 49 59 (1937)

[22] N. F. Mott, Proc. Phys. Soc. London, Ser. A 49 72 (1937)

[23] J. Hubbard, Proc. Phys. Soc. London, Ser. A 277 237 (1964)

[24] M. Imada, A. Fujimori, Y. Tokura, Reviews Of Modern Physics **70** 4 (1998)

[25] J. Zaanen, G. A. Sawatzky, J. W Allen, Phys. Rev. Lett. **55** 418 (1985)

[26] F. Parmigiani, L. Sangaletti, A. Goldoni, U. Del Pennino, Z. –X Sheen, A Resvcolevschi, G. Dhalenne, Phys. Rev. B. **55** 3 (1997)

[27] M. Marezio, D. B. McWhan, J. D. Reineika, P. D. Dernier, Phys. Rev. B. **5** 2541 (1972)

[28] J. B. Torrance, P. Lacorre, A. I. Nazzal, E. J. Ansaldo, C. Niedermayer, Phys. Rev. B. **45** 8209

[29] Y. Tokura, Y. Okimoto, S. Yamaguchi, H. Taniguchi, T. Rimura, H. Takagi, Phys. Rev. B. **58** 12 1699

[30] A. Damascelli, Z. Hussain, Z. –X Sheen, Reviews of Modern Physics **75** (2003)

[31] N. F. Mott, "Metal-insulator transition", edited by Taylor and Francis, London-Philadelphia (1990)

[32] A. S. Barker, H. W. Verleur, H. J. Guggenheim, Phys. Rev. Lett. **17** 1286 (1966)

[33] F. Gervais, W. Kress, Phys. Rev. B. **31** 4809 (1985)

[34] R. Srivastava, L. L. Chase, Phys. Rev. Lett. **27** 727 (1971)

[35] D. B. McWhan, M. Marezio, J. P. Remeika, P.D. Dernier, Phys. Rev. B. **10** 490 (1974)

[36] A. Cavalleri, Th. Dekursy, H. H. W. Ching, J. C. Vieffer, R.W. Schoenlein, Phys. Rev. B. **70** 161102 (2004)

[37] L. Luer, G. Manzini, G. Cerillo, G. Lanzani, M. Meneghetti, Phys. Rev. Lett. **99** 027401 (2007)

[38] M. Chellet, *et al.,* Journal of Physics: Conference Series **21** 130-135 (2005)

[39] T. Ogawa, Solid State Phenomena Vol **112** (2006)

[40] C. Giannetti, G. Coslovich, F. Cilento, G. Ferrini, F. Parmigiani, (not published) (2008)

[41] A. Sawa, M. Kawasaki, H. Takagi, Y. Tokura, Phys. Rev. B. **66** 014531 (2002)

[42] M. Bassi, P. Camagni, R. Rolli, G. Samoggia, F. Parmigiani, G. Dhalenne, A. Revcolevschi, Phys. Rev. B. **54** 16 (1996)

[43] S. Pagliara, F. Parmigiani, P. Gallinetto, A. Revcolevschi, G. Samoggia, Phys. Rev. B. **66** 024518 (2002)

[44] Z. V. Popovic, S. D. Devic, V. N. Popov, G. Dhalenne, A. Revcolevschi, Phys. Rev. B. **52** 06 (1995)

[45] D. Nardi, Master's Thesis, Università degli Studi di Brescia (2006)

[46] Y. Mizuno, T. Tohyama, S. Maekawa, T. Osafune, N. Motoyama, H. Eisaki, S. Uccida, Phys. Rev. B. **57** 9 (1998)

[47] J. B. Goodenough, Phys. Rev. **100** 564 (1955)

[48] J. Kanamori, J. Phys. Chem. Solids **10** 87 (1959)

[49] P. W. Anderson, Solid State Phys. **14** 99 (1963)

[50] W. Geertsma, D. Khomskii, Phys. Rev. B. **54**, 3011 (1996)

[51] A. Damascelli, D. van der Marel, G. Dhalenne, A. Revcolevschi, Cond. Matt. 9906159 01 (1999)

[52] F. M. F. De Groot, J. Electron Spectroscopy Relat. Phenom. **67** (1994)

[53] Coen de Graaf, Ria Broer, Phys. Rev. B. **62** 1

[54] Operator's manual for Verdi and Mira, Coherent Laser Division

[55] J. C. Diels, W. Rudolph, "Ultrashort laser pulse phenomena", edited by Academic Press (2006)

[56] L. Postregna, Bachelor's Thesis, Università degli Studi di Trieste (2007)

[57] Legend user Manual, Coherent Laser Division.

[58] C. Consani, Master's Thesis, Università degli Studi di Trieste (2007)

[59] User guide and Specification NI c DAQ-9172, National Instruments

[60] Guide to RefFIT, Alexey Kuzmenko

[61] J. Chesnoy, A. Mokhtari, Phys. Rev. A. **38** 3566 (1988)

[62] H. Zeiger, J. Vidal, T. K. Cheng, E. P. Ippen, G. and M. S. Dresselhaus, Phys. Rev. B. **45** 768 (1992)

[63] G. Garrett, T. F. Albrecht, J. F. Whitaker, R. Merlin, Phys. Rev. Lett. **77** 3661 (1996)

[64] O. V. Misochko, M. V. Lebedev, H. Schäfer, T. Dekorsy, Journal of Physics: Condensed Matter **19** 406220 (2007)

[65] S. Atzkern, M. Knupfer, M. S. Golden, J. Fink, A. Hübsch, C. Waidacher, K. W. Becker, W. von der Linden, M. Wiedem, C. Geibel, Phys. Rev. B. **64** 075112 (2001)